

# Simulation-based Microstructure Imaging: From Forward Signal Modeling to Machine Learning

Présentée le 10 septembre 2021

Faculté des sciences et techniques de l'ingénieur  
Laboratoire de traitement des signaux 5  
Programme doctoral en génie électrique

pour l'obtention du grade de Docteur ès Sciences

par

**Jonathan Rafael PATINO LOPEZ**

Acceptée sur proposition du jury

Prof. D. N. A. Van De Ville, président du jury  
Prof. J.-Ph. Thiran, directeur de thèse  
Prof. T. Dyrby, rapporteur  
Dr S. Deslauriers-Gauthier, rapporteuse  
Prof. G. Knott, rapporteur

## Acknowledgements

I want to thank everyone here — colleague, friend, or family — who helped me through these four years, to all the ones still with us and those who left.

Thank you.

To all my colleagues, starting with my supervisor Prof. Jean-Philippe. He has been constant guidance and support of all my good ideas and quite a few bad ideas. You helped me to survive the scientific and non-scientific aspects of Academia. I'm equally grateful to Prof. Giorgio Innocenti, without whom I would have never found my scientific curiosity that now drives me at every step of my career. I was so fortunate to have worked with both of you.

To everyone at the LTS5. Colleagues, friends, and foosball victims. (Dr). David Romascano, (Dr.) Muhamed and (Dr) Gaetan, who welcomed me and then suffered me on my first years of PhD, thanks for all the discussion and the fun; I did it too! To Marco, Gab, Elda and Erick, you were all my co-supervisors. Thanks for being there and always have time to help me inside and outside the lab. To the young and naïve Tom, Francesco, Juan Luis and Remi, you are all welcome to have met me. To all the fans I left behind, Saeed, Christophe, Saleh, Dimitri, Christian, Samuel, Mina, thanks for all the games and coffee breaks, and sorry for my noisy keyboard; Yes, I totally did it on purpose. I am equally appreciative of all the other friends I made along the way, all the Mateos, Alessandros, and Marcos (and one Mauro); cheers.

Thanks a lot to all the collaborators who welcomed me into their teams. Prof. Tim Dyrby and his fantastic team, thanks for inviting me to be part of such unique works. To Mariam,

who remains my example of positively naïve spirit, and to Sidsel, which I may have depressed at moments, I hope to see you all soon. Thanks to Prof. Emmanuel Caruyer for hosting me at his lab and to the excellent MMINCARAV team; I'm sure if Raphael and I sit and work hard enough, we will come with a better name for the team. Thanks a lot to Prof. Graham Knott and Samuel Deslauriers-Gauthier for their comments; we had great discussions.

Thanks to all people who made this journey possible, and without whom, I wouldn't be here. Prof. Alessandro Daducci, Prof. Gary Zhang, Prof. Alonso Ramirez, Dr. Joaquín Peña, Prof. Luis Concha; it has been a long journey which you started with me.

Finally, if you reached this part, you are probably my family. So please ignore all the above. You know this thesis was only possible because of all of you. To my parents, sister, and my lovely wife. It's over.



# Abstract

---

This thesis focuses on the signal modelling of Diffusion-Weighted Magnetic Resonance Imaging (DW-MRI) in the brain's white matter (WM). DW-MRI a non-invasive technique with enormous potential for the study of the brain's microstructure by measuring the diffusion properties of biological tissue. In order to infer such microstructure properties from DW-MRI signals — for example the axon's diameter distribution or the neurite dispersion, just to mention a few — many models have been proposed in the past decades. However, such models have relied on disregarding several structural components of the WM, like the diameter and direction changes along the axons or the volumetric changes in the tissues' water compartments, which inherently affect the diffusion properties of the studied media. This large heterogeneity in the WM tissue, summed to the high structural variability between different brains regions or WM tracks, have prevented researchers from formulating accurate analytical models to this day.

The following work proposes a paradigm change from the conventional analytic model-based approach to a simulated-based one, centered in the simulation of DW-MRI signals in realistic virtual tissue. Our work starts with the challenge of creating a robust framework for the simulation of DW-MRI as a forward modelling tool for microstructure estimation and continues exploring the simulator capabilities to create a simulation-based microstructure modelling strategy. Each chapter of this thesis presents several contributions to the field for the construction of realistic white matter numerical phantoms, which can later be used for the estimation of the axons' density and diameter distribution, or the design of novel microstructure-specific DW-MRI acquisition sequences. Thus, the contributions presented in this work pave the way for the modelling, study, and validation of complex microstructure models of brain white matter.

**Keywords:** Diffusion, MRI, Simulations, Monte Carlo, Machine Learning, Brain, Microstructure.

# 1.1 Table of Contents

Abstract .....	v
1.1 Table of Contents .....	vi
1.2 List of Figures .....	x
Chapter 1 Introduction .....	xiii
1.1 Content of the Thesis .....	xiv
1.2 Relevant Publications.....	xv
Chapter 2 Background .....	19
2.1 Overview.....	19
2.2 Diffusion-Weighted Magnetic Resonance Imaging.....	20
2.3 Self-diffusion of water molecules .....	20
2.4 NMR Diffusion contrast .....	23
NMR diffusion contrast in the brain's tissue .....	26
2.5 White matter signal models .....	30
Diffusion Tensor .....	30
Diffusion Kurtosis.....	32
Compartment models .....	32
Axon diameter model.....	33
Fibre dispersion and orientation distribution .....	35
Fast microstructure parameters estimation. ....	35
2.6 DW-MRI Simulations .....	37
DW-MRI Monte-Carlo Simulations .....	40
Particle Dynamics Simulation.....	40

Signal Computation .....	42
Simulation computation complexity .....	44
Chapter 3 Robust and Realistic DW-MRI Monte-Carlo Simulations .....	47
3.1 Overview .....	47
3.2 Design and Validation of MCDS .....	48
Number of samples in an MCDC .....	48
Impact of the Intra-axonal space simplifications .....	51
Extra-axonal space representation .....	52
3.3 Results .....	53
Convergence analysis .....	53
Intra-axonal space representation results .....	55
Extra-axonal space representation results .....	57
3.4 The MC/DC Simulator .....	59
3.5 Discussion and Conclusions .....	60
Chapter 4 Towards Realistic and Complex Numerical Phantoms .....	62
4.1 Overview .....	62
4.2 Complex substrates generation framework .....	63
Results on a fibre-crossing substrate .....	66
Conclusions .....	70
4.3 The DiSCo Numerical Phantom for Connectomics .....	70
Phantom Design .....	71
DW-MRI Signal Simulation .....	73
Resulting Dataset .....	75

Conclusion .....	75
4.4 MCDS in 3d reconstructed tissue .....	76
Conclusions.....	78
Chapter 5 Simulation-Assisted Machine Learning .....	79
5.1 Overview .....	79
5.2 Introduction.....	80
5.3 Simulation-Assisted Machine Learning models .....	82
5.4 Results and Discussion .....	84
5.5 Conclusion and contributions .....	87
Chapter 6 Simulation-Assisted Protocol Optimization.....	89
6.1 Overview .....	89
6.2 Fisher information based Optimal waveforms.....	89
Signal and noise model .....	91
Numerical substrate design .....	92
Evolution process.....	94
Signal simulation .....	95
6.3 Optimized waveforms .....	95
6.4 Conclusion .....	98
Chapter 7 Data-driven Machine Learning: Perspectives for the Simulation of Realistic DW-MRI Signals .....	99
7.1 Overview .....	99
7.2 Anomalous Tissue Detection .....	99
Data .....	102



Multi-component T2 reconstruction .....	103
Multi-compartment microscopic diffusion MRI model.....	104
Lesion identification .....	104
Machine learning-based classification scores .....	105
Results.....	106
Conclusions and perspectives .....	110
7.3 Microstructure Maps using Trainable Sparse Encoders .....	111
Introduction.....	111
COMMIT .....	111
Learned Sparse Encoding .....	112
Sparse Encoding for Microstructure Estimation.....	113
In-Vivo Dataset and Processing.....	114
Results.....	115
Conclusions.....	116
Chapter 8 Conclusions and Perspectives .....	118
References.....	122

## 1.2 List of Figures

Figure 3-1 PGSE protocol and the diffusion experiment. ....	23
Figure 3-2 Water diffusion compartments characteristics .....	27
Figure 2-3 Streamline Axon Diameter Index (mADI).....	37
Figure 4-1: Gamma distributed radii and corresponding intra-axonal diffusion signal. ....	49
Figure 3-2: Curved meshes used as intra-axonal substrates. ....	52
Figure 3-3 RMAE Intra- extra- axonal tests. ....	54
Figure 3-4 Tables with the diameter fitting results. ....	56
Figure 3-5 Results for three substrates, with 100, 1,000 and 10,000 cylinders, respectively. ....	58
Figure 3-6 Single MC/DC simulation core components. ....	60
Figure 4-1 Optimized non-overlapped trajectories.....	64
Figure 4-2 Fiber crossing substrate. ....	65
Figure 4-3 Model bases results of the crossing signal. ....	67
Figure 4-4 ICVF maps of one volume slice in the XZ-plane in three different resolutions. ....	68
Figure 4-5 Axon diameter estimation maps and distributions. ....	69
Figure 4-6 DiSCo Phantom construction steps.....	72
Figure 4-7 Mesh of the 12,196 strands used as input to the MC/DC diffusion simulator.....	74
Figure 5-8 . Photomicrograph showing axons and the resulting 3d reconstruction.....	77
Figure 5-9 EM 3d reconstruction and quantification.....	77
Figure 4-10 A numerical phantom using MODERN. ....	78
Figure 5-1 Simulation-based framework pipeline. ....	80
Figure 5-2 Substrate generation characteristics.....	82
Figure 5-3 Estimates of the trained regressors on the validation dataset.....	85
Figure 5-4 Joint histogram of the estimated mean diameters. ....	85

<i>Figure 5-5 Midsagittal plane of the estimation maps for two subjects (showed from posterior to anterior).</i>	86
<i>Figure 6-1 Example of substrate design composed of intra- and extra-axonal spaces.</i>	93
<i>Figure 6-2 Fisher information vs b-value</i>	96
<i>Figure 6-3 Cross-over procedure</i>	96
<i>Figure 6-4 Waveforms genetically generated to optimize the Fisher Information</i>	97
<i>Figure 6-5 Histogram of the Fisher information of DW-MRI sequences</i>	97
<i>Figure 7-1 Visualization of the extracted training data for the lesions (light blue) and NAWM voxels (purple).</i>	105
<i>Figure 7-2 Confusion matrix of the three trained models</i>	107
<i>Figure 7-3 Voxel-wise lesion probability maps for one control subjects used in the validation.</i>	108
<i>Figure 7-4 Voxel-wise lesion probability maps for two MS subjects used in the validation.</i>	109
<i>Figure 7-5 The network architecture of LISTA truncated to the number of layers.</i>	112
<i>Figure 7-6 Voxel-wise map of the mean Axon Diameter Index</i>	113
<i>Figure 7-7 DNN vs COMMIT bases mADI results.</i>	116

Hey Giorgio! Look at this...

# Chapter 1 Introduction

---

In this dissertation we tackle the challenges of Diffusion-Weighted Magnetic Resonance Imaging (DW-MRI) and microstructure modeling from a novel simulation-based perspective. This work was conducted under the supervision of Professor Jean-Philippe Thiran (École Polytechnique Fédérale de Lausanne (EPFL), Switzerland) and continues previous work from (Romascano, 2019) at the LTS5 and in collaboration with several laboratories such as the Danish Research Centre for Magnetic Resonance (DRCMR) and the Multimodal Microstructure-Informed Connectivity: Acquisition, Reconstruction, Analysis and Validation (MMINCARAV) international laboratory.

The modelling and reconstruction of DW-MRI signals from the brain's WM is, to this day, an open challenge due to the outstanding complexity of the WM microstructure and the tissue's heterogeneity in different regions of WM. Current models in the literature are still limited to different degrees due to the use of simplified WM microstructure geometries, such as in the changes of diameter and direction along the individual axons or the volumetric changes in the tissues' water compartments, which inherently affect the magnitude and anisotropy of the confined diffusion process. In this thesis, we tackle these limitations from a simulation-based approach. Notably, the new simulation approach presented in this thesis, apart from serving as a validation tool for the study of the limitation of previously proposed methods in the literature, can be employed as a forward-modelling tool for the generation of synthetic data, usable as training data for Machine Learning-based approaches, which can be then employed for the estimation of the axons' density and diameter distribution (Chapter 5), or for the design of novel microstructure-specific DW-MRI acquisition sequences (Chapter 6).

This work starts with the challenge of creating a robust framework for the simulation of Diffusion-Weighted Magnetic Resonance Signals (DW-MRI) as a forward modelling tool for microstructure estimation and continues exploring the simulator capabilities to create a new simulation-based microstructure modelling strategy.

## 1.1 Content of the Thesis

The content of the following seven chapters of this thesis will follow the listed structure below:

- Chapter 2: Background. Summary of the state-of-the-art and theory of Diffusion-Weighted MRI, tissue microstructure and diffusion simulations for synthetic data generation.
- Chapter 3: Robust and Realistic DW-MRI Monte-Carlo Simulations. Summary on the contributions about the sign and validation of MCDS diffusion simulations.
- Chapter 4: Towards Realistic and Complex Numerical Phantoms. Contribution chapter on the creation and complex substrate for MCDS mimicking the brain's white matter microstructure.
- Chapter 5: Simulation-Assisted Machine Learning. Microstructure estimation using MCDS simulations to train machine learning models.
- Chapter 6: Simulation-Assisted Protocol Optimization. This chapter focuses on the creation of microstructure-specific MRI protocols using MCDS.
- Chapter 7: Data-driven Machine Learning: Perspectives for the Simulation of Realistic DW-MRI Signals. A chapter dedicated to estimating tissue properties using data-driven approaches outlines our research future work.

- Chapter 8: Contributions and Conclusions.

## 1.2 Relevant Publications

The chapters listed above are supported by the following publications and research contributions to the field where the author has significantly contributed:

### Chapter 3 and Chapter 4:

**Rafael-Patino, J.**, Romascano, D., Ramirez-Manzanares, A., Canales-Rodríguez, E. J., Girard, G., & Thiran, J. P. (2020). *Robust Monte-Carlo Simulations in Diffusion-MRI: Effect of the Substrate Complexity and Parameter Choice on the Reproducibility of Results*. *Frontiers in Neuroinformatics*, 14. <https://doi.org/10.3389/fninf.2020.00008>

**Rafael-Patino, J.**, Gabriel Girard, Raphael Truffet, Marco Pizzolato, Emmanuel Caruyer, Jean-Philippe Thiran. (2021). *The Diffusion Simulated Connectivity (DiSCo) Dataset*. Springer Data in Brief. DIB-D-21-00567. Submitted.

**Rafael-Patino, J.**, Thomas Yu, Mariam Andersson, Hans Martin Kjer, Vedrana Andersen Dahl<sup>3</sup>, Alexandra Pacureanu, Anders Bjorholm Dahl, Tim B. Dyrby, and Jean-Philippe Thiran. *Phantoms for Diffusion Simulations: Multi-Objective Differential Evolution for Realistic Numerical (MODERN) Phantoms.*, 2019 Proc. Intl. Soc. Mag. Reson. Med. 27 (2019), Montreal, Canada, 2019

**Rafael-Patino, J.** *et al.* (2021) ‘The Diffusion-Simulated Connectivity Dataset’. Mendeley, 1. doi: 10.17632/FGF86JDFG6.1.

### Chapter 5:

**Rafael-Patino, J.**, Yu, T., Delvigne, V., Barakovic, M., Pizzolato, M., Girard, G., Jones, D. K., Canales-Rodríguez, E. J., & Thiran, J. P. (2020). *DWI Simulation-Assisted Machine Learning Models for Microstructure Estimation*. In *Mathematics and Visualization* (pp. 125–134). Springer Science and Business Media Deutschland GmbH. [https://doi.org/10.1007/978-3-030-52893-5\\_11](https://doi.org/10.1007/978-3-030-52893-5_11)

#### Chapter 6:

**Rafael-Patino, J.\***, Truffet, R.\*, Girard, G., Pizzolato, M., Barillot, C., Thiran, J.-P., & Caruyer, E. (2020). *An Evolutionary Framework for Microstructure-Sensitive Generalized Diffusion Gradient Waveforms*. In *Lecture Notes in Computer Science* (including subseries *Lecture Notes in Artificial Intelligence* and *Lecture Notes in Bioinformatics*): Vol. 12262 LNCS. [https://doi.org/10.1007/978-3-030-59713-9\\_10](https://doi.org/10.1007/978-3-030-59713-9_10) \* Equally contributed first authors.

#### Chapter 7:

**Rafael-Patino, J.**, M. Barakovic, G. Girard, A. Daducci and J-P. Thiran, *Learning Global Brain Microstructure Maps Using Trainable Sparse Encoders*, 2019 IEEE International Conference on Image Processing (ICIP), Taipei, Taiwan, 2019, pp. 2926-2930, doi:10.1109/ICIP.2019.8803733.

**Rafael-Patino, J ±\***, Elda Fisch-Gomez\*, Marco Pizzolato, Gian Franco Piredda, Tom Hilbert, Tobias Kober, Erick Jorge Canales-Rodríguez, Jean-Philippe Thiran. *Multi-Compartment Diffusion MRI, T2 Relaxometry and Myelin Water Imaging as Neuroimaging Descriptors for Anomalous Tissue Detection*. 2021 IEEE 18th International Symposium on Biomedical Imaging (ISBI 2021).

#### Other relevant contributions:



- Rafael-Patino, J.**, Girard, G., Romascano, D. P. R., Barakovic, M., Rensonnet, G. O. D., Thiran, J.-P., & Daducci, A. (2018). *Realistic 3D Fiber Crossing Phantom Models for Monte Carlo Diffusion Simulations*. 26th Annual meeting of the International Society for Magnetic Resonance in Medicine, Paris, France, June, 2018
- Rafael-Patino, J** & Girard, Gabriel & Fischl, Elda & Romascano, David & Yu, Thomas & Pizzolato, Marco & Ramirez-Manzanares, Alonso & Canales-Rodríguez, Erick & Thiran, Jean-Philippe. (2020). *Multi-diffusion and Multi-T2 weighted Monte-Carlo Simulations*. 2020 OHBM ANNUAL MEETING 10.13140/RG.2.2.19239.78241.
- Rensonnet, G., **Rafael-Patino, J.**, Macq, B., Thiran, J.-P., Girard, G., & Pizzolato, M. (2020). *A Signal Peak Separation Index for axisymmetric B-tensor encoding*. <http://arxiv.org/abs/2010.08389>
- Andersson, M., Kjer, H. M., **Rafael-Patino, J.**, Pacureanu, A., Pakkenberg, B., Thiran, J. P., Ptito, M., Bech, M., Dahl, A. B., Dahl, V. A., & Dyrby, T. B. (2021). *Axon morphology is modulated by the local environment and impacts the non-invasive investigation of its structure-function relationship*. Proceedings of the National Academy of Sciences of the United States of America, 117(52), 33649–33659. <https://doi.org/10.1073/PNAS.2012533117>
- Girard G., Caruyer E., **Rafael-Patino, J**, Pizzolato M, Truffet R., & Jean-Philippe Thiran, (2021). *Diffusion-Simulated Connectivity Challenge*. doi: 10.5281/ZENODO.4733450.
- Romascano, D., Barakovic, M., **Rafael-Patino, J.**, Dyrby, T. B., Thiran, J., & Daducci, A. (2020). *ActiveAx<sub>ADD</sub>: Toward non-parametric and orientationally invariant axon diameter distribution mapping using PGSE*. *Magnetic Resonance in Medicine*, 83(6), 2322–2330. <https://doi.org/10.1002/mrm.28053>

- Nath, V., Schilling, K. G., Parvathaneni, P., Huo, Y., Blaber, J. A., Hainline, A. E., Barakovic, M., Romascano, D., **Rafael-Patino, J.**, ... Landman, B. A. (2019). *Tractography reproducibility challenge with empirical data (TraCED): The 2017 ISMRM diffusion study group challenge*. *Journal of Magnetic Resonance Imaging*. <https://doi.org/10.1002/jmri.26794>
- Yu, T., Pizzolato, M., Girard, G., **Rafael-Patino, J.**, Canales-Rodríguez, E. J., & Thiran, J.-P. (2019). Robust Biophysical Parameter Estimation with a Neural Network Enhanced Hamiltonian Markov Chain Monte Carlo Sampler. In *Lecture Notes in Computer Science (including subseries Lecture Notes in Artificial Intelligence and Lecture Notes in Bioinformatics): Vol. 11492 LNCS*. [https://doi.org/10.1007/978-3-030-20351-1\\_64](https://doi.org/10.1007/978-3-030-20351-1_64)
- Schilling, K. G., Nath, V., Hansen, C., Parvathaneni, P., Blaber, J., Gao, Y., Neher, P., Aydogan, D. B., Shi, Y., Ocampo-Pineda, M., Schiavi, S., Daducci, A., Girard, G., Barakovic, **Rafael-Patino, J.**, ... Landman, B. A. (2019). Limits to anatomical accuracy of diffusion tractography using modern approaches. *NeuroImage*, 185. <https://doi.org/10.1016/j.neuroimage.2018.10.029>
- Canales-Rodríguez, E. J., Legarreta, J. H., Pizzolato, M., Rensonnet, G., Girard, G., **Rafael-Patino, J.**, Barakovic, M., Romascano, D., Alemán-Gómez, Y., Radua, J., Pomarol-Clotet, E., Salvador, R., Thiran, J. P., & Daducci, A. (2019). *Sparse wars: A survey and comparative study of spherical deconvolution algorithms for diffusion MRI*. *NeuroImage*, 184, 140–160. <https://doi.org/10.1016/j.neuroimage.2018.08.071>
- Romascano, D, **Rafael-Patino, J.**, Jelescu, I, Barakovic, M, Dyrby, TB, Thiran, J-P & Daducci, A. 2018, ‘Voxel size matters: big voxels are required to generate realistic extra-axonal dMRI signals from Monte Carlo simulations’, pp. 1-2. Proc. Intl. Soc. Mag. Reson. Med. 26 (2018)

# Chapter 2 Background

---

## 2.1 Overview

Diffusion-Weighted Magnetic Resonance Imaging (DW-MRI) is a non-invasive technique based on the self-diffusion process of water molecules in tissues, providing relevant clinical and biological information that no other MRI modality can provide. This technique is known as Diffusion-Weighted MRI (DW-MRI). In the brain, water diffusion is influenced by the microstructure of the tissue in which the molecules are situated, so quantifying diffusion provides indirect measures of the microstructure's properties. For at least two decades, the DW-MRI technique has been extensively used to assess acute ischemic stroke and other neurological disorders sensitive to diffusion changes in brain tissue (Sorensen *et al.*, 1996; Horsfield, Jones and Horsfield, 2002; Sotak, 2002). Its usefulness is based on its ability to measure the average diffusion coefficient in an image voxel — coined as the *apparent* diffusion coefficient (ADC). The term *apparent* relates to the fact that the resulting coefficient is sensitive to a variety of factors, including the DW-MRI acquisition procedure, the hardware properties, the characteristics of the tissues, and the surrounding environment; making the interpretation and study of the ADC value a multidimensional problem that often results in an ill-conditioned problem (Bihan, 2013; Le Bihan and Lima, 2015). As a result of this, and due to the complexities of brain microstructure, the nature of the DW-MRI contrast caused by changes in geometrical tissue properties is still unknown. Because of these constraints, there is a need to develop simulation tools that enable researchers to study complex scenarios and propose ad-hoc models for the high-quality data we can now achieve in modern scanners (Yaniv, 2013; Ferizi *et al.*, 2015, 2017). The development of next-generation MR sequences will ultimately benefit from comprehensive, systematic, and dependable simulations of realistic microstructure scenarios.

In this background chapter, we will go through the main theoretical concepts of DW-MRI, focusing on the basic principles behind signal decay, which are the building blocks needed to synthesize artificial simulated signals, that will be addressed at the end of the chapter. More specifically, the following section introduces fundamental concepts in neuroanatomy, state-of-the-art mathematical models, and ideas behind microstructure modelling, which we used through our contribution work of this thesis. The section will end with a technical overview of Monte-Carlo simulations, centred on creating more realistic virtual tissue in future chapters.

## 2.2 Diffusion-Weighted Magnetic Resonance Imaging

Nuclear Magnetic Resonance (NMR) results from the mutual interaction among the magnetic moments (such as the hydrogen nucleus  $^1\text{H}$  in the water molecules) in the sample and an induced constant magnetic field. This phenomenon appears in magnetic systems made up of elements that possess a magnetic moment, e.g. protons. Water molecules are susceptible to this effect. Due to the spontaneous displacements of the molecules caused by thermal motion, spins that move randomly experience non-uniform changes in their *precession rate*, which results in a dephasing that contributes to a loss of the MRI signal. The physical foundations of DW-MRI are then essentially based on this interaction between an induced magnetic field and the three-dimensional (3d) water diffusion, making the understanding of the water molecules diffusion process in complex media of utmost importance.

## 2.3 Self-diffusion of water molecules

Water molecules are in continuous motion and collide with each other at temperatures greater than absolute zero (0K). This particle-to-particle interaction also produces random displacements resulting in a self-diffusion phenomenon, which affects the local magnetic field felt by their nucleus of hydrogen. These changes in the field lead to the relaxation phenomena in which the T2 weighted MR contrast is based (Whittall *et al.*, 1997). As it

will be explained in the following sections of this chapter, in the presence of a non-uniform linear magnetic field (gradient), molecules that move randomly suffer random changes in their spins' precession rate, which ends into dephasings that contribute to the MRI signal loss.

A random walk model can be used to explain this type of diffusion process, in which, at each time interval ( $\tau$ ), a molecule moves a random distance ( $r$ ) in a random direction. This view of diffusion as a random walk is usually built from the traditional understanding of diffusion as a flux of particles down a concentration gradient described by Fick's first law formula (Fick, 1855),

$$J(x, \tau) = -D \nabla c(x, \tau), \quad 2-1$$

where  $J$  is the particle flux (number of particles passing through a unit area per second),  $\nabla c(x, t)$  is the gradient of the particle concentration, and  $D$  is the diffusion coefficient. Equation 2-1 gives us an empirical law relating the total flux to the particle concentration. Furthermore, because of the conservation of mass, the continuity theorem can be applied and further write Eq. 2-1 as,  $\frac{\delta c(x, \tau)}{\delta \tau} = -\nabla J(x, \tau)$ , (Fick, 1855). By substituting Eq. 2-1 in the former form, we can then write Flick's second Law as follow:

$$\frac{\delta c(x, \tau)}{\delta \tau} = D \nabla^2 c(x, \tau). \quad 2-2$$

Flick's second law relates the time evolution of the concentration with respect to the spatial Laplacian operator. In the case of homogeneous media where  $D$  can be considered constant, Flick's second law with initial Dirac conditions ( $c(x, 0) = \delta(x)$ ) has the following solution (Powles *et al.*, 1992) :

$$c(x, \tau) = \frac{1}{\sqrt{(4\pi D\tau)}} e^{\left(-\frac{x^2}{4D\tau}\right)}. \quad 2-3$$

In the self-diffusion phenomenon, however, the concentration gradient is not present, and specifically for the application in DW-MRI, we are concerned about the total probability of a particle to displace from a position  $x_0$  to  $x_1$  in a given time  $\tau$ :

$$P(x_1, \tau) = \int \rho(x_0) P(x_0, x_1, \tau) dx_0. \quad 2-4$$

Furthermore, if we change the concentration gradient for the previous equation and relate  $J$  to the conditional probability flux, Eq 2-4 becomes:

$$\frac{\delta P(x_0, x_1, \tau)}{\delta t} = D \nabla^2 P(x_0, x_1, \tau) \quad 2-5$$

Using Eq.2-5, (Albert Einstein, 1956) calculated the mean-squared displacement of free diffusion to describe the Brownian motion of an ensemble of particles as:

$$\langle x^2 \rangle = 2dD, \quad 2-6$$

where  $d$  is the dimensionality of  $x$ , and  $\langle x^2 \rangle$  is the mean squared displacement of molecules ensemble. At a temperature of 25°C. the water diffusion coefficient is approximately  $2.2 \times 10^{-3} mm^2/s$ ; on the other hand, in soft tissue, because of the reduced mobility of the water molecules, the diffusion coefficient is in general smaller than in pure water (Bihan, 2013). When applying any Brownian water motion model, it is necessary to distinguish between the actual diffusion coefficient of pure water and the apparent diffusion coefficient (ADC) that can be measured.

Finally, to relate the parameters of a random walk such as the total displacement  $r$  and diffusion time  $\tau$ , to  $D$ , the net flux past a particular point  $x$  in a one-dimensional random walk is considered, in which  $D$  is related to the parameters of a random walk as (Buxton, 2009):

$$D = \frac{r^2}{2\tau}. \quad 2-7$$

Because of this phenomenon, a local diffusion coefficient can be estimated by applying the aforementioned magnetic gradient. Even though the net displacement of a molecule could be close to zero for a given time in a random walk, the total distance travelled by the molecule is much larger. This is because every molecule follows a random path from its

initial position due to the collisions with other water molecules and with a velocity proportional to the environmental temperature.

## 2.4 NMR Diffusion contrast

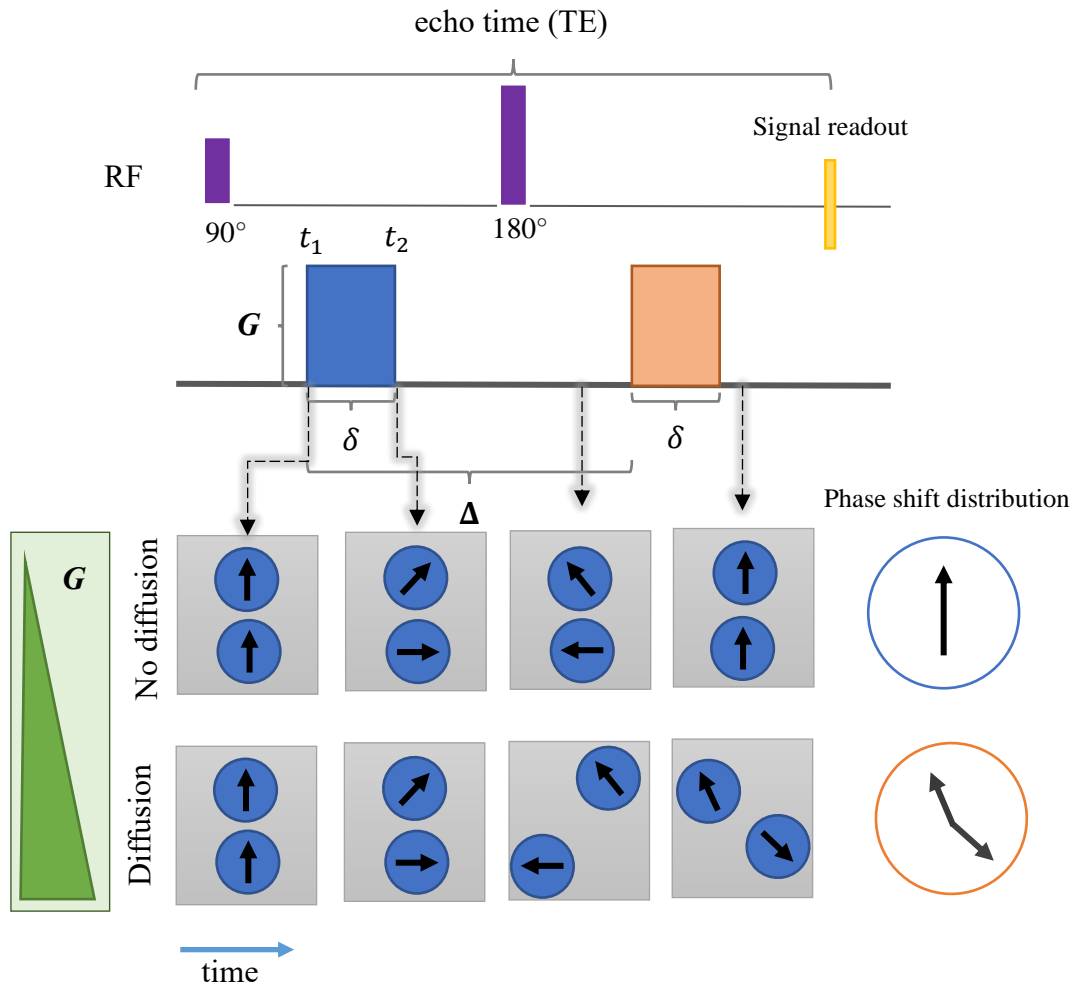


Figure 2-1 PGSE protocol and the diffusion experiment.

Illustration of the effect of the Brownian motion of an ensemble of two water molecules in comparison with a non-diffusing scenario. The PGSE protocol is also illustrated in the panel above, consisting of two gradient blocks with duration  $\delta$ , magnitude  $G$ . After that, the molecules are able to diffuse freely during the  $\Delta$  duration. If the water molecules diffused along the gradient field direction (bottom column), the refocusing will be imperfect and the phase shift distribution will be different from zero.

Diffusion imaging is based on the previously described molecular self-diffusion phenomenon and the effects of linear magnetic gradients on the spin of the molecules. The classical pulsed gradient spin-echo (PGSE) protocol is the most frequently used DW-MRI protocol (Tanner and Stejskal, 1968), as illustrated in Figure 2-1. This protocol's key elements can be parametrized by timings between the two applied pulses ( $\Delta$ ), the total time they are active ( $\delta$ ), and the gradient amplitude  $\mathbf{G}$ . Following a  $90^\circ$  excitation pulse, the spatial gradient with amplitude  $\mathbf{G}$  and duration  $\delta$  is applied. Following the duration of the first pulse and the separation  $\Delta$  time, the second pulse of equal amplitude but opposite gradient direction is induced, in the case of PGSE, this is accomplished by using a  $180^\circ$  refocusing pulse between the two gradients, and then the second pulse of the same gradient direction is applied (Buxton, 2009). The purpose of these two pulses is to spatially label each spin based on its average position during the activation time ( $\delta$ ). This is achieved thanks to the spins' intrinsic Larmor frequency,  $\omega_0 = \gamma B_0$ , in the presence of a steady magnetic field, where  $\gamma$  is the gyromagnetic ratio (a fundamental physical constant), and  $B_0$  is the strength of the static magnetic field. As shown in the non-diffusing case of Figure 2-1, if the spins did not diffuse, the second pulse would precisely cancel out the first pulse's effect. The net result would be the same as if no gradient pulses were applied since the net magnetization measured value in an MRI experiment is proportional to the spins' coherence in their precession rate, i.e. when their dephasing can be dismissed. On the other hand, in the presence of diffusion, each spin is likely to be in a different position when the second pulse is applied than when the first pulse was applied. As a result, the effects of the two gradient pulses do not balance, leaving each spin with a random phase offset that is proportional to how far it displaced between the two pulses, so the frequency  $\omega$  becomes spatially dependant as shown in the formula:

$$\omega = \omega_0 + \gamma(\mathbf{g} \cdot \mathbf{r}), \quad 2-8$$

where  $\mathbf{r}$  is the local displacement, and  $\mathbf{g}$  is the non-normalized gradient orientation.

Eq. 2-8 gives us a simple measurement of the phase shift caused by a single molecule's displacement. Now, by considering the cumulative phase shift of a single particle  $i$  during the first gradient block (starting at the time  $t = t_1$ ), the cumulative phase shift of a particle  $i$  at time block  $\tau = t_1 + \delta$ , and preceding the  $180^\circ$  refocusing pulse, can be defined as:



$$\phi_i(\tau = t_1 + \delta) := \gamma B_0 \tau + \gamma \int_{t_1}^{t_1 + \delta} \mathbf{g}(t) \cdot \mathbf{z}_i(t) dt, \quad 2-9$$

where term  $B_0$  denotes the static field contribution to the phase shift; the term  $\mathbf{g}(t)$  denotes the time dependent applied gradient, and  $\mathbf{z}_i(t)$  is the molecule's displacement at time  $t$ . As a result of the second term of the equation, the degree of dephasing caused by the gradient pulse is proportional to the type of nucleus (i.e.  $\gamma$ ), the gradient strength, the gradient time, and the spin displacement along the gradient direction.

As shown in Figure 2-1, at the beginning of a PGSE sequence, a  $90^\circ$  pulse is applied, which provokes that the diffusion-sensitizing-gradient — defined as a constant value  $\mathbf{g}(t) = \mathbf{g}$  in PGSE — to have a positive phase shift effect on the spins. The gradient vector  $\mathbf{g}(t)$  will affect the spin phase proportionally to the displacement along the gradient direction. This means that a displacement orthogonal to the gradient direction does not affect the spin phase, while a displacement parallel to the gradient direction has the most significant phase shift effect. In the simplified case of a linear and constant magnetic gradient, as in the case of PGSE, the gradient magnitude is constant over time for each block; thus, if we describe  $\mathbf{z}_i(t)$  as the displacement along the gradient direction (projection over the gradient direction), Eq 2-9 can be rewritten as follows:

$$\phi_i(\tau = t_1 + \delta) = \gamma B_0 \tau + \gamma g \int_{t_1}^{t_1 + \delta} z_i(t) dt, \quad 2-10$$

where the gradient magnitude is now constant and proportional to the magnitude. Finally, as explained above, PGSE is separated into two main blocks; thus, at the end of the echo sequence, the total phase shift of spin  $i$ , is given by:

$$\Phi_i(\tau, \delta, \Delta) = \gamma B_0 \tau + \gamma g \left\{ \int_{t_1}^{t_1 + \delta} z_i(t) dt - \int_{t_1 + \Delta}^{t_1 + \delta + \Delta} z_i(t') dt' \right\} \quad 2-11$$

Finally, the relation between the attenuation of the MR signal and the phase distribution of a spin ensemble is given by the formula (Price, 1997; Hall, 2009):

$$S(G, \delta, \Delta) = S(0, \delta, \Delta) \int_{-\infty}^{\infty} P(\Phi) e(i\Phi) d\Phi, \quad 2-12$$

where  $S(0, \delta, \Delta)$  is the signal in the absence of a gradient field, and  $P(\phi)$  is the distribution of the total phase shift from Eq 2-11. Finally, if we consider the real-valued part only of the equation:  $e(i\phi) = \cos(\phi) + i \sin(\phi)$  as in (Price, 1997), this results in the definition of the normalized diffusion signal as follows:

$$S(G, \delta, \Delta) = S(0, \delta, \Delta) \int_{-\infty}^{\infty} P(\phi) \cos(\phi) d\phi. \quad 2-13$$

The last expression describes how the PGSE mechanism works in particular. As seen in the equation above, the phase shift caused by the static field cancels. Without diffusion, the phase shifts caused by the two gradient pulses also cancels; thus,  $\phi_i = 0$  for all labelled particles  $i$  and since  $\cos(\phi) = 1$ , the maximum signal is obtained. At the signal level, the result of all the previous factors is a signal attenuation ( $A = S(G, \delta, \Delta)/S(0, \delta, \Delta)$ ) that can be interpreted by a factor that depends on the value of  $D$ . If we assume that the distribution of the spin dephase is Gaussian, as is the case of free diffusion, the attenuation behaviour is a mono-exponential decay (Price, 1997):

$$S(b, D) = e^{-bD} \quad 2-14$$

where the factor  $b = (\gamma G \delta)^2 (\Delta - \delta/3)$ . This value contains all of the PGSE protocol's amplitude and timing parameters. In practice, the local tissue diffusivity in a given direction can be calculated by evaluating two signals, one without a gradient applied ( $b = 0$ ) and another with a relatively large  $b$ -value. The ratio of the two signals is called the attenuation factor  $S(b, D)$  and it depends on the apparent local diffusion.

### **NMR diffusion contrast in the brain's tissue**

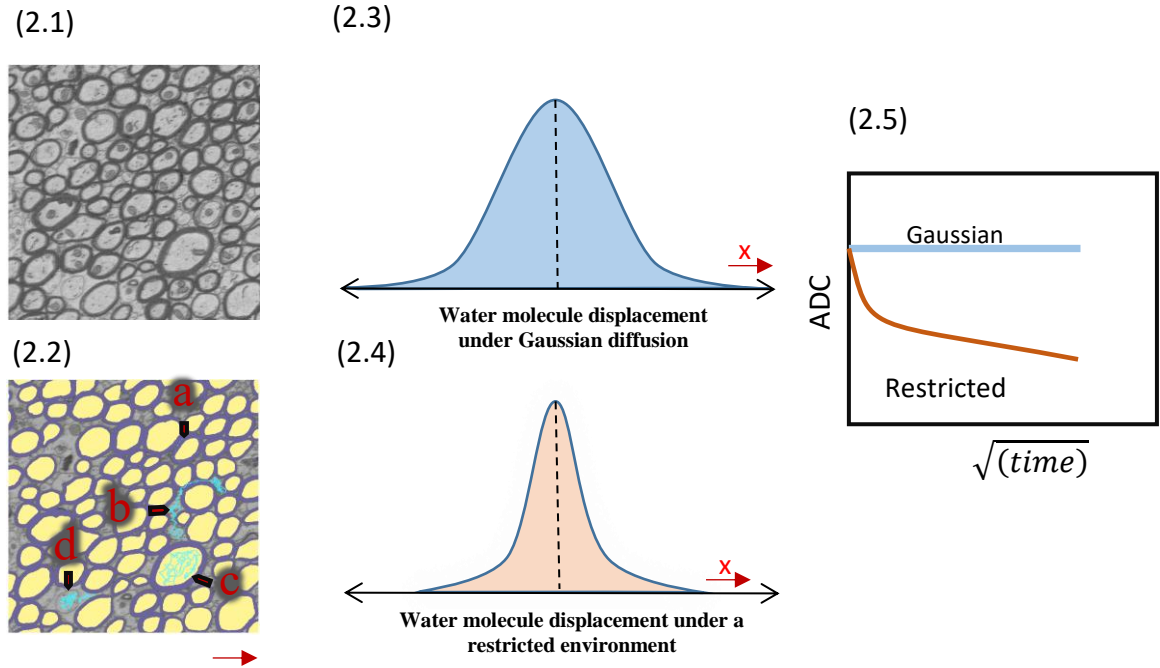


Figure 2-2 Water diffusion compartments characteristics

Panel 2.1) shows an electron microscopy image of the mouse corpus callosum showing the base structure of the myelinated axons. Panel 2.2) displays the restricted water compartments (yellow) by the myelin lamellae (purple). An illustration is shown of the water molecule motion in four distinctive compartments: a) trapped water in the myelin lamellae, b) in the extra-axonal space, c) intra-axonal space, and d) water exchange in non-myelinated axons. In the case of diffusion constrained by microstructure obstacles, the displacement distribution becomes sharper (2.4) In comparison with the distribution of free water, or even the extra-axonal space (2.3). As a result, the diffusion coefficient appears reduced and capped by the pore size (2.5).

In in-vivo conditions, the water diffusion coefficient is approximately  $2.5 \times 10^{-3} mm^2/s$ , then, from Eq 2-3, we can see that in free water, half of the particles in the media will displace by at least  $15 \mu m$  in a given direction at after 50 ms, which is about the average echo period of a PGSE protocol. On the other hand, diffusion in biological tissue is not unrestricted but is constrained by many barriers, such as cell membranes that restrict the mobility of water molecules and result in a lower ADC (see Figure 2-2) To interpret the decay with respect to the ADC, it is important to understand the water compartments inside the tissue microstructure. Figure 2-2 panel b) shows examples of the most prominent water

compartments described in the brain's white matter, which correspondingly spawns four of the main sources of contrast in DW-MRI, described below.

**No diffusion (static water pools):** In the presence of no diffusion, the maximum magnitude of the signal is obtained since the effect of the magnetization gradients is nullified for each spin. This case may arise in small restricted structures such as the myelin lamellae (Dortch *et al.*, 2013; Brusini, Menegaz and Nilsson, 2019) and other cell bodies (Innocenti, Caminiti and Hof, 2010) where the water diffusivity is low and thus considered static (see Figure 2-2, panel 2.2 a)). However, the small volume and typically low T2 relaxation times have made this compartment neglected or ignored from the theoretical microstructure models (Tax *et al.*, 2020).

**Free diffusion:** In the presence of free diffusion (random walk with no restrictions), the displacement distribution of free water molecules is time-dependent and spreads as a Gaussian distribution that dilates (Eq. 2-3). This type of diffusion, which is mainly assumed to occur in the brain's CSF and other isotropic compartments (Panagiotaki *et al.*, 2012), can be accurately modelled using a mono-exponential decay as a function of the b-value, as is shown in Eq. 2-14.

**Hindered diffusion.** As shown in Figure 2-2, in a highly concentrated environment densely packed with membrane obstacles but still allowing for diffusion, the displacement of water molecules no longer follows a Gaussian distribution. Thus the signal decay cannot be adequately represented by a mono-exponential decay. This phenomenon, which is often associated with the extra-cellular space (ECS), is referred to as *hindered diffusion*. To estimate the degree of diffusion hindrance in the ECS proportional to a free medium, the *tortuosity* — formulated as the square root of the ratio of the apparent extra-cellular diffusion coefficient to that of the free medium (Nicholson, 2001) — has been used to calculate the degree of diffusion hindrance in the ECS proportional to a free medium. Several studies using iontophoresis have measured the tortuosity of the brains' ECS, reporting tortuosity values of around 1.6, which corresponds to a factor of  $\frac{1}{2.6}$  from that of the water in the CSF (Nicholson, 2001); however, the true measurable tortuosity value of water molecules may still change. Of all the factors that contribute to the hindrance in the ECS — such as the extra-cellular matrix structure and trapped or transient water molecules

in the cell surface; — the ECS geometry may be the most important (Tao and Nicholson, 2004; Syková and Nicholson, 2008). The hindrance will be affected by the ECS geometry mainly by the extra-cellular volume fraction and the shape of the cells since water molecules are forced to take paths around cellular obstructions as their diameter increases due to cell swelling or increased cell packing density (cellularity), for example. Such effects have been one of the points of interest and focus of the work on this thesis, as explained in the following chapters.

**Restricted Diffusion:** Restricted diffusion is the fundamental signal characteristic of microstructure models for axon diameter mapping, as it provides details about the water molecules enclosed within the axons. Restricted is a term that has historically been used to refer to the trapping of water molecules inside an enclosed compartment (e.g., the axons' myelin layer and cell membranes) summarized in the intra-axonal or intra-cellular space (ICS). The signal decay associated with this space is fundamentally different from the signal decay associated with free and hindered water diffusion since the net squared displacement of water molecules is no longer linear over time and thus non-Gaussian (see Figure 2-2). Moreover, assuming an impermeable compartment, the time evolution of net displacements — and thus the phase shift of net spins — is highly dependent on the size and shape of the restricting compartment, the intrinsic intracellular diffusivity, and the total diffusion time. Such behaviour contrasts to that of the extra-cellular water, where extra-axonal ADC is independent of diffusion time — at least for short enough diffusion times — (Jensen *et al.*, 2005) since the effective diffusion coefficient for intracellular water decreases with the diffusion time. This because, as the diffusion time increases, a more significant proportion of spins are sensible to the membrane barriers and “bounce off”. Because of this, the restricted diffusion must be characterized considering the ensemble of factors that contributed to the “non-gaussianity” of the molecules' net displacement, such as the diffusion time, the membrane permeability (low or high exchange regime) and the size of restricting cellular compartments. For example, in the short-time limit below 1 or 2 ms, the diffusion is mainly unrestricted since a large amount of the water molecules are unable to reach the cell barriers, except for a small minority of molecules confined close to cell membranes or other barriers. Conversely, in the long-time limit above the cell residence time ( $> 500$  ms) of the intra- and extra- axonal compartments, the diffusion

cannot be longer compartmentalized because of the active exchange between intra- and extra-cellular water. In DW-MRI, however, the typical acquisition time ranges between 30 to 100 ms (Mitra, Sen and Schwartz, 1993; Latour *et al.*, 1994; Mitra and Halperin, 1995), which is long enough for the particles to sense the axon's myelinated barriers (0.1 to 2  $\mu\text{m}$ ) or cell membranes but short enough to be relatively small in comparison to the exchange between intra- and extra- cellular compartments (Dortch *et al.*, 2013; Nilsson *et al.*, 2013).

## 2.5 White matter signal models

The diffusion compartments described above can be used to characterize the MRI signal and provide important information about the white matter tissue microstructure of the brain. This characterization will then enable the ADC of the different compartments to be related to the underlying microstructure. The ADC has historically been used successfully to diagnose brain regions affected by ischemic stroke (Sorensen *et al.*, 1996; Mori and Barker, 1999; Sotak, 2002). However, over the last decade, plenty of new models have been proposed to characterize, for instance, the degree of non-Gaussian net diffusion in a voxel, usually referred to as kurtosis, or more specific microstructure features such as axon diameter in white matter — CHARMED, AxActiveAx (Alexander *et al.*, 2010; Dyrby *et al.*, 2013), AxCaliber (Assaf *et al.*, 2008) — or neurite orientation dispersion (NODDI) (Zhang *et al.*, 2012). In the following section, we will discuss several models used in the Thesis' contribution work.

### Diffusion Tensor

The Diffusion Tensor (DT) (Le Bihan *et al.*, 1986) is one, if not the most, used model for DW-MRI. In its essence, DTI extends the simplified model derived from Fick's laws to a

three-dimensional diffusion case, replacing the scalar coefficient  $D$  with an axis-symmetrical tensor  $\mathbf{D}$ :

$$\mathbf{D} = \begin{pmatrix} D_{xx} & D_{xy} & D_{xz} \\ D_{yx} & D_{yy} & D_{yz} \\ D_{zx} & D_{zy} & D_{zz} \end{pmatrix} \quad 2-15$$

Then, Einstein's equation (Eq. 2-7) can be rewritten in terms of the total displacement vector  $R$  over time  $\tau$  as:

$$\mathbf{D} = \frac{1}{6\tau} (RR^t) \quad 2-16$$

The solution of the Gaussian diffusion probability distribution function (PDF) is then formulated as

$$P(r|r_0, \tau) = \frac{1}{\sqrt{(4\pi\tau)^3 |\mathbf{D}|}} \exp\left(-\frac{(r - r_0)^T \mathbf{D}^{-1} (r - r_0)}{4\tau}\right), \quad 2-17$$

From this expression,  $\mathbf{D}$  can be viewed as a covariance matrix of the molecule's random displacement, which then can be estimated using linear regression at the signal level. Since  $\mathbf{D}$  is a symmetric tensor, we have then a system with six unknowns, which in theory requires at least six independent measurements and one unweighted  $b_0$  image for normalization. Thanks to its simplicity, DT estimation has been extensively used in both clinical and research applications (Horsfield, Jones and Horsfield, 2002; Roebroek *et al.*, 2008; Ramírez-Manzanares *et al.*, 2010; Rafael-Patiño, Ramírez-Manzanares and Rivera, 2011; Zhou *et al.*, 2012). As part of this thesis work, we made use of DT derived measurements as hand-crafted features for axon diameter and volume fraction estimation (Rafael-Patino, Yu, *et al.*, 2020), such as the fraction anisotropy (FA) and mean diffusivity (MD), defined in terms of the tensor's eigenvalues  $\lambda_1, \lambda_2, \lambda_3$  decomposition as follows,

$$FA = \frac{\sqrt{3}}{\sqrt{2}} \sqrt{\frac{(\bar{\lambda} - \lambda_1)^2 + (\bar{\lambda} - \lambda_2)^2 + (\bar{\lambda} - \lambda_3)^2}{\lambda_1^2 + \lambda_2^2 + \lambda_3^2}}, \quad 2-18$$

$$MD = \bar{\lambda} = \text{trace}(D)/3. \quad 2-19$$

The FA is related to the amount of diffusion anisotropy of a DW-MRI image voxel, ranging from 0 (isotropic) to 1 (anisotropic). However, DT-based maps are limited by their assumption of a homogeneous and Gaussian diffusion, which is not the case of the brain's white matter structure at the typical diffusion times used in clinical DW-MRI acquisitions.

## Diffusion Kurtosis

For more restricted media, such as the case of the intra-axonal space of the white matter, the diffusion kurtosis (DK) (Jensen *et al.*, 2005) can be helpful to measure the degree of “non-gaussianity” of the diffusion PDF. A large, measured kurtosis is then related to the sharpness of the PDF, as shown in Figure 2-2. At the signal level, the diffusion DK is expressed as:

$$\ln(S/S_0) = -bD_{app} + \frac{1}{6}b^2D_{app}^2K_{app} + \mathcal{O}(b^3) \quad 2-20$$

where  $K_{app}$  refers to the apparent kurtosis.

## Compartment models

Microstructure modelling relies on explicit models of the tissue's biological structures inside a voxel. As previously stated, DT reduces the complexity of the tissue to a single tensor from which eigenvalues and eigenvectors can be extracted to obtain diffusion features — such as the FA and MD — that represent several properties of the WM microstructure. On the other hand, such metrics are non-specific and do not capture the



finer details of the DW-MRI signal. More complex tissue models allow for the estimation of specific microstructure properties such as mean axon diameter (Alexander *et al.*, 2010), axon diameter distributions (Assaf *et al.*, 2008), intra-axonal and extra-axonal volume fractions, and neurite dispersion (Zhang *et al.*, 2012). Those models use the following equation to describe the DW-MRI signal  $S$  as a mixture of compartments:

$$S = \sum_{i=1}^N f_i S_i; \quad s. t. \quad \sum_i f_i = 1, \quad 2-21$$

where  $N$  is the number of compartments and the term  $f_i S_i$  is the signal of the  $i^{th}$  compartment, weighted by its volume fraction. These models are referred to as compartmentalized methods because the signal is modelled as a weighted average of each microstructure compartment's independent contributions. Notice that those models consider microstructural structures that have a few micrometres of characteristic dimension (like the axon's diameter) and decompose the signal — averaged in a voxel of a few millimetres — onto this linear formulation.

### **Axon diameter model.**

Among the first compartmentalized models proposed for DW-MRI were the **Composite Hindered And Restricted Model of Diffusion (CHARMED)** (Assaf and Basser, 2005). The WM in this model is represented by two compartments, one hindered for extra-axonal space and one restricted for intra-axonal space. The total signal produced by diffusion in the compartments is the following formula:

$$S(\mathbf{q}, \Delta) = f_h S_h(\mathbf{q}, \Delta) + f_r S_r(\mathbf{q}, \Delta), \quad 2-22$$

where the sub-indices  $h, r$  indicate the hindered and restricted compartments, respectively. This model makes several assumptions about the nature of each compartment, i) it assumes no water exchange between compartments, and thus a simple linear formulation can be used; ii) the restricted compartment representing the WM axon fibres are simplified as

cylinders of constant radii, and the signal from the restricted diffusion perpendicular to the cylinder is taken from (Van Gelderen *et al.*, 1994) formulation with diffusion coefficient  $D_{\perp}$ ; iii) the diffusion parallel to the orientation of the cylinder is modelled as a Gaussian diffusion with diffusivity independent to the parallel diffusivity, and iv) the diffusion in the hindered compartment is assumed to be unrestricted but anisotropic, which is modelled by a tensor  $\mathbf{D}_h$  with parallel diffusivity and perpendicular diffusivity, and with the principal diffusion direction aligned with the WM fibres. According to (Assaf and Basser, 2005), the volume fraction of the restricted compartment distinguishes between white matter (WM), grey matter (GM), and cerebrospinal fluid (CSF) throughout the brain. In addition, since the water particles are trapped within axons, the signal at high b-values is mainly attributed to intra-axonal water, and the signal from extra-axonal water is completely attenuated.

**The AxCaliber** model (Assaf *et al.*, 2008) is an extension of CHARMED; it estimates the distribution of axon diameters within a voxel. This work is motivated by the relationship between the diameter of myelinated axons and their conduction velocity. The framework is similar to CHARMED, except that the restricted compartment is replaced by a probability function representing the diameter within each compartment. According to (Barazany, Basser and Assaf, 2009), the AxCaliber model significantly overestimates the mean axon diameter compared to histology, and at the same time, the axonal volume fraction is grossly underestimated. In addition, in this model, it is assumed that the intra- and extra-axonal compartments have the same T2 relaxation time because it cannot be estimated from DW-MRI data alone. However, it has been reported that the T2s of these compartments are different (McKinnon and Jensen, 2019).

The **ActiveAx** model was proposed as a simplified version of AxCaliber in (Alexander *et al.*, 2010), where one single mean axon radius is assigned at each voxel, and the intra-axonal and parallel extra-axonal diffusivities are similar. In contrast to CHARMED, signals are acquired at a range of b-values and orientations to provide an estimate that is not orientation-based. The original framework was improved in (Dyrby *et al.*, 2013) by using ad-hoc protocols optimized to enhance the sensitivity to small axons diameters. In addition to the model firstly proposed, the CSF is modelled using free and isotropic diffusion,

whereas the water trapped inside glial cells is modelled using an isotropic restricted diffusion compartment.

The accuracy and feasibility of the axons' diameter mapping have significantly been discussed in the DW-MRI community (Hui *et al.*, 2011; Nilsson *et al.*, 2012, 2017). A comparison study of the WM models for axon diameter estimation on ideal data (Panagiotaki *et al.*, 2012) suggested that at least three compartments are necessary.

### **Fibre dispersion and orientation distribution**

The **Neurite Orientation Dispersion and Density Imaging** (NODDI) model was proposed in (Zhang *et al.*, 2012) to model the fibre dispersion estimation using three compartments. In here, the intra-axonal compartment is modelled with sticks (the perpendicular diffusivity is nullified,  $D_{\perp} = 0$ ) oriented along a principal direction, with the fibre dispersion within voxels modelled by a Watson distribution; and the extra-axonal compartment is modelled as hindered Gaussian diffusion, with the apparent diffusion coefficient weighted using the Watson distribution. The authors claimed that the intra- and extra-axonal diffusivities take into account the morphology of the neurites because an increase in the dispersion coefficient reduces both diffusivities. The last compartment then models the CSF as isotropic Gaussian diffusion. One major drawback of this model is the fixed value of the intra-axonal and parallel extra-axonal diffusivities. The authors in (Jelescu *et al.*, 2016) relaxed this assumption, but the fitting becomes rapidly unstable, and the precision decreases. Additionally, the model does not cope with voxels having crossing fibres because it is assumed that the axons are dispersed along one main direction. In (Tariq *et al.*, 2016), the Watson distribution is replaced by the Bingham distribution to allow anisotropic dispersion in the main direction, while no assumptions are made on the orientation distribution.

### **Fast microstructure parameters estimation.**

The methods described in the previous section exploit simple microstructure geometry models that allow deriving analytical solutions of the DW-MRI signal under specific conditions. This limits the signals modelling to those simple cases where the solution to the Bloch-Torrey equation can be analytically solved for cases based on the narrow pulse approximation, such as for the diffusion in confined plane sheets (Tanner and Stejskal, 1968), cylinders (Neuman, 1974; John and Crank, 1979), and spheres (Murday and Cotts, 1968). In each case, each compartment has some parameters that are either fixed before the fitting or estimated during the optimization, e.g., the diffusion coefficient, the distribution of sphere radii within the voxel, or the permeability of the membranes. The final step of these methods is estimating the tissue parameters from the measured DW-MRI signal by optimising a loss function for the parameters mentioned above. Usually, this cost function is the sum of the mean squared differences between the measured signal of each component  $S_i$  and model-estimated signal  $\hat{S}$ :

$$\arg \min_{\theta} \mathcal{L} = \arg \min_{\theta} \sum_{i=1}^{N_q} \left\| S_i - \hat{S}(\theta) \right\|^2, \quad 2-23$$

where  $N_q$  is the number of measurements,  $\theta$  is the ensemble of parameters.

To solve models such as Eq. 2-23 efficiently, (Daducci *et al.*, 2015) introduced the AMICO (**A**ccelerated **M**icrostructure **I**maging by **C**onvex **O**ptimization) framework, in which any non-linear microstructure estimation problem is reformulated as a discrete regularized linear inverse problem, which can be solved using dedicated solvers that yield a global solution thousands of times faster. The following convex optimization problem is used to formulate the DW-MRI signal reconstruction:

$$\arg \min_{x \geq 0} \left\| Ax - \hat{S} \right\|_2^2 + R(x), \quad 2-24$$

where  $R(\cdot)$  regularizes the solution  $x$  and depends on the specific tissue model and microstructure signal response dictionary  $A$ . AMICO was first used to linearize ActiveAx and NODDI. Other studies continued the microstructure and diffusion modelling line by extending the framework towards more complex features such as the full axon diameter distribution (ADD) (Romascano *et al.*, 2020) and the estimation of the diffusion

coefficients in complex hindered compartments such as the extra-axonal space of the WM using a mixture of a non-parametric model. The former work showed that non-parametric and orientationally invariant ADDs could be reliably reconstructed from Pulsed gradient spin-echo (PGSE) data using this method (called *ActiveAx<sub>ADD</sub>*). Figure 2-3 shows a visualization of the mapping of the mean of the Axon Diameter Distribution (called streamline Axon Diameter Index, or mADI) for each streamline for the callosal connections of a human brain.

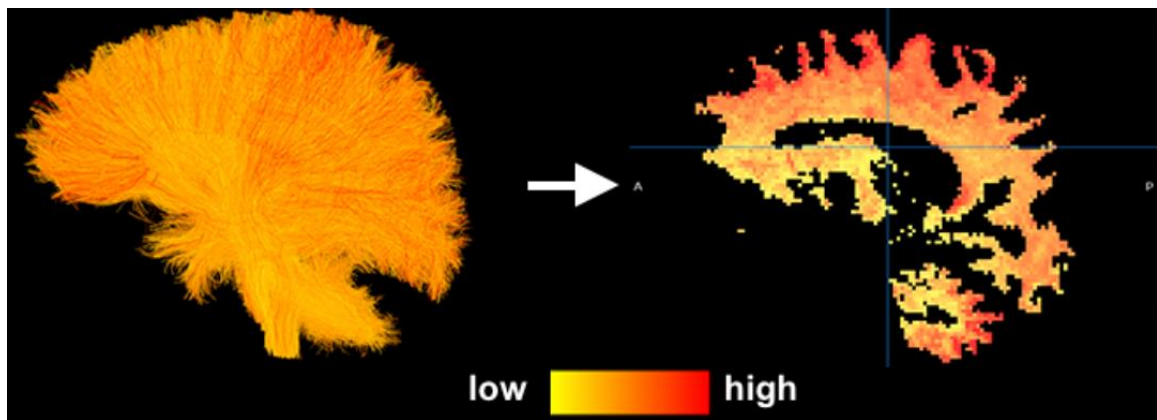


Figure 2-3 Streamline Axon Diameter Index (mADI).

Each streamline is coloured according to its mADI for a whole tractogram (left) and is projected to the voxel level (right).

The method, however, inherits common limitations of current microstructure models, particularly the lack of sensitivity to small axons because of the protocol limitations and the difficulty of disentangling intra-axonal and extra-axonal contributions, and simplification regarding the axonal geometry as parallel cylinders of constant radius.

## 2.6 DW-MRI Simulations

As addressed in the previous sections, DW-MRI microstructure modelling allows the link of the measured signal to the tissue's underlying microscopic properties. To further improve the information and analysis given by DW-MRI features, tests and validations of

acquisition methods in controlled environments are essential. For instance, to investigate the relationship between the MRI acquisition protocol and the substrate's features, to develop and optimize novel DW-MRI acquisition protocol, to quantify the tissue composition, to improve the estimation of local tissue orientation methods, and enhance WM tractography techniques (Close *et al.*, 2009; Lin *et al.*, 2016; Rensonnet *et al.*, 2019, 2020; Truffet *et al.*, 2020). Therefore, it is crucial to precisely understand how the microstructure influences the water diffusivity profiles and then use that knowledge to estimate the brain tissue properties on complex brain tissue accurately.

The ability to simulate DW-MRI signals for given synthetic tissue geometries can play a significant role in this context. In a first approach, the diffusion-weighted signal of individual axons and glial cells was modelled using the synthetic signal from simple geometries (packing of parallel cylinders and spheres). The advantage of using such geometries is that it is possible to derive analytical solutions for the diffusion coefficients in those geometries. Although these geometries helped to study first insights in isotropic and anisotropic diffusivity, they are not an accurate representation of the complex tissue's microstructure.

A second approach for the validation of the DW-MRI was the development of physical phantoms (Nath *et al.*; Fieremans *et al.*, 2008; Lavdas *et al.*, 2013; Khasawneh *et al.*, 2020). The most challenging problem here is replicating and manufacturing complex microstructure phantoms suitable for studying DW-MRI at the microscale. Even though these phantoms have proven helpful for DW-MRI experimentation and quality evaluation, developing physical models that accurately reflect the complex arrangement of axons that occurs in vivo remains a challenge.

Alternatively, **Monte-Carlo Diffusion Simulations** (MCDS), like the ones presented in this thesis, are tools used to study diffusion phenomena in scenarios where the analytical solutions cannot be computed due to their complexity. In contrast to other numerical methods, MCDS does not require an explicit model of the diffusion signal. Instead, it requires a substrate (geometrical representation of the diffusion media) in which the water

molecule displacement can be simulated. To the best of our knowledge, (Lipinski, 1990) presented the first analysis of extra-cellular diffusion in brain tissue using MCDS. In this study, binary contours were drawn from 2D histological data to serve as irregular intra-cellular barriers. Most studies after this one simplified the extra-cellular space representation as a series of restricted corridors in the orthogonal plane of the axonal direction and unrestricted parallel to them. Furthermore, the intracellular compartment is typically modelled as a series of parallel hollow cylinders with constant radii or radii sampled from a distribution based on histological evidence. Recent research (Nilsson *et al.*, 2012; Reisert *et al.*, 2017; Andersson *et al.*, 2021) suggests that such simplifications fail to capture the complexity of white matter’s axonal structures and its diffusion properties. By introducing regular undulations in the intra-axonal compartment, researchers were able to obtain shifts in the diffusion signal and parameters derived from the diffusion tensor, such as the fractional anisotropy (FA) and mean diffusivity (MD). However, because of the high computational burden and lack of available resources, the DW-MRI community has not widely adopted such methods. As a result, more realistic diffusion simulations are underutilized.

In addition to the computational burden, one subsequent challenge in using microstructure MCDS is replicating the complex geometry of the WM tissue. Nevertheless, several studies emerge to investigate the immense complexity of real axonal morphology in 3d using ex-vivo Electron Microscopy (EM) (Abdollahzadeh *et al.*, 2019, 2021; Andersson *et al.*, 2021). Compared with previously reported trends that studied axon diameter and g-ratio in one image, the 3d detailed reconstructions show that real WM contains axons with complex morphology on an individual axon basis: undulation beading, non-circular cross-sections, orientation dispersion, and crossing bundles. Thanks to this new understanding of the structural components of the white matter, several studies introduced more microstructure complexity into the numerical phantoms, like beading (Balls and Frank, 2009), spines (Palombo, Alexander and Zhang, 2019), undulation (Nilsson *et al.*, 2012), water myelin exchange (Brusini, Menegaz and Nilsson, 2019), and interdigitating packing (Ginsburger *et al.*, 2019; Rafael-Patino, Romascano, *et al.*, 2020). Nevertheless, large substrate size (number of axons) and high packing density in the WM are not solved yet.

In the following section, we address the basic theory behind DW-MRI Monte-Carlo simulations, the challenges to implement a robust and optimized simulator, and critical problems and challenges that have been addressed in this thesis.

## DW-MRI Monte-Carlo Simulations

Monte-Carlo experimentation is a non-deterministic method used to approximate complex mathematical expressions or models. The base of a Monte-Carlo method is to sample the mathematical expression in order to obtain the desired approximation randomly. To approximate the DW-MRI contrast in challenging environments via Monte-Carlo sampling, an MCDS uses a computational geometric model of a complex tissue *in silica*, then mimics the diffusion dynamics (the evolution in time of the proton diffusion density) of a large population of water spins within such environments, and simulates the resulting MR signal explained by Eq. 2-13. To approximate the magnetic resonance signal, a large population of uniformly distributed water spins is needed. Following that, each individual spin is tracked over time, and its local displacement and total magnetization are updated according to the DW-MRI protocol's parameters. Finally, the signal decay can be computed as a function of the ensemble of spins. This approximation can theoretically be achieved in great detail if the geometry model is accurate enough to reflect the desired tissue microstructure or substrate. One advantage of this approach is that we can keep track of all dynamical events, allowing us to study the diffusion and magnetization processes and the intrinsic interaction between parameters. A simulation then can be divided into these two main steps, the particle dynamics simulation and the signal computation. The following section will explain the main components of these two steps.

### **Particle Dynamics Simulation**



The particle dynamics simulate the diffusion process of water particles in a certain environment, usually called the substrate. At the beginning of the simulation, the particles are uniformly placed inside the defined substrate's voxel or substrate's limits. This way, the number of particles in all compartments is proportional to the defined volume fractions. If necessary, the local position of each particle can be tracked to separate the signal contribution of each compartment by, for example, tracking if the particle is inside a given compartment. The major challenge of this step is to build a fast and robust simulation that can reproduce, with enough accuracy, the desired geometry. We need to define this geometry and its microstructure features in which the water is diffusing. On the other hand, as in any Monte-Carlo method, we need a considerable large number of samples to estimate our objective function. Our samples here are the particles diffusing in each time step as random walkers, colliding and interacting with the barriers of the substrate. Thus, in each step of the simulation, the direction is randomly sampled using a fixed step length. At each time step, the particles that collide with the substrates barriers are elastically reflected depending on the properties of the barriers. For example, we can consider the elasticity of the barrier or even a percolation coefficient that controls exchange time between compartments. This results in the following sequence of steps as explained in (Hall and Alexander, 2009):

- I. Spin initial distribution. The water spins need to be initialized in the corresponding substrates limits, which define the simulated voxel size. In a substrate made of multiple compartments, the initialization must be done uniformly in all compartments, such that the resulting density of particles is proportional to the volume fraction of each compartment. The *number of particles* or the *density of particles* is an essential parameter in a Monte-Carlo simulation — which is addressed in the following chapter — since it directly affects the convergence of the signal estimation (Rafael-Patino, Romascano, *et al.*, 2020).
- II. Water spins random diffusion. Once the particles are uniformly placed at a given position at time 0, the molecules will undergo a reflected Brownian motion. To

simulate the random motion of a given spin, each spin molecule will move a given distance ( $l$ ) in a random direction over the sphere at each time step. This can be done by sampling a random set of angles  $\phi$  and  $\theta$  as follows:

$$\begin{aligned}x &= \sin \phi \cos \theta, \\y &= \sin \phi \sin \theta, \\z &= \cos \phi,\end{aligned}\tag{2-25}$$

where  $\phi$  is the elevation angle ranging from  $[0, \pi]$  radians, and  $\theta$  is the azimuth angle from  $[0, 2\pi]$  radians. The step size or step length  $l$  defines the effective diffusion displacement over the duration of each time step. The step length needs to be computed using the Einstein equation (Eq. 2-6) as follows:

$$l = \sqrt{\frac{6Dt_s}{T}},\tag{2-26}$$

where  $D$  is the desired diffusion coefficient,  $T$  is the number of steps to compute, and  $t_s$  is the total simulation time of the simulation. The resulting step vector is then defined as  $\Delta\vec{x} = l * (x, y, z)$ .

- III. Collision detection: At each time step, the particle's position is updated based on the substrated defined barriers and properties. The main operation relies on verifying whether the resulting position after the step crosses any substrate's barrier. In the lack of a collision, the spin position can be updated as  $\vec{x}_n = \vec{x}_{n-1} + \Delta\vec{x}$ . On the other hand, if any barrier is crossed, the spin is iteratively and elastically reflected at the collision point — or ignored depending on the barrier's permeability — until no barrier is crossed or the total step length is travelled.

It is important to note that the dynamic simulation and the pulse sequence must be time-congruent, meaning that the overall duration of the dynamics simulation should match the duration of the pulse sequence calculation.

### **Signal Computation**

The cumulative net magnetic contribution of the spatially dependent magnetic gradients and thus the resulting phase shift of each particle must be computed during the particle simulations. This is easily described by referring to the pulsed gradient PGSE sequence, PGSE. As previously mentioned, a PGSE sequence consists of two magnetic gradient blocks with the same delta duration. After a  $90^\circ$  initial pulse, the first gradient block is enabled, and this combination induces a quantifiable effect on each particle called a phase shift. Following the application of the initial gradient, a  $180^\circ$  pulse is applied, which acts as if the gradient's sign is flipped and the phase shift contribution is now negative. We can compute this effect numerically on the cumulative phase shift formula (Eq. 2-13) for each one of the spins as follows:

$$\Phi(t) = a(t)\gamma g(t)z(t) \quad 2-27$$

where a phase shift is computed in each step as a function of the time-step  $t$ ,  $g(t)$  is the magnitude of gradient vector, which is constant for the PGSE sequence,  $z(t)$  is the spin's displacement along the gradient direction at time  $t$ , defined as the projection of  $\vec{x}(t) - \vec{x}_0$  in that direction, where  $\vec{x}_0$  is the position at time  $t = 0$  and  $\vec{x}(t)$  is the position at time  $t$ ;  $\gamma$  is the gyro-magnetic ratio;  $\delta t$  is the duration of a time step, defined as the diffusion time divided over the number of steps; and finally  $a(t)$  is a function that indicates the gradient sign and magnitude. For example, in a PGSE sequence,  $a(t)$  is equal to 1 in the first gradient block, and -1 on the second gradient block after the  $180^\circ$  pulse. The function  $a(t)$  can then be easily adjusted for any other type of sequence with multiple refocusing times or arbitrary waveforms shapes as in (Truffet *et al.*, 2020) (See Chapter 6).

Throughout the simulation, each one of the spins accumulates the phase shift, and the final signal is then generated by the contribution of the conjoint phase shift of all the spins simulated:

$$S/S_0 = \frac{1}{N_s} \sum_{N_s} e^{-i \sum_t^{N_t} \phi(t) dt}, \quad 2-28$$

where  $N_s$  is the total number of spins,  $N_t$  is the number of time steps in the simulation, and  $dt$  is the step duration, defined as the total diffusion time divided by the number of steps

taken  $N_t$ . Equation 2-28 is analogous to Equation 2-12, so, in order to obtain a real-valued signal, we can take only the real part of the signal as explained in (Price, 1997) resulting in the following expression:

$$S/S_0 = \frac{1}{N_s} \sum_{N_s} \cos \left( \sum_t^{N_t} \phi(t) dt \right) \quad 2-29$$

### Simulation computation complexity

---

#### **Algorithm 1** MCDS core algorithm

---

```

1: procedure BASICSIMULATION
2:    $N_s \leftarrow$  Number of spins
3:    $N_t \leftarrow$  Number of time-steps
4:    $N_g \leftarrow$  Number of acquisitions
5:   for each  $N_s$  spins do:
6:     for each  $N_t$  time step do:
7:       UpdateSpinPosition(...)
8:     for each  $N_g$  acquisition do:
9:       UpdateTotalDephase(...)
10:  for each  $N_g$  acquisitions do:
11:    ComputeDWSignal(...)

```

---

Alg. 2-1 DW-MRI Monte-Carlo Simulatoins algorithm.

The algorithm shown in Alg. 2-1 summarizes all of the fundamental steps required in a diffusion simulation. Previously, in (Hall and Alexander, 2009), the simulation complexity was defined as the number of steps multiplied by the number of simulated particles ( $U = N_t * N_s$ ). From an experimental standpoint, this formula helps summarize the relationship between sample size and temporal resolution in terms of estimation quality; however, the computational complexity is not adequately described. This is because such complexity considers only the first two nested loops and implicitly assumes that the position update has complexity  $\mathcal{O}(1)$ , which is valid only when there is no substrate, i.e., free diffusion. In (Rafael-Patino, Romascano, *et al.*, 2020), the following asymptotic complexity formula

was proposed:  $\mathcal{O}(N_s * N_t * N_o) + \mathcal{O}(N_s * N_g)$  ; which incorporates the effect of the collision detection in terms of the number of simulated obstacles ( $N_o$ ) and number of acquisitions ( $N_g$ ). From this expression, the number of particles  $N_s$  linearly increases the computational burden of a simulation. At the same time, the quality of the estimated signal will greatly depend on the number of sampled particles.

---

**Algorithm 2** Particle Position Update

---

```

1: procedure UPDATESPINPOSITION
2:    $\Omega \leftarrow$  List of Obstacles
3:   do
4:     for each obstacle in  $\Omega$  do
5:       checkForCollision(...)
6:       if collision detected then
7:         reflectTrajectory(...)
8:   while collision is detected

```

---

Alg. 2-2 Particle's position update function.

Alg. 2-2 shows the steps inside the *updateSpinPosition()* function. To assess the overall function's complexity of this function, the estimated collision probability must be estimated. However, the predicted collision rate is impractical to compute since it is dependent on the step duration, the number of obstacles, their size and packing density, and diffusion parameters. On the other hand, the method *checkForCollision()* has  $\mathcal{O}(N_o)$ , where  $N_o$  is the total number of obstacles — barriers defined as triangles, cylinders, or spheres — in the substrate. Spatial optimization procedures, such as Axis-aligned Bounding Boxes (AABB) or R-Trees, can optimize the collision detection by splitting and search the obstacle domain in  $\Omega(\log(N_o))$  for well balanced spatial structures (Agarwal *et al.*, 2001). By neglecting the complexity of the multiple reflections of a single step, we can summarize the complexity of the first two nested loops in Alg. 2-2 as  $\mathcal{O}(N_s * N_g * N_o)$ . Finally, since updating the total dephasing in each iteration can be done in constant time,

the second nested loop has complexity  $\mathcal{O}(N_s * N_g)$ , where  $N_g$  is the number of acquisitions (number of output signals). The overall simulation complexity can be written as:

$$\mathcal{O}(N_s * N_t * N_o) + \mathcal{O}(N_s * N_g) = \mathcal{O}(\max(N_s * N_t * N_o, N_s * N_g)) \quad 2-30$$

The number of particles  $N_s$  has the most significant impact since it scales the complexity in both terms; in addition, it is usually the biggest one, followed by the number of steps  $N_t$ . On the other hand, the number of acquisitions or output signals  $N_g$  is usually the smaller one and therefore, the complexity above can be usually reduced as  $\mathcal{O}(N_s * N_t * N_o)$ . Nevertheless, we cannot neglect it from the complexity above since it may have a more significant impact in application related to protocol optimization — as is shown in Chapter 4 — or q-space exploration, where a significant number of shells or sampling direction is needed. Finally, the number of obstacles  $N_o$  may variate from hundreds (Panagiotaki *et al.*, 2010) to several million as in the presented numerical phantom of Chapter 4.

# Chapter 3

## Robust and Realistic DW-MRI

### Monte-Carlo Simulations

---

#### 3.1 Overview

As discussed in the previous chapter, Monte-Carlo Diffusion Simulations (MCDS) have been broadly used as a ground truth method for microstructure model validation in Diffusion-Weighted MRI. However, as reported in previous studies, methodological flaws in the design of biomimicking geometrical configurations and stimulation parameters can result in biased approximations of the DW-MRI signal. Such pitfalls have an impact on the estimated signal reliability, as well as its validity and reproducibility as ground truth data. For instance, the number of simulated particles and time steps, and simplifications in the intra- and extra- axonal substrate are three of those crucial pitfalls encountered in the design of MCDS in the literature, which we investigated in our contribution Paper-1 (Rafael-Patino, Romascano, *et al.*, 2020) and summarize in here. This next chapter shows how the simulated signal and recovered microstructure features show significant changes when those parameters are modified and how we can tackle such limitations by generating more complex — and computationally expensive — simulations. As a result of this, and as part of the Thesis contributions, we developed a robust and open-source simulator to help improve the realism and reproducibility of DW-MRI simulations in the field, which paved the way for all of the studies presented in the following chapters of this thesis.

## 3.2 Design and Validation of MCDS

The number of simulated particles and the number of time measures, the intracellular geometrical representation, and the created extra-axonal space in terms of the substrate's size are discussed in this chapter as three significant pitfalls encountered in the design of MCDS in the literature. Each experiment depicts a potential bias produced in the computed signal when such simplifications are not adequately handled, affecting the signal's reproducibility.

### Number of samples in an MCDC

The first experiment measures the variance of the predicted signal as a function of the number of particles sampled in a substrate; to stress the importance of the number of simulated spins to the signal convergence. To do so, we calculated the errors of a collection of simulated signals with varying sample counts. In the intra-axonal space, the calculated errors were compared to the predicted analytical solution and a gold-standard estimate of the extracellular space. A substrate with 10,000 parallel cylinders with diameters sampled from a Gamma distribution,  $\Gamma(\kappa, \theta)$ , with shape,  $\kappa = 4.0$ , and scale,  $\theta = 4.5 \times 10^{-7}$ , was used, resulting in a mean diameter  $\mu = 1.8 \mu m$  with a standard deviation of  $\sigma = 0.9$ , using a packing algorithm similar to that described in (Hall and Alexander, 2009), resulting in a distribution of radii comparable to the ones found in the literature (Hui *et al.*, 2011; Benjamini *et al.*, 2016)

The analytical signal of the intra-axonal space was computed using the volume-weighted sum of the individual signals, so this substrate was used:

$$S_i = \frac{v_1 S_{c_{i,1}} + \dots + v_n S_{c_{i,n}}}{\sum v_j}, \quad 3-1$$



where  $S_i$  is the  $i^{th}$  acquisition,  $v_j$  is the volume of the  $j^{th}$  cylinder and  $S_{c_{i,1}}$  is the analytical signal of the cylinder obtained using the Gaussian Phase Distribution (GPD) approximation of the signal in cylinders for a given radius (Van Gelderen *et al.*, 1994). The resulting distribution of radii and the measured ground-truth intra-axonal signal are shown in Figure 3-1. Since there is no analytical model for the extracellular signal, the gold-standard was calculated using a large number of particles ( $20 \times 10^6$ ), and time-steps ( $2 \times 10^4$ ). These parameters were chosen based on previous findings (Rafael-Patino *et al.*, 2017) and research into the convergence properties of a larger number of particles and time measures (Hall and Alexander, 2009). In reality, we confirmed that the signal converges even with less demanding simulation parameters (i.e.  $1 \times 10^6$  particles and  $5 \times 10^3$  steps). In order to keep results as accurate as possible, however, we decided to use simulation parameters higher than the minimum required.

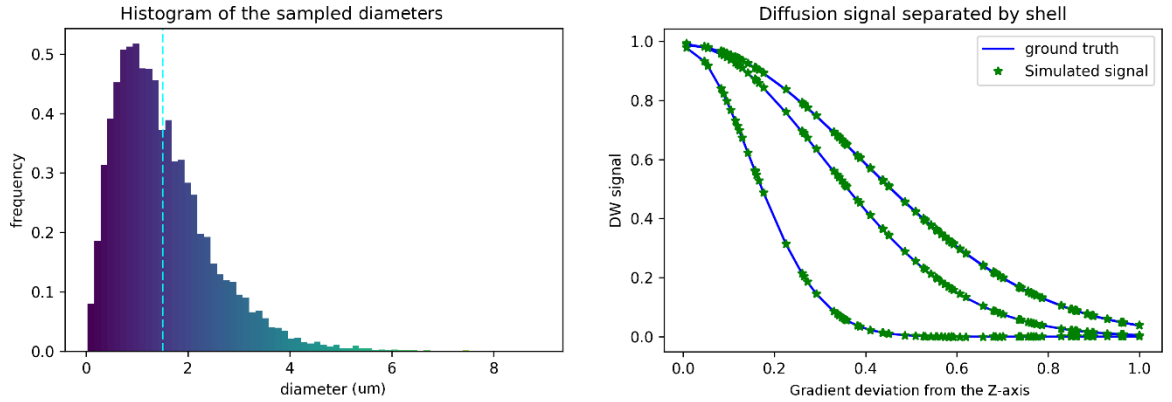


Figure 3-1: Gamma distributed radii and corresponding intra-axonal diffusion signal.

Left panel: The distribution of the sampled diameters, the dotted line marks the sampled distribution mean. Right panel: The computed ground-truth along with the simulated signal used for the intra-axonal space representation. The signals of each shell are ordered by the normalized distance to Z coefficient of the gradient direction.

The approximate signals were determined with the number of particles ranging from  $1 \times 10^3$  to  $1 \times 10^6$  particles, and the time-steps from  $1 \times 10^2$  to  $2 \times 10^4$  steps. For both simulations and ground-truth results, the diffusion coefficient was set to  $D = 0.6 \times 10^{-3} \text{ mm}^2/\text{s}$  (corresponding to an ex-vivo diffusivity), and  $TE = 0.054 \text{ s.}$ , for both the simulations and the ground-truth data. The ActiveAx PGSE protocol (Alexander *et al.*,

2017) was used, which consist of a four shell HARDI acquisition with 90 orientations per shell, each shell with the following parameters respectively, i)  $b=1930 \text{ s/mm}^2$ ,  $G = 140 \text{ mT/m}$ ,  $\delta = 0.010 \text{ s}$ , and  $\Delta = 0.016 \text{ s}$ ; ii)  $b = 1930 \text{ s/mm}^2$ ,  $G = 140 \text{ mT/m}$ ,  $\delta = 0.010 \text{ s}$ , and  $\Delta = 0.016 \text{ s}$ ; iii)  $b = 3090 \text{ s/mm}^2$ ,  $G = 131 \text{ mT/m}$ ,  $\delta = 0.007 \text{ s}$ , and  $\Delta = 0.045 \text{ s}$ ; iv)  $b = 13190 \text{ s/mm}^2$ ,  $G = 140 \text{ mT/m}$ ,  $\delta = 0.017 \text{ s}$ , and  $\Delta = 0.035 \text{ s}$ . Figure 3-1 right panel shows the plot of a diffusion signal obtained with this protocol separated by shell and ordered with respect to the angle with the main fibre axis (Z-axis).

A bootstrapping analysis was used:  $1 \times 10^3$ ,  $2 \times 10^3$ ,  $5 \times 10^3$ ,  $1 \times 10^4$ ,  $2 \times 10^4$ ,  $5 \times 10^4$ ,  $1 \times 10^5$ ,  $2 \times 10^5$ ,  $1 \times 10^6$ , and  $2 \times 10^6$  samples; and time-steps:  $1 \times 10^2$ ,  $5 \times 10^2$ ,  $1 \times 10^3$ ,  $5 \times 10^3$ ,  $1 \times 10^4$ , and  $2 \times 10^4$  to assess the variance of the error between estimations with different sample sizes. Signals from 50 repetitions were generated for each combination of sample size and time-steps. The Relative Mean Absolute Error (RMAE) was used to calculate the error between the ground-truth and each estimated signal, which was expressed as a percentage:

$$\text{RMAE}(S_{gt}, S_c) = \frac{100}{N_g} \sum_i^N \frac{|S_{gt}(i) - S_c(i)|}{|S_{gt}(i)|}, \quad 3-2$$

where  $S_{gt}$  is the ground-truth signal,  $S_c$  is the estimated signal and  $N_g$  is the number of acquisitions.

In addition, a complementary study of the temporal resolution (number of time steps) was performed using the same substrate and protocol. The estimated signals were computed using a total of  $N = 20 \times 10^6$  samples and then varying the number of time-steps. A bootstrapping analysis with 50 repetitions was performed in the same way as before, increasing the number of time-steps from  $1 \times 10^2$  to  $2 \times 10^4$ .

## Impact of the Intra-axonal space simplifications

In our second study, we look into the effect of using curved or angled geometries against straight cylinders as representations of the intra-axonal space. Such an effect is of particular interest on the computation of axonal diameter indexes when it is assumed that straight cylinders capture the diffusion properties of the intra-axonal compartment.

To understand this effect, an experiment extending the previous work from (Nilsson *et al.*, 2012) was performed, where the diffusion properties of undulating axonal substrates using a helical undulation parametrization along  $z$ .

$$U(z) = \left( A_x \cos\left(\frac{2\pi z}{L}\right), A_y \sin\left(\frac{2\pi z}{L}\right), z \right), \quad 3-3$$

where  $L$  is the wavelength and  $A_x, A_y$  denote the amplitude in the X- and Y- axis, respectively. The amplitudes  $A_x$  and  $A_y$  were set to be equal to obtain helical undulations. A set of substrates was made by deforming cylinders with diameters of  $1 \mu m$ ,  $2 \mu m$ , and  $3 \mu m$  using the formula above. The wavelength and amplitude of the undulations were  $4 \mu m$  to  $2 \mu m$  and  $0.2 \mu m$  to  $2.6 \mu m$ , respectively, covering a wide range of values in the literature (Haninec, 1986; Allison C. Bain David I. Shreiber, 2004; Nilsson *et al.*, 2012). The resulting undulating cylindrical shapes were triangulated to use them as mesh substrates suited for MCDS, as shown in Figure 3-2.

A fitting procedure using an exhaustive search approach was used to calculate the diameter estimation error in the intra-axonal signal. The RMAE between the simulated signal of each undulating substrate and the analytical signal of a range of cylinders with different diameters, sampled between  $0.4 \mu m$ , and  $8.0 \mu m$  with a step size of  $0.01 \mu m$ , is computed using exhaustive search. The GPD approximation for the signal in cylinders was used to calculate the analytical signals (Van Gelderen *et al.*, 1994). The fitting procedure returns a set of plausible diameters with a computed error between them that is less than a threshold set at a 1% difference from the minimum fitting error for each undulating substrate. The fitting procedure was carried out using two different acquisition protocols i) the ex-vivo

ActiveAx PGSE protocol (Alexander *et al.*, 2010) and ii) the optimized PGSE protocol for ex-vivo axonal diameter estimation described in (Dyrby *et al.*, 2013).

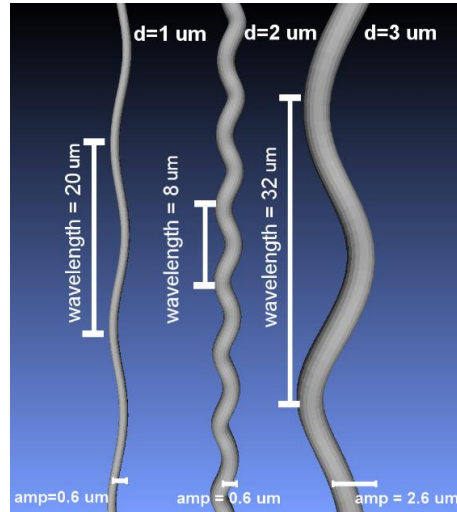


Figure 3-2: Curved meshes used as intra-axonal substrates.

Examples of the curved meshes for three different diameters and different undulation parameters.

Finally, the convergence analysis described at the beginning of the Chapter was used to select the MC simulation parameters. The confidence estimate was calculated by varying the number of particles and time steps on the substrate with higher curvature (higher amplitude and smaller wavelength) and selecting parameters with almost no variance in the estimations. A total of  $5 \times 10^4$  particles and  $5 \times 10^4$  steps were chosen to compute the signal for each substrate separately.

## Extra-axonal space representation

If the volume size of the sample is large enough, extra-axonal spins exhibit an effective diffusivity that an axisymmetric tensor can represent in the case of macroscopically homogeneous substrates, e.g. with randomly packed cylinders and in the absence of bundle dispersion (Hrabe *et al.*, 2004). Several works (Assaf *et al.*, 2008; Alexander *et al.*, 2010; Hui *et al.*, 2011; Panagiotaki *et al.*, 2012; Daducci *et al.*, 2015; Benjamini *et al.*, 2016) assume that the extra-axonal radial contribution does not shift for any direction aligned to

the bundle's perpendicular plane. This assumption seems to be supported by the author's validations. However, in MCDS, the significance of the extra-axonal space design was commonly ignored because it was presumed that substrates with any hindered configuration would match the model. To demonstrate such a pitfall, we conducted a study of the extra-axonal radial contribution in simulated signals, which shows the importance of the sample size in terms of the number of cylinders used to create a substrate.

In our third study, the radial extra-axonal DW-MRI signal was simulated to select voxels with different numbers of cylinders and a fixed distribution of diameters and intra-axonal volume fractions. As in our first analysis,  $N$  diameters ( $N = 100, 1,000, 10,000, 50,000,$  and  $100,000$ ) were sampled from a gamma distribution with parameters  $\Gamma(4.0, 4.5 \times 10^{-7})$ . The corresponding cylinders were randomly placed in substrates with voxel sizes adjusted to ensure a 60% intra-axonal volume fraction and periodicity at the voxel boundaries. The extra-axonal signal was simulated using the following parameters:  $1 \times 10^6$  particles in the extra-axonal space with diffusivity of  $0.6 \times 10^{-4} \text{ mm}^2\text{s}^{-1}$ ,  $\text{TE} = 0.075$  s, and  $1 \times 10^3$  steps. The diffusion protocol was set to highlight the radial contribution of the diffusion signal in different diffusion time regimes as follows:  $G = 300 \text{ mTm}^{-1}$ ,  $\delta = 0.010$  s and  $\Delta$  from 0.015 to 0.060 s., acquired in 180 directions evenly distributed over the XY-plane. The simulated noiseless signal's anisotropy was calculated by dividing the signal's standard deviation by its mean, yielding an approximation of how far the signal deviates from a perfectly radially isotropic signal.

## 3.3 Results

### Convergence analysis

Figure 3-3 summarizes the overall results of the bootstrapping analysis for the intra- and extra- axonal space with respect to the number of samples and time-steps. The graphs represent the mean error of the 50 samples for each possible combinations of the selected parameters, which are colour-coded in a heat map. We showed the error of each repetition

by i) setting the number of steps to the limit ( $2 \times 10^4$ ) and varying the number of particles (left column), and ii) setting the number of particles to the maximum ( $2 \times 10^6$ ) and varying the number of steps (right column). Each data point represents one repeat of a fixed sample size. Each row contains 50 points, and the mean error for each sample is denoted by a red asterisk.

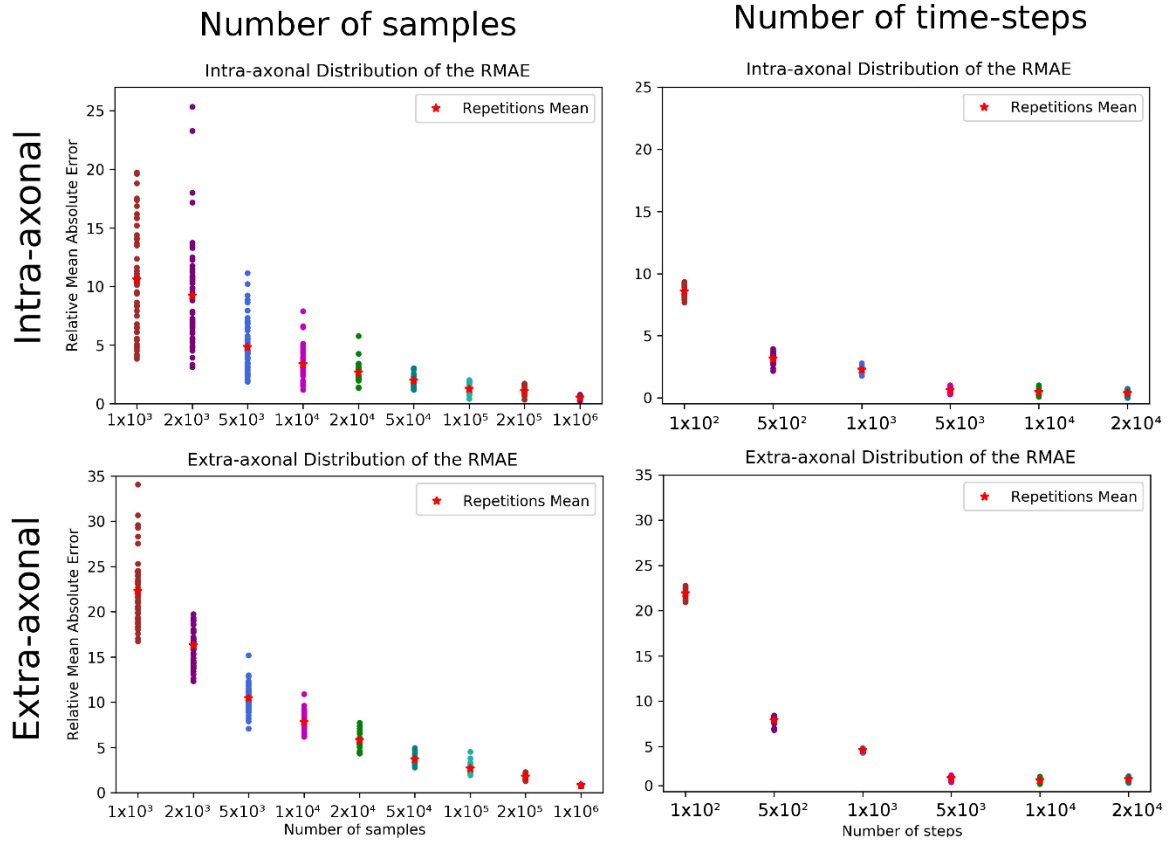


Figure 3-3 RMAE Intra- extra- axonal tests.

RMAE for each repeat and sample size for the number of samples (left) and time-steps (right). The top two rows reflect intra-axonal results, while the bottom row reflects extra-axonal results. The X-axis represents each sample size, and the Y-axis represents the RMAE of all repetitions of the same colour. A red marker represents the mean RMAE of all repetitions.

The error in the estimation presented in Figure 3-3 illustrates the significant possible estimation variability for a relatively simple substrate. We found that the signal on each

compartment showed high variability for simulations with less than  $5 \times 10^5$  particles and  $1 \times 10^4$  steps, which are above the range of parameters used in other simulations studies. We can extrapolate from this that any estimation from more complex substrates, such as the ones with undulation or crossings, or even higher diffusivity, will likely entail even higher variability. Instead of using this measurement as a rule of thumb, to avoid such uncertainty on the estimations for more intricate substrates, a similar analysis as the one presented should be attained.

## Intra-axonal space representation results

The diameter range calculated from our fitting procedure for both protocols is shown in Figure 3-4. Each cell is coloured according to its minimum RMAE. In the table's rows, an amplitude (amp) of  $0 \mu m$  corresponds to a straight cylinder, which has the minimum fitting error achievable for each diameter. Values with the highest amplitude and lowest wavelength (wl) correspond to the axons with the highest undulation,  $wl = 4 \mu m$ ; on the other hand, values with the lowest amplitude and highest wavelength amplitude (amp =  $0.2 \mu m$ ,  $wl = 32 \mu m$ ) corresponds to almost straight axons.

While the helical representation used in this study was found to exist in the nervous system (Nilsson *et al.*, 2012), it may not accurately represent the longitudinal axonal angular variations in the brain's white matter, particularly at the micro-scale. However, it gives us a convenient starting point to study the effect of angular variations in the intra-axonal compartment over the diffusion signal. This study found a considerable misestimation in the presence of undulation for both protocols and the three studied diameters. The relative fitting error for the smaller diameter ( $1 \mu m$ ) was higher among the three cases (more than 300 % for some cases). We also observed that the range of diameters from our fitting method did not follow a simple trend between protocols; that is to say, increments on the undulation parameters, which effect can be summarized in terms of the tortuosity factor  $\lambda = \sqrt{(2\pi A/L)^2 + 1}$ , does not follow a simple relationship between protocols (horizontal

axis of the results in Figure 3-4). This is likely to affect the parameters of the acquisition protocol ( $\delta$ ,  $\Delta$  and TE), which vary between shells and thus change the effective diffusion time. We corroborated that the optimized protocol showed better results in terms of the fitted diameter and range of similar diameters compared to both protocols. However, there was still a considerable misestimation, especially for the undulation of 1  $\mu\text{m}$  diameter. We considered this experiment to be of great interest for any future protocol optimization or diameter estimation framework. It illustrates how sensible the estimation of the axon's diameter based on the cylindrical model is, even for regular and smooth angular deviations.

Diameter = 1 $\mu\text{m}$						RMAE
amp / wl	4 $\mu\text{m}$	8 $\mu\text{m}$	12 $\mu\text{m}$	20 $\mu\text{m}$	32 $\mu\text{m}$	
0 $\mu\text{m}$	[0.4, 2.5]	[0.4, 2.5]	[0.4, 2.5]	[0.4, 2.5]	[0.4, 2.5]	0.00%
0.2 $\mu\text{m}$	[0.4, 1.6]	[0.4, 1.7]	[0.4, 1.9]	[0.4, 2.2]	[0.4, 2.0]	1.42%
0.4 $\mu\text{m}$	[0.4, 1.7]	[0.4, 1.9]	[0.4, 2.2]	[0.4, 2.3]	[0.4, 2.2]	2.84%
0.6 $\mu\text{m}$	[0.4, 1.8]	[0.4, 2.0]	[0.4, 2.4]	[0.4, 2.6]	[0.4, 2.4]	4.26%
1.0 $\mu\text{m}$	[0.4, 2.1]	[0.4, 2.5]	[0.4, 3.0]	[0.4, 3.3]	[0.4, 3.0]	5.68%
1.6 $\mu\text{m}$	[0.4, 3.8]	[0.4, 4.4]	[3.2, 4.5]	[3.2, 4.3]	[2.4, 3.8]	7.10%
2.6 $\mu\text{m}$	[6.6, 7.0]	[6.5, 6.9]	[6.2, 6.6]	[5.3, 5.9]	[4.3, 4.9]	8.52%
Diameter = 2 $\mu\text{m}$						9.94%
amp / wl	4 $\mu\text{m}$	8 $\mu\text{m}$	12 $\mu\text{m}$	20 $\mu\text{m}$	32 $\mu\text{m}$	11.36%
0 $\mu\text{m}$	[1.1, 2.2]	[1.1, 2.2]	[1.1, 2.2]	[1.1, 2.2]	[1.1, 2.2]	12.78%
0.2 $\mu\text{m}$	[0.4, 1.9]	[0.4, 2.1]	[0.4, 2.3]	[1.6, 2.5]	[0.4, 2.3]	14.20%
0.4 $\mu\text{m}$	[0.4, 1.8]	[0.4, 2.1]	[0.4, 2.5]	[0.4, 2.5]	[0.4, 2.6]	15.62%
0.6 $\mu\text{m}$	[0.4, 1.9]	[0.4, 2.2]	[0.4, 2.7]	[0.4, 2.9]	[1.7, 2.9]	17.04%
1.0 $\mu\text{m}$	[0.4, 2.2]	[0.4, 2.8]	[0.4, 3.3]	[1.7, 3.4]	[1.9, 3.3]	18.46%
1.6 $\mu\text{m}$	[0.4, 4.2]	[2.6, 4.7]	[3.6, 4.7]	[3.5, 4.4]	[2.7, 3.9]	19.88%
2.6 $\mu\text{m}$	[6.9, 7.3]	[6.7, 7.1]	[6.4, 6.8]	[5.4, 6.0]	[4.4, 5.0]	21.30%
Diameter = 3 $\mu\text{m}$						22.72%
amp / wl	4 $\mu\text{m}$	8 $\mu\text{m}$	12 $\mu\text{m}$	20 $\mu\text{m}$	32 $\mu\text{m}$	24.14%
0 $\mu\text{m}$	[2.9, 3.1]	[2.9, 3.1]	[2.9, 3.1]	[2.9, 3.1]	[2.9, 3.1]	25.56%
0.2 $\mu\text{m}$	[0.4, 2.9]	[1.8, 3.0]	[2.9, 3.1]	[2.6, 3.1]	[3.0, 3.2]	26.98%
0.4 $\mu\text{m}$	[0.4, 2.4]	[0.4, 3.0]	[2.0, 3.2]	[2.7, 3.2]	[2.5, 3.1]	28.40%
0.6 $\mu\text{m}$	[0.4, 2.4]	[0.4, 3.0]	[1.3, 3.4]	[2.5, 3.4]	[2.9, 3.4]	29.82%
1.0 $\mu\text{m}$	[0.4, 2.9]	[0.4, 3.6]	[2.6, 3.9]	[3.1, 3.9]	[2.7, 3.6]	31.24%
1.6 $\mu\text{m}$	[3.9, 4.9]	[3.9, 5.2]	[4.2, 5.1]	[3.9, 4.7]	[3.3, 4.2]	32.66%
2.6 $\mu\text{m}$	[7.3, 7.7]	[7.1, 7.5]	[6.7, 7.1]	[5.7, 6.2]	[4.7, 5.2]	34.08%

Diameter = 1 $\mu\text{m}$						RMAE
amp / wl	4 $\mu\text{m}$	8 $\mu\text{m}$	12 $\mu\text{m}$	20 $\mu\text{m}$	32 $\mu\text{m}$	
0 $\mu\text{m}$	[0.4, 1.4]	[0.4, 1.4]	[0.4, 1.4]	[0.4, 1.4]	[0.4, 1.4]	0.00%
0.2 $\mu\text{m}$	[0.4, 1.3]	[0.4, 1.5]	[0.4, 1.6]	[0.4, 1.5]	[0.4, 1.7]	1.42%
0.4 $\mu\text{m}$	[0.4, 1.3]	[0.4, 1.7]	[0.4, 2.0]	[0.4, 1.9]	[0.4, 1.8]	2.84%
0.6 $\mu\text{m}$	[0.4, 1.5]	[0.4, 1.9]	[0.4, 2.2]	[0.4, 2.2]	[0.4, 2.1]	4.26%
1.0 $\mu\text{m}$	[0.4, 2.3]	[0.4, 2.6]	[1.6, 3.0]	[0.4, 2.7]	[0.4, 2.5]	5.68%
1.6 $\mu\text{m}$	[3.8, 4.6]	[3.9, 4.5]	[3.8, 4.3]	[3.2, 3.7]	[2.0, 3.1]	7.10%
2.6 $\mu\text{m}$	[6.3, 6.6]	[6.0, 6.3]	[5.6, 5.9]	[4.7, 5.0]	[3.6, 4.1]	8.52%
Diameter = 2 $\mu\text{m}$						9.94%
amp / wl	4 $\mu\text{m}$	8 $\mu\text{m}$	12 $\mu\text{m}$	20 $\mu\text{m}$	32 $\mu\text{m}$	11.36%
0 $\mu\text{m}$	[1.9, 2.1]	[1.9, 2.1]	[1.9, 2.1]	[1.9, 2.1]	[1.9, 2.1]	12.78%
0.2 $\mu\text{m}$	[0.4, 1.8]	[1.4, 2.1]	[1.0, 2.1]	[1.3, 2.1]	[0.4, 2.1]	14.20%
0.4 $\mu\text{m}$	[0.4, 1.6]	[0.4, 2.0]	[0.4, 2.4]	[1.7, 2.4]	[1.5, 2.3]	15.62%
0.6 $\mu\text{m}$	[0.4, 1.8]	[0.4, 2.2]	[0.4, 2.6]	[0.4, 2.5]	[1.9, 2.5]	17.04%
1.0 $\mu\text{m}$	[0.4, 2.8]	[1.8, 3.1]	[2.4, 3.3]	[2.2, 3.0]	[1.4, 2.7]	18.46%
1.6 $\mu\text{m}$	[4.2, 4.9]	[4.2, 4.8]	[4.0, 4.5]	[3.3, 3.8]	[2.4, 3.2]	19.88%
2.6 $\mu\text{m}$	[6.6, 6.9]	[6.2, 6.5]	[5.8, 6.1]	[4.8, 5.2]	[3.8, 4.2]	21.30%
Diameter = 3 $\mu\text{m}$						22.72%
amp / wl	4 $\mu\text{m}$	8 $\mu\text{m}$	12 $\mu\text{m}$	20 $\mu\text{m}$	32 $\mu\text{m}$	24.14%
0 $\mu\text{m}$	[2.9, 3.0]	[2.9, 3.0]	[2.9, 3.0]	[2.9, 3.0]	[2.9, 3.0]	25.56%
0.2 $\mu\text{m}$	[2.5, 2.9]	[2.8, 3.0]	[2.9, 3.0]	[3.0, 3.0]	[3.0, 3.0]	26.98%
0.4 $\mu\text{m}$	[0.4, 2.8]	[2.7, 3.1]	[2.9, 3.2]	[2.7, 3.1]	[3.0, 3.1]	28.40%
0.6 $\mu\text{m}$	[0.4, 2.8]	[2.6, 3.3]	[2.9, 3.3]	[2.9, 3.2]	[2.9, 3.1]	29.82%
1.0 $\mu\text{m}$	[2.6, 3.9]	[3.4, 3.9]	[3.4, 3.8]	[3.1, 3.5]	[2.9, 3.3]	31.24%
1.6 $\mu\text{m}$	[4.9, 5.5]	[4.8, 5.3]	[4.5, 4.9]	[3.8, 4.2]	[3.2, 3.7]	32.66%
2.6 $\mu\text{m}$	[7.1, 7.4]	[6.7, 7.0]	[6.2, 6.4]	[5.1, 5.5]	[4.2, 4.6]	34.08%

Figure 3-4 Tables with the diameter fitting results.

For the three simulated diameters, the left column displays the fitted intervals of the initial ex-vivo ActiveAx protocol (Alexander *et al.*, 2010), and the right column shows the optimized ex-vivo protocol from (Dyrby *et al.*, 2013). For each simulated amplitude and wavelength, the min and max diameters (m) of the fitted range are specified between square brackets. According to the colour bar on the right, the colour of each cell is encoded with respect to the minimum RMAE in the fitted set.

In a previous work (Nilsson *et al.*, 2017), it is worth mentioning that a formulation to compute the minimal diameter of a parallel cylinder can produce a signal attenuation more significant than that from a cylinder with a diameter of zero using standard single-shell



PGSE sequences. According to this formalism, the minimum differentiable diameter is  $d_{min} = (768\sigma D/7\gamma^2\delta|G|^2)^{1/4}$ , where  $\sigma$  is the significance level, defined as the minimum tolerated percentage of signal change. For a fixed value  $\sigma = 1\%$  change, the resolution limit predicted for both protocols used in this study were  $d_{min} = 2.29\mu m$  for  $|G| = 140mT/m$ , and  $d_{min} = 1.76\mu m$  for  $|G| = 300mT/m$ . However, such estimates are based on many assumptions that do not hold in our experimental conditions. For example, the formulation is valid for parallel and straight cylinders and acquisition protocols with a single shell with parameters  $\delta = \Delta$ , which is not the case of this experiment, where we used non-parallel and curved cylinders with multi-shell protocols with  $\Delta \gg \delta$ .

## Extra-axonal space representation results

Figure 3-5 shows three distinct substrates with 100, 1,000, and 10,000 cylinders, corresponding to voxel sizes of  $23 \times 23\mu m$ ,  $71 \times 72\mu m$ , and  $230 \times 230\mu m$ , respectively, and their corresponding radial DW-MRI signals. The voxel sizes shown were chosen to emphasize the radial anisotropy in three representative sizes. The most isotropic radial DW-MRI signal was found on the substrate with 10,000 cylinders, i.e. the most significant voxel scale. The substrate with the fewest cylinders, on the other hand, produced the most anisotropic signal. The mean and standard deviation of the radial extra-axonal signal as a function of voxel size is shown in Figure 3-5. The graphs showed that a sufficiently rich sampling is required for the simulated signal to converge. Indeed, small substrates have a limited number of cylinders, limiting the variability of hindered micro-environments sampled by the spins during the Monte-Carlo simulation — yielding anisotropic patterns in the radial DW-MRI signal. The results also showed a bias in the mean amplitude, with small voxels having a lower signal than bigger voxels. Our results suggest that, for a given diameter distribution, substrates with an area smaller than  $200 \times 200\mu m$  will present biased extra-axonal signals. However, this lower bound probably depends on the distribution of diameters and cylinder packing on one side and the typical diffusion length of the spins, given by their diffusivity and the diffusion time of the experiment.

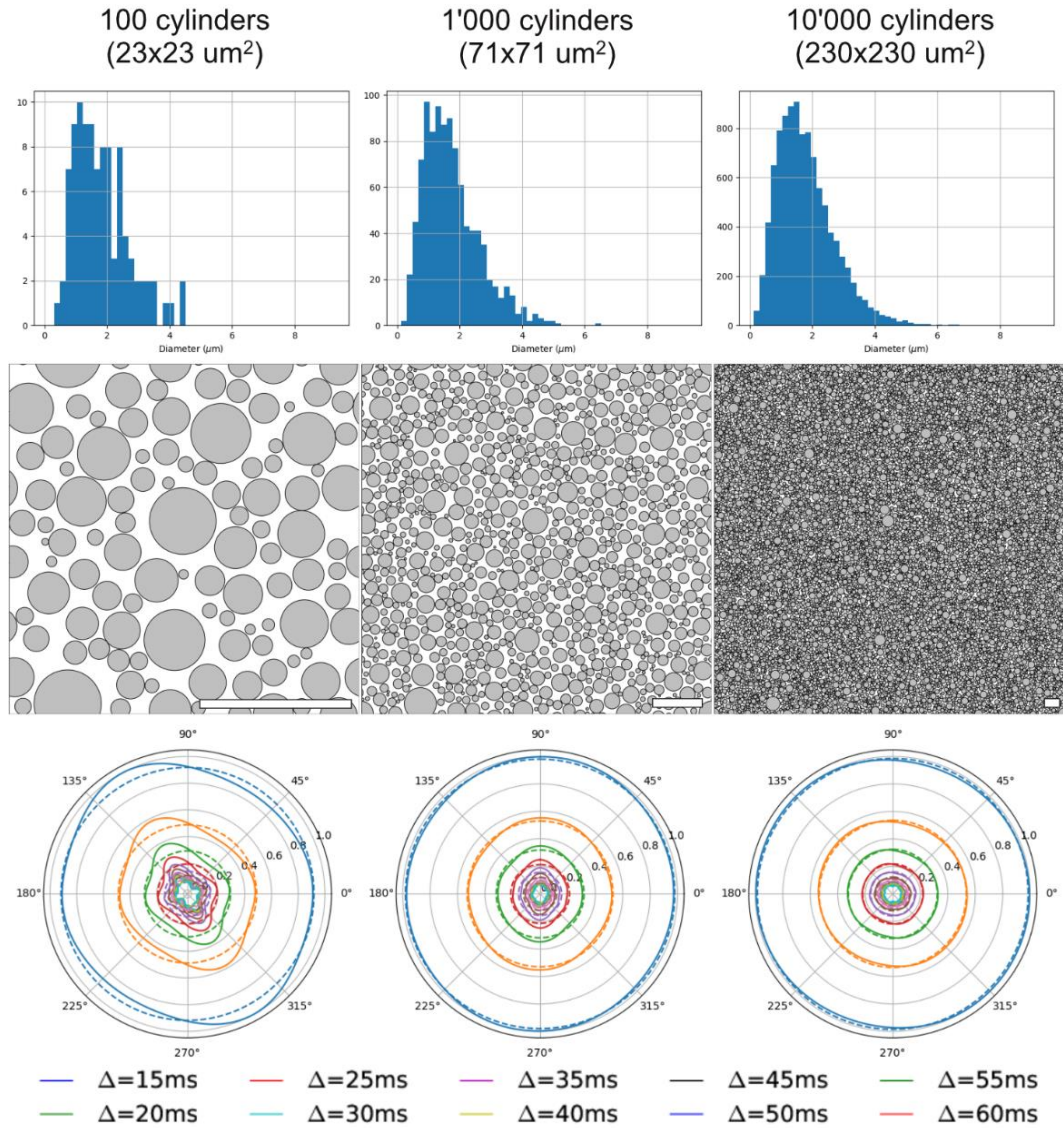


Figure 3-5 Results for three substrates, with 100, 1,000 and 10,000 cylinders, respectively.

First row: sample diameter distributions for each voxel size, getting closer to the desired distribution law as the voxel size increases. Second row: Cylinder's packing positions in each substrate, the white scale bar corresponds to 10 $\mu\text{m}$ . Third row: radial DW-MRI signal simulated from the respective substrates. Each coloured line corresponds to one different  $\Delta$  duration. Dotted lines correspond to the mean radial signal for each diffusion time.

### 3.4 The MC/DC Simulator

The Monte Carlo Diffusion and Collision (MC/DC) Simulator is a C++, open-source, DW-MRI Monte-Carlo Simulator developed as part of the contribution work done in (Rafael-Patino, Romascano, *et al.*, 2020). The simulator is currently supported and still under constant development. The installation, main parameters and examples can also be found in the simulator's repository <sup>1</sup>.

The simulator is implemented following a modular and scalable architecture, as shown in Figure 3-6. Similar to our description of the simulation process in Chapter 3, the framework separates a Monte-Carlo simulation into the two core tasks, the particle dynamics inside the *DynamicSimulation* class and the signal synthesis, handled by the *SimuleableSequence* base class. Both classes are fundamentally independent of each other, making the simulation process's separation (and parallelization) possible. We used this property to implement a fast signal synthesizer for the DW-MRI protocol optimization framework, explained in Chapter 6. The simulator also implements a friendly user interface via simple scripting to run and handle the most common simulation types. The simulator handles three types of obstacles for the spin dynamics: infinity cylinders of constant radii, spheres of constant radii, and closed 3d mesh models. Several obstacles can be defined inside a single substrate in arbitrary positions by the user. The simulator also implements some commonly used substrates for porous media such as hexagonally packed cylinders, hexagonally packed spheres, randomly packed cylinders with radii sampled from a Gamma distribution ( $r \sim \Gamma(\alpha, \beta)$ ), and randomly packed spheres with radii sampled from a Gaussian distribution ( $r \sim G(\mu, \sigma)$ ). On the other hand, for the signal synthesis, the simulator handles two nominal cases: explicit PGSE protocols parametrized by the gradient strength and its timings  $\delta$ ,  $\Delta$ , and  $TE$  (see Chapter 2); and General Waveforms parametrized as 3d gradient curves over time. For more details on the needed parameters and other advanced options to track dynamic and magnetic simulation events, such as the particles' mean squared

---

<sup>1</sup> [https://github.com/jonhraf/MCDC\\_Simulator\\_public](https://github.com/jonhraf/MCDC_Simulator_public)

displacement distribution, phase shift distribution, or ensemble propagator over time, we refer the reader to the technical project's GitHub page.

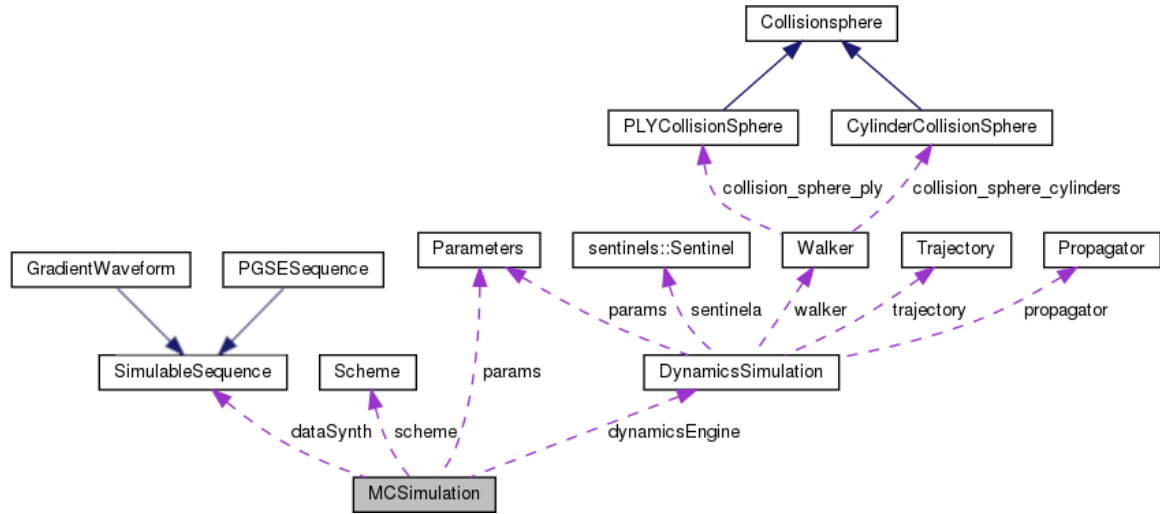


Figure 3-6 Single MC/DC simulation core components.

The purple dotted arrows indicate which classes (pointed classes) are instances in the base class. Blue lines indicate inherited classes from the parent (pointed) class. All the displayed components depicted above are organized in separated class-oriented modules with abstract-based prototypes that can be inherited and re-implemented to augment the functionality and scope of the simulations.

### 3.5 Discussion and Conclusions

To summarize, this Chapter's key inputs can be defined as follows: First, we discuss and explore a series of pitfalls that can occur when selecting parameters and designing substrates for Monte-Carlo simulations. Our findings on the effect of particle number and time-steps and our quantification of the effect of substrate size on extra-axonal space can be used to improve the design of future experiments immediately. Overall, we discovered that simulations of less than  $5 \times 10^5$  particles and  $1 \times 10^4$  steps carried a significant variance between the computed signals for both the intra- and extra-axonal compartments. Furthermore, we discovered that simulation substrates with less than 10,000 sampled

cylinders caused a significant bias in the diffusion signal's directional symmetry in directions transversal to the main fibre path. Those values are around one order of magnitude larger than those used in the literature, which necessarily impacts reproducibility. An additional effect of incorporating angular perturbations into the intra-axonal space model showed significant deviations from expectations (Hall and Alexander, 2009; Rensonnet *et al.*, 2018, 2019). Using the approximate axon diameter based on the cylindrical model, we evaluated the effect of incorporating such angular perturbations in the intra-axonal space representation and found a significant deviation from the predicted results. This finding is consistent with previous findings and adds to the growing body of evidence that estimating whole-brain axon diameter using simplified models like the straight cylindrical diffusion model may not be feasible. Finally, we presented a self-implemented robust and open-source simulator that paved the way for all the presented studies in the following chapters of this thesis.

# Chapter 4

## Towards Realistic and Complex Numerical Phantoms

---

### 4.1 Overview

The introduction of new simulation frameworks, such as the one described above, has pushed the community to consider more complex in-silico approaches rather than analytical models. However, due to the inherent complexity of the brain's white matter at the micro and meso scales, defining and designing appropriate physical models (with accurate microstructural features) has proven to be a difficult task. In this chapter, we describe our efforts to create more realistic white matter numerical phantoms. The first section describes a proposed framework based on a previous algorithm used to build tractography phantoms. The adaptation to this framework for MCDS results in a system capable of generating complex fibre configurations at the mesoscale and with desired microstructure details presented in (Rafael-Patino, Romascano, *et al.*, 2020). We demonstrated the framework's ability to generate a complex fibre configuration, which is used to highlight the frameworks' capabilities and the resulting microstructure maps. Then, we present arguably the most complex numerical phantom build to this day, the DiSCo Numerical phantom, which is introduced as a new phantom for joint microstructure and tractography studies. Finally, we describe additional experiments on the simulation of realistic axons segmented from electron microscopy, which has previously been used successfully in other collaboration studies (Andersson *et al.*, 2021).

## 4.2 Complex substrates generation framework

Based on the results of previous experiments and a previously published algorithm for generating tractography phantoms (Close *et al.*, 2009), the section that follows lays out a general structure for creating complex substrates. We illustrate that such a structure overcomes some of the previous sections' simplifications. A cross-section of axon bundles was created as a study case to demonstrate those capabilities. The complexity of the crossing fibres was evaluated qualitatively in terms of the resulting intra-axonal volume fraction and diffusion properties at various resolutions.

The original framework is based on optimising an objective function that penalizes the overlap, curvature and length of a set of initial splines called strands. Each strand has a constant radius used to ensure no overlapping. The optimization cost-function has the following form:

$$E(\cup S) = \sum_i^{\#S} w_o J_o(S_i) + w_c J_c(S_i) + w_l J_l(S_i), \quad 4-1$$

where the set  $\cup S$  of size  $\#S$ , denotes the collection of all initialized strands and  $S_i$  represents the strand  $i$  for  $i = 1, \dots, S$ . The functions define the overlap, curvature, and length penalization functions  $J_o(\cdot), J_c(\cdot), J_l(\cdot)$ ; and the coefficients represent their weights  $w_o, w_c$ , and  $w_l$ . Each strand  $S_i$  is parametrized using a distinct set of control points that describe the strand's backbone and a constant radius; the transversal region associated with this radius is then subdivided to form sub-strands. For more details, we refer the reader to (Close *et al.*, 2009).

A gamma-distributed collection of diameters was mapped within the trajectories of the resulting strands using the structure mentioned above, which was improved. The cost-function,  $J_o$ , was also adjusted to make it more appropriate for constructing 3D meshes. The analytical intersection between two strands' control points was computed using the cylinder to cylinder collision detection described in (Verth and Bishop, 2008).



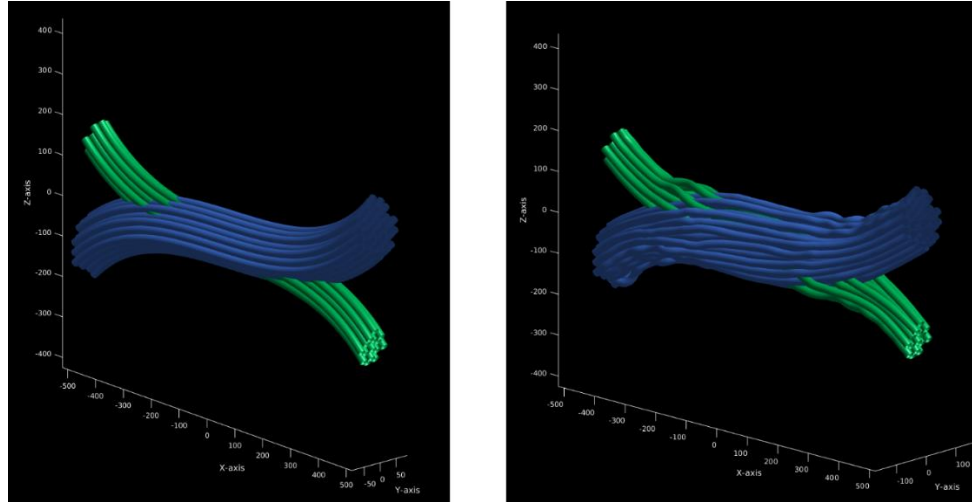


Figure 4-1 Optimized non-overlapped trajectories

Optimization procedure of initial trajectories. (Left) initial trajectories parametrized as a set of control points with a constant radius. (Right) the resulting trajectories after the optimization procedure, which ensures that there is no overlapping between the resulting strands.

The outcome is a gamma-distributed crossing arrangement of deformed cylinders. The key benefit of this configuration is that the bundles within a common area do not overlap or intersect but rather interdigitate, preserving volume in the crossing field. Furthermore, the curvature and length penalties encourage a higher packing density. Finally, rather than assigning a symmetric tensor along the sub-strands, the proposed structure computes the DW-MRI signal using a Monte-Carlo simulation using a mesh substrate built from the configuration obtained above. Figure 4-2 shows the crossing configuration before and after the optimization procedure.

The diameters from a gamma distribution with parameters  $\Gamma(1.2, 1.5 \times 10^{-6}) \mu\text{m}$  were sampled in the presented study case, resulting in mean diameter of  $\mu = 1.8 \mu\text{m}$  and standard deviation  $\sigma = 1.6 \mu\text{m}$ , which are in the range of anatomical interest (Alexander *et al.*, 2010). To prevent strands with diameters smaller than  $0.2 \mu\text{m}$ , the resulting values were truncated. The dimensions of the resulting enclosing volume were  $1200 \mu\text{m} \times 240 \mu\text{m} \times 480 \mu\text{m}$ . Figure 4-1 depicts the resulting 3D geometrical crossing. After post-processing decimation and smoothing to reduce the triangle density, the 3D mesh model has 1,698,328 triangular faces. The longest strand measures  $1.58 \text{ mm}$  from end to end. The



resulting diameter distribution of the overall structure is shown in Figure 4-2's bottom panel.

The total volume was divided into three voxel resolutions to compute the simulated MRI signal:  $80 \times 16 \times 32$ ,  $40 \times 8 \times 16$ , and  $20 \times 4 \times 8$  voxels. The signal for the three resolutions was computed using  $105 \times 10^6$  particles and 5,000 steps. The original ActiveAx protocol from (Alexander *et al.*, 2010) was used with a diffusivity coefficient equal to  $0.6 \times 10^{-3} \text{ mm}^2/\text{s}$  and a total diffusion time of 0.053 s.

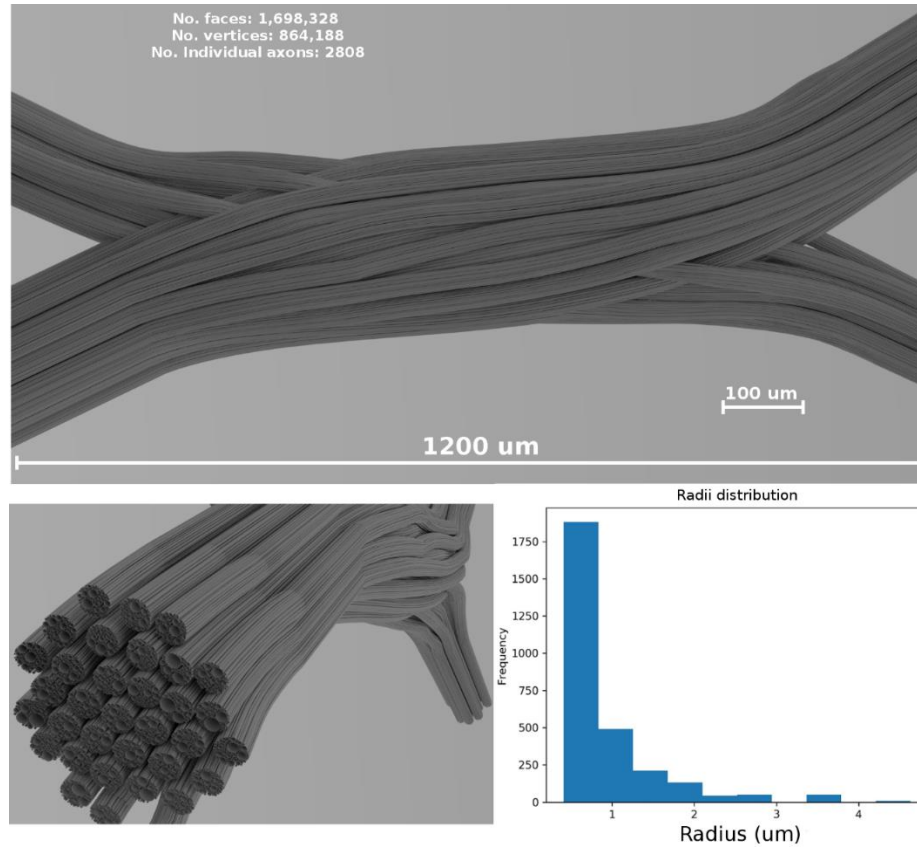


Figure 4-2 Fiber crossing substrate.

The top panel shows a visualization of the resulting fibre crossing substrate after the strand refinement and the smoothing and decimation of the triangular faces. The left-bottom panels show the resulting sub-strand configuration of one of the crossings bundles. The Right-bottom panel shows the overall diameter distribution of the displayed bundle on the (left).

The Diffusion Tensor estimate and corresponding FA were computed using Dipy (Garyfallidis *et al.*, 2014) and the ICVF maps for each of the three resolutions. To compute the DT in each voxel, only the shell with  $b=3080 \text{ s/mm}^2$  was used. Since there was no analytic representation of the substrate, the ICVF was approximated by tracking the local location of the uniformly random positioned particles and labelling them as within or outside the meshed substrate.

Finally, for the three separate voxel resolutions, an assessment of the axon diameter estimate within the crossing region was performed. The same exhaustive search method explained before was used to estimate axon diameter. The analytical GPD approximation was computed using only one bundle orientation chosen from the DT calculation at each voxel. The fitting procedure was performed solely on the intra-axonal signal and in voxels with FA greater than 0.25 to isolate the effect of extra-axonal space on diameter misestimation.

## Results on a fibre-crossing substrate

The resulting crossing with two fibre populations is outlined in Figure 4-2. The total optimization time to construct the substrate was approximately 42 hours, with the majority of the optimization time (approximately 35 hours) required in the second optimization iteration, following the subdivision on gamma-distributed radii, to ensure that no minor overlaps and abrupt angular changes were made. A single-core 2.8 GHz processor was used for optimization. The total simulation time for the complete geometry, with  $105 \times 10^6$  particles, was less than 24 hours using a total of 8 nodes with 28 cores on EPFL's cluster and 6GB of RAM per node (48GB in total).

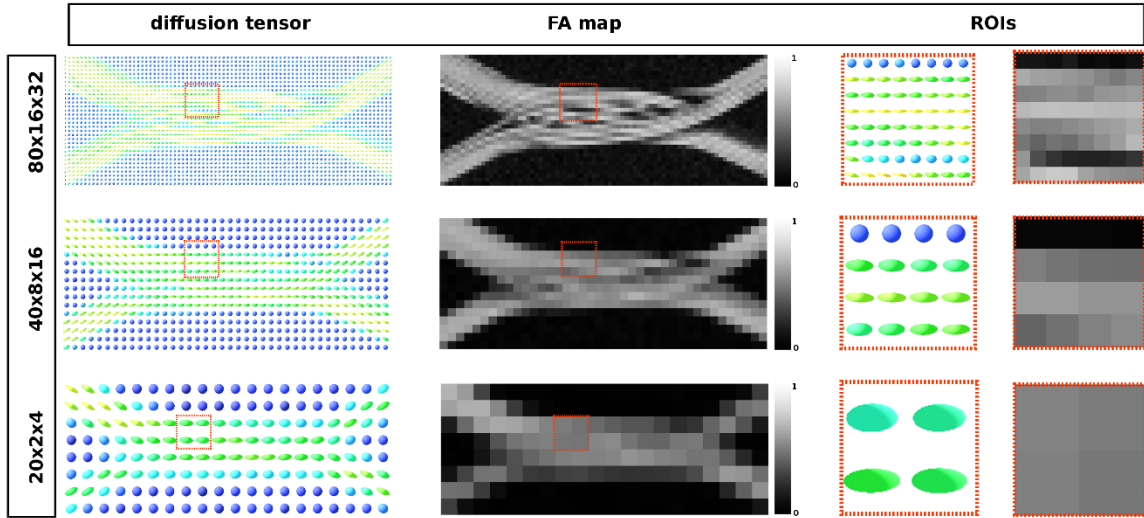


Figure 4-3 Model bases results of the crossing signal.

From the leftmost to the right: diffusion tensor map, the resulting fractional anisotropy, and the two highlighted ROIs in each map. Each image corresponds to the same volume slice in the XZ-plane. The ROI's highlights one area where different compartments result from the optimization procedure.

Figure 4-3 depicts the resulting diffusion tensor and FA maps for the three different resolutions. There can be observed local variations in diffusivity and signal changes linked to the curvature of each axon. Figure 4-4 shows the intra-axonal volume fraction. Small water compartments in the crossing sections can be seen in the highest resolution, and this is a consequence of the optimizer phase that does not overlap fibres. These compartments are no longer visible in the lowest resolution, but the reduced volume fractions indicate these compartments.

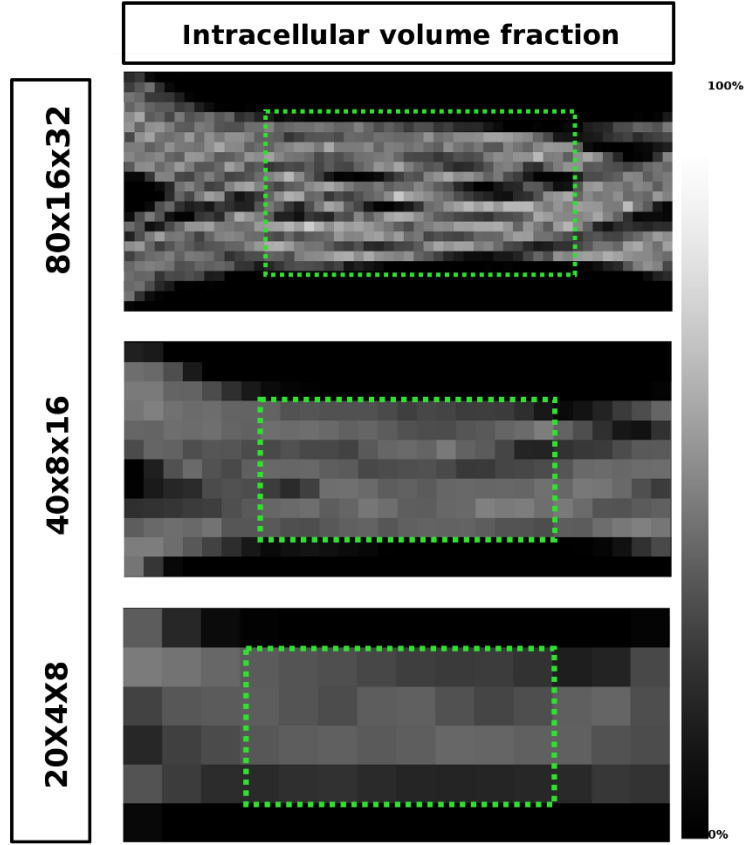


Figure 4-4 ICVF maps of one volume slice in the XZ-plane in three different resolutions.

The highest achieved ICVF value for each resolution were: 0.8013, 0.5792, 0.4825, from top to bottom, respectively. The three green areas highlighted in the two lowest resolutions were used to evaluate the axon diameter estimation.

Figure 4-5 depicts one plane of the axon diameter measurement maps of the volumetric area outlined in Figure 4-4 and the diameter distribution obtained for the three resolutions. The higher resolution estimation (80 x 16 x 32) has 2848 voxels, while the lower resolution has a total of 112 voxels. The bottom-right panel of Figure 7 displays the resulting sampled diameters inside the crossing configuration, which are notably distorted to smaller diameters; this is a consequence of the packing algorithm inside individual circular strands, which under-represent the tail of the distribution due to the complexity of packing strands with large diameters. This influence would have an immediate impact on the effective apparent radius (Burcaw, Fieremans and Novikov, 2015)  $r_{eff} \approx \left( \frac{\langle r^6 \rangle}{\langle r^2 \rangle} \right)^{1/4}$  given by the

intra-axonal contribution of the signal. The resulting effective diameter of the conjoint assemble of strands was  $2 * r_{eff} = 3.48 \mu m$ , comparable with such of Figure 4-5.

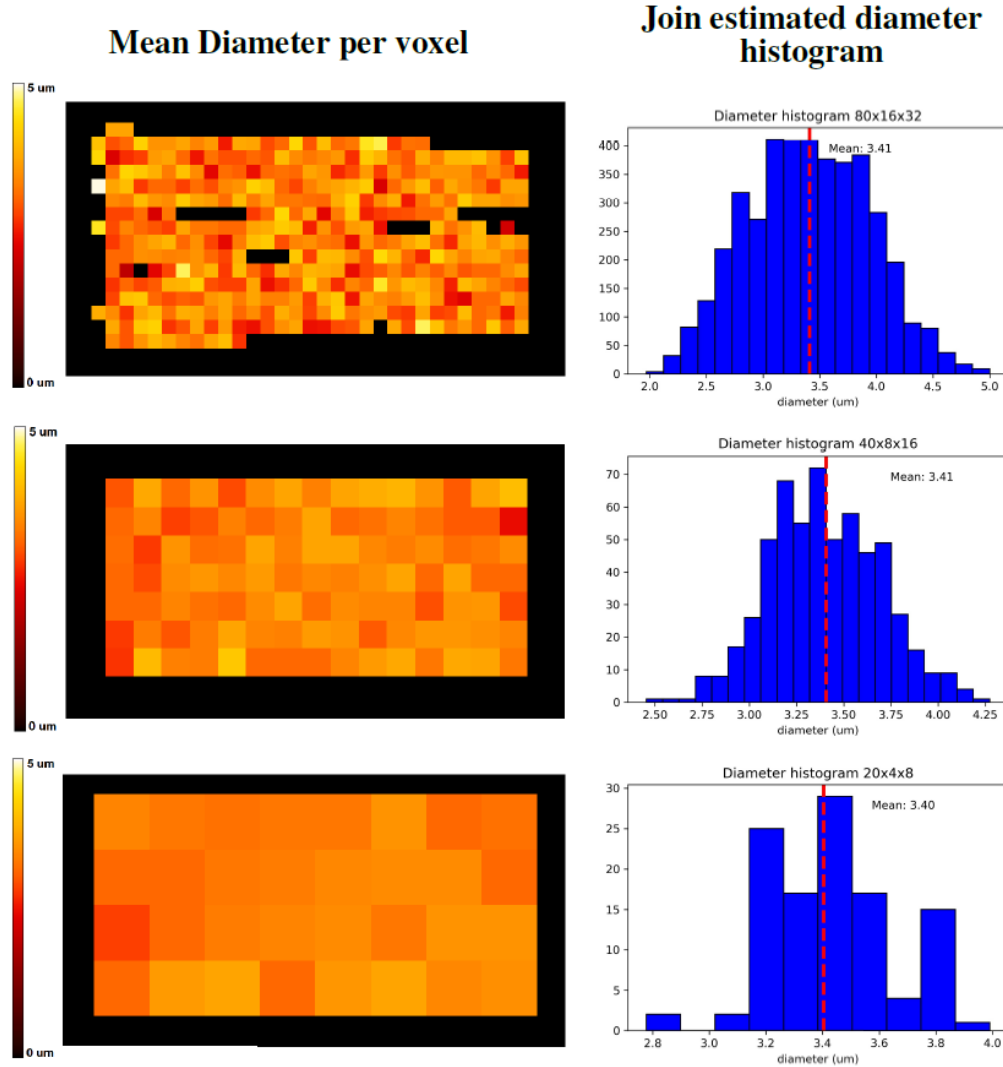


Figure 4-5 Axon diameter estimation maps and distributions.

The left column shows the axon diameter estimation map of the regions highlighted in Figure 4-4. The right column shows the diameter histograms estimated on the total volume enclosed by the highlighted regions. The top row shows the axon diameter map and the diameter estimation histogram for the  $80 \times 16 \times 32$  nominal resolution; the middle row shows the same maps for the  $40 \times 8 \times 16$  nominal resolution, and the bottom row shows the same maps for the  $20 \times 4 \times 8$  nominal resolution. The dotted line indicates the histograms' mean diameter within the regions, to be compared with the effective apparent diameter ( $2 * r_{eff}$ ) of  $3.48 \mu m$ .

## Conclusions

This section presents a framework that can generate complex fibre configurations with desired microstructure information based on a previous algorithm used to create tractography phantoms. We showed the framework's capabilities to generate complex fibres configurations that, along with the simulator developed in this work, can generate more challenging and composite Monte-Carlo simulations. This is further shown in the following section, where a numerical phantom, extensive enough to run tractography algorithms, is constructed. The framework, however, still lacks several structural features present in white matter tissue — such as the axonal myelin sheath, Ranvier nodes, or diameter changes along the trajectory of the axons — and thus, future work should focus on adding such characteristics as explained in the last section of the chapter.

### 4.3 The DiSCo Numerical Phantom for Connectomics

This section describes the creation of a numerical phantom that mimics complex anatomical fibre pathway trajectories while also accounting for microstructural features such as axonal diameter distribution, myelin presence, and variable packing densities. The substrate has a micrometric resolution and an unprecedented size of 1 cubic millimetre to mimic an image acquisition matrix of 40x40x40 voxels. DW-MRI images were obtained from Monte Carlo simulations of spin dynamics to enable the validation of quantitative tractography. The phantom comprises 12,196 synthetic tubular fibres with diameters ranging from  $1.4\ \mu m$  to  $4.2\ \mu m$ , interconnecting sixteen regions of interest. The simulated images capture the macroscopic properties of the tissue (e.g. fibre diameter, water diffusing within and around fibres, free water compartment) while also having desirable macroscopic properties resembling the anatomy smoothness of the fibre trajectories. While previous phantoms were used to validate either tractography or microstructure, this phantom can better assess the connectome estimation's reliability on the one side and its adherence to the actual microstructure of the nervous tissue on the other. This phantom has increased

complexity compared to previously available datasets and may help improve the reconstruction methods of the quantitative structural connectome. In particular, in this large and complex substrate, the volume of the axon-like structure is preserved across their trajectories, allowing for microstructure-informed tractography methods.

## Phantom Design

The DiSCo (Diffusion-Simulated Connectivity) phantom is composed of 12,196 tubular fibres (strands), with gamma-distributed inner diameters ranging from  $1.4 \mu\text{m}$  to  $4.2 \mu\text{m}$ , connecting 16 distant Regions of Interest (ROIs). The strands form different white matter configurations (e.g., kissing, branching), intersect at different crossing angles, split and group after leaving and ending in the ROIs. These fibres form various white matter configurations (e.g. kissing, branching), intersect at various crossing angles, separate and group together after leaving and ending from/in 16 regions, with the possibility of forming 120 distinct pairs of connections. The initial connectivity matrix weights of the DiSCo phantom were randomly generated for 16 ROIs. By controlling for the sparsity of the resulting matrix, we obtained 25 non-zero weights for a total of 120 possible connections among the ROIs. These weights were used to initiate a proportional set of strands of  $15 \mu\text{m}$  in diameter interconnected the ROIs going toward the centre of the sphere (789 strands, see Figure 4-6 b). The strands trajectories were then optimised using the Numerical Fiber Generator (Close *et al.*, 2009) described in the past section. To force strands convergence toward the centre of the phantom, we added spherical constraints around each ROI (see Figure 4-6 a). The cost function had energy terms controlling for strands curvature and strands length. Moreover, the cost function increases when strands overlap with other strands or with spherical constraints. Multiple optimisation iterations were performed to increase the cost of overlapping strands slowly (see Figure 4-6 c,d). Each strand was then subdivided into strands of  $7.5 \mu\text{m}$  in diameter following hexagonal packing (5,523 strands, see Figure 4-6 e). Strands were then optimized to reduce overlaps, length, and curvature. Finally, each strand was subdivided into cylinders which diameters following a gamma



distribution  $\Gamma(\kappa, \theta)$ , with shape,  $\kappa = 0.5$ , and scale  $\theta = 0.007$  (minimum diameter of  $2 \mu m$  and maximum diameter of  $6 \mu m$ ). Cylinders were iteratively sampled and placed within each strand cross-sectional surface until a density of 0.7 was reached (12,196 strands, see Figure 4-6 f). Sampled cylinders not fitting within the surface were discarded. The Numerical Fiber Generator optimisation procedure was performed for an additional iteration to reduce overlapping strands further and use the space left by the initial sampling procedure.

The final set of strands (trajectories and diameters) were used to generate a mesh of the substrate with the Blender software (see Figure 4-7). For each strand, a tubular mesh was generated to represent the outer surface of the axon-like structure with an additional inner tubular mesh following the same trajectory but with a diameter of 0.7 times the outer diameter, representing the inner surface of the axon-like structure. The mesh was used as input to the open-source MC/DC Simulator presented in Chapter 2.

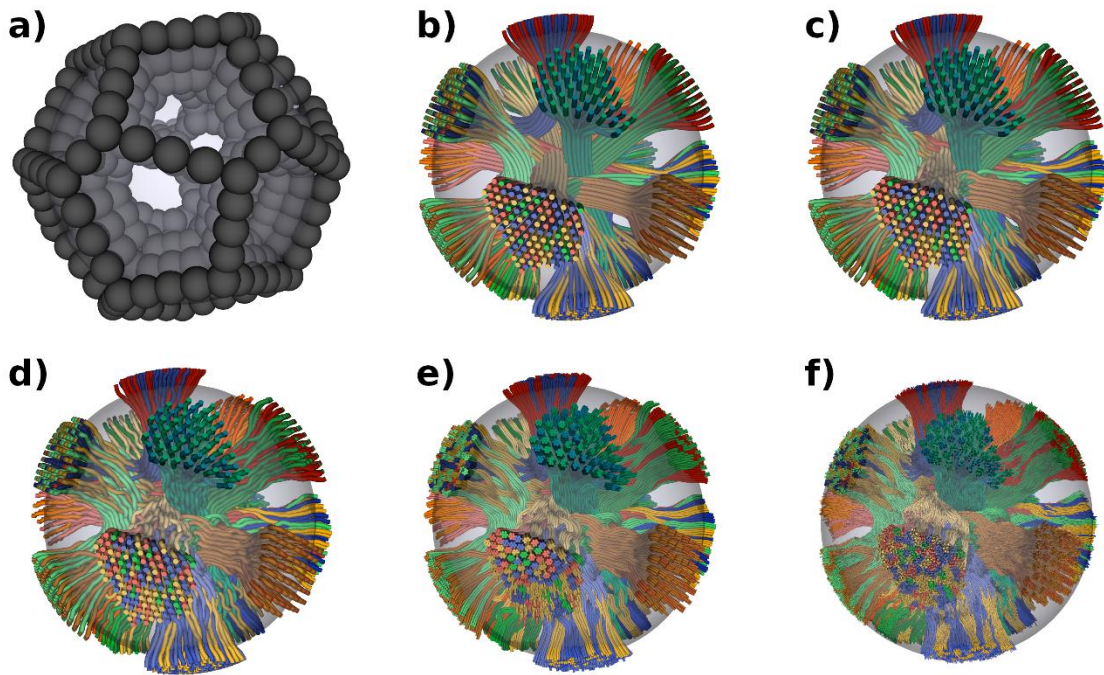


Figure 4-6 DiSCo Phantom construction steps



a) Spherical constraints located around each ROI, used to force the strands trajectories to converge toward the centre of the phantom. b) Initial strands trajectories. c, d) Strand's trajectories after 1 and 4 optimisation steps of the Numerical Fiber Generator, respectively. e) Subdivided strands following hexagonal packing. f) Strand trajectories after the optimisation process, with gamma-distributed diameters. The colours of the strands correspond to a pair of connected ROIs.

## DW-MRI Signal Simulation

All the signals were computed using the sum of the accumulated phase shift approximation implemented in the MC/DC simulator (Rafael-Patino, Romascano, *et al.*, 2020). The simulator contains routines to optimize collision detection and memory handling, allowing it to perform simulations of 3D mesh substrates containing millions of triangles and particles. We adjusted the parameters of those routines to better perform in the simulation settings and substrate size described before, allowing us to compute the full volume simulation in a feasible time. To ensure a high and uniform density in all the 64,000 computed voxels, we used a highly dense regular particle placement with a total of  $10^9$  particles to achieve a density of one particle per cubic micrometre. The total diffusion time was set to  $53.5 \times 10^{-3} s$  matching the maximum protocol's echo time, and the time between each step  $\delta t$  was set to  $5.35 \times 10^{-7} s$ . The unrestricted diffusion coefficient was set to  $0.6 \times 10^{-3} mm^2/s$  for an ex-vivo scenario. The simulated signal was computed separately by labelling all particles inside the inner-mesh as intra-axonal, those inside the outer-mesh but outside the inner mesh as *myelin*, and those outside the outer-mesh as extra-axonal. Particles initiated in the extra-axonal and intra-axonal compartments were used for the DW-MRI signal generation.

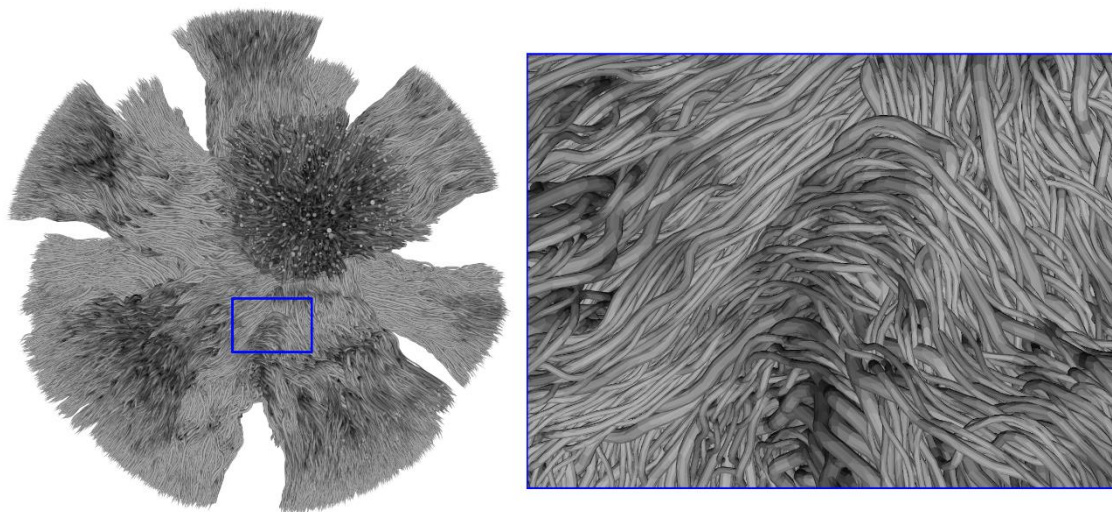


Figure 4-7 Mesh of the 12,196 strands used as input to the MC/DC diffusion simulator.

The outer mesh (used for the simulation of the extra-axonal space) contains 36,672,202 faces after post-processing.

Although the substrate was optimized to minimize strand overlaps, some overlaps remained. To account for the effect of overlapping strands in the simulated DW-MRI signal, the intra-axonal signal was generated solely using the mesh of the strand into which the particle was initiated. If a particle is initiated at a point where two strands overlap and thus within more than one strand, one of the strands was randomly chosen to simulate the intra-axonal diffusion process.

The DW-MRI protocol includes 360 diffusion-weighted images and four non-diffusion-weighted images ( $b=0$ ). The measurements are distributed on four  $b$ -shells ( $b = 1000, 1925, 3094, 13191 s/mm^2$ ). Those correspond to the three  $b$ -shells of the optimized ActiveAx protocol (Dyrby *et al.*, 2013) with an additional shell at  $b = 1000 s/mm^2$ . The echo time was set to 0.0535s. Each shell is sampled using 90 uniformly distributed gradient directions on the sphere. The resulting DW-MRI signal was corrupted using various levels of Rician noise using the Diffusion Imaging in Python (DIPY) library (Garyfallidis *et al.*, 2014).

## Resulting Dataset

The in silico DW-MRI was simulated for 360 measurements, using four b-values ( $b=1000, 1925, 3094, 13191 \text{ s/mm}^2$ ). The dataset includes the ground truth connectivity matrix, which weights correspond to the inter-sectional area of the axon-like structures forming the connections. The four-dimensional (4D) DW-MRI signal obtained is available in standard Nifti format of dimension  $40 \times 40 \times 40 \times 364$ , where the 4<sup>th</sup> dimension corresponds to the DW-MRI. The DW-MRI images corrupted with Rician noise at a signal to noise ratio (SNR) of 10, 20, 30, 40 and 50 are also generated. The 3d location of the 16 ROIs of the phantom is included as a labelled mask with all voxels of the ROIs having a corresponding value of 1 to 16. Finally, the maps of the fraction of Monte Carlo particles initiated inside the inner tubular mesh of the substrate over the total number of Monte Carlo particles used to generate the signal are included as a volume fraction metric between compartments. Additionally, the ground-truth information is included, such as the centerline trajectories of the 12,196 strands and the list of the corresponding inner diameters and the two ending ROIs labels of each strand.

All the resulting files, meshes and metrics are freely available as a test dataset for the MICCAI 2021 Diffusion Simulated Connectivity (DiSCo) challenge (Girard *et al.*, 2021)<sup>2</sup> and as a Mendeley Research dataset (Rafael-Patino *et al.*, 2021)<sup>3</sup>.

## Conclusion

This section presented the construction of a massive numerical phantom, extensive enough to run tractography algorithms, using the framework in (Rafael-Patino, Romascano, *et al.*, 2020) and discussed in the previous section. The creation of this type of phantoms shows how Monte-Carlo simulations could also be used as a cornerstone for the validation or the modelling of tractography and microstructure-informed tractography methods. This will be of great importance to machine-learning-based methods such as the one presented in

---

<sup>2</sup> [http://hardi.epfl.ch/static/events/2021\\_challenge/](http://hardi.epfl.ch/static/events/2021_challenge/)

<sup>3</sup> <https://data.mendeley.com/datasets/fgf86jdfg6/1>

Chapter 7, where the lack of ground truth information makes the validation and training of such methods a challenging task.

## 4.4 MCDS in 3d reconstructed tissue

Several studies have used histology to study and validate DW-MRI models and tissue structural assumptions. For example, for the validation of the fibre orientation dispersion, polarized light images were used in (Mollink et al., 2017), light microscopy images in (Grussu et al., 2016) and 3d confocal microscopy images in (Schilling et al., 2018). Such results can be used directly to design realistic numerical phantoms by mimicking the structural characteristics of the segmented tissue or by reconstructing the geometry directly. Figure 4-8 shows a photomicrograph and a 3d reconstruction made, which exemplifies how this can be used for MCDS of the orientation dispersion of segmented axons. Other recent studies have used 3d electron microscopy (EM) to reconstruct the axons' microstructure below the micrometre level. Such reconstructions produce realistic virtual tissues, making the study of the effect of more refined structures in the DW-MRI signal, such as the axons' diameter changes along with the fibre orientation and the micro and meso dispersion (Andersson et al., 2021). Figure 4-9 shows an example of such axonal shape reconstruction from EM data which are able to provide high-quality meshes of realistic environments for Monte-Carlo simulations.

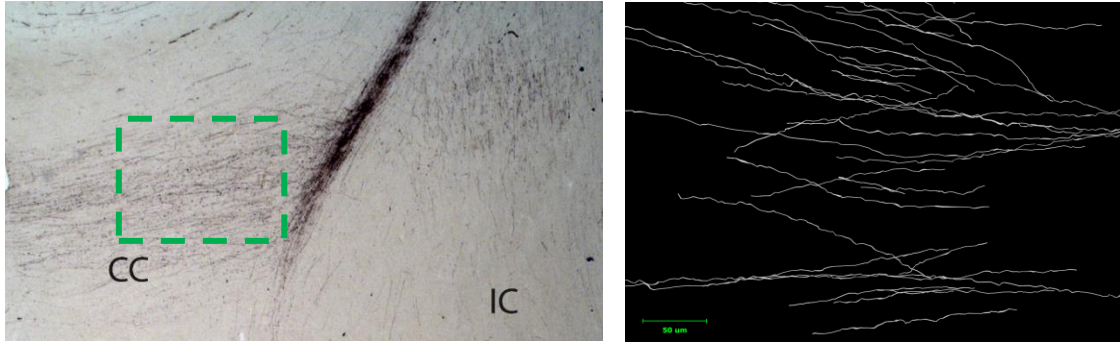


Figure 4-8 . Photomicrograph showing axons and the resulting 3d reconstruction.

(Left) Photomicrograph showing axons labeled with biotinylated dextran amine (BDA) from a cortical injection which course in a tight bundle up to where they disperse on the way to the corpus callosum (CC) and internal capsule (IC). (Right) BDA 3d reconstructed at high resolution. Notice the undulations as well as the fact that axons do not keep a parallel course but tend to cross each other (misalignment).

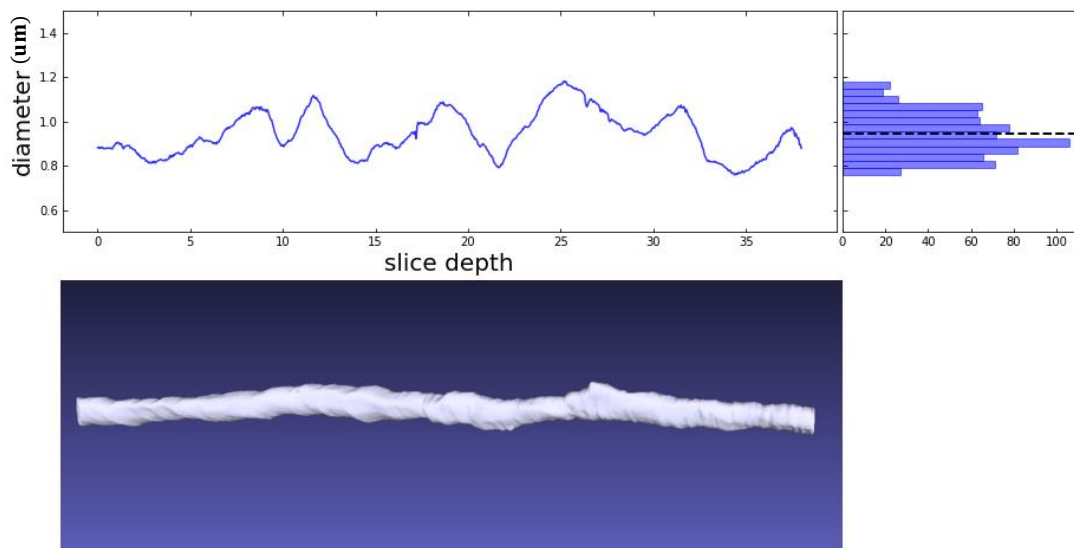


Figure 4-9 EM 3d reconstruction and quantification.

Bottom panels shows a the 3d reconstruction from serialized EM data (not shown). From the 3d reconstruction, quantifications such as the inner axon diameter along the fiber (top left panel) and its distribution (top right panel) can be measured.

In addition, such diameter changes can be induced in the numerical phantom framework explained earlier in this chapter, generating this way realistic fibre bundles mimicking the micro and meso characteristics of segmented data, as was explored in the MODERN

framework in (Rafael-Patino *et al.*, 2019). Figure 2-3 shows a substrate generated with axonal diameter changes mimicking those from segmented EM data; however, adding more microstructures characteristics makes the packing procedure more challenging, making achieving lower extra-axonal volume fractions an open problem.

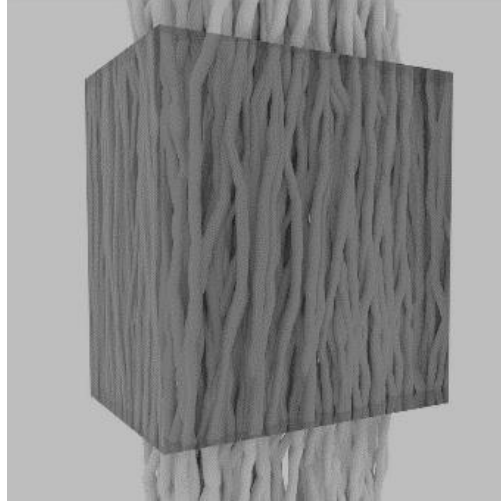


Figure 4-10 A numerical phantom using MODERN.

Axonal-like structures with mapped axonal diameter changes generated using a multi-objective differential evolution optimization procedure. The phantom contains axonal diameter changes and dispersion characteristics packed inside a target voxel.

## Conclusions

The advances in the creation of numerical phantoms of the brain's white matter, like the one presented in this chapter, will indubitably help validate and model DW-MRI methods for microstructure estimation and tractography. However, many essential structures present in real tissue are still neglected and thus could still bias the simulated DW-MRI signal towards previously used simplified models. Because of this, studies from highly accurate tissue imaging, as 3d EM reconstructions, play a vital role towards the designs of realistic and complex numerical phantoms.

## Chapter 5

# Simulation-Assisted Machine Learning

---

### 5.1 Overview

Diffusion MRI (DW-MRI) allows for the detailed exploration of the brain white matter microstructure, with applications in both research and the clinic. However, state-of-the-art methods for microstructure estimation suffer from known limitations, such as the overestimation of the mean axon diameter and the infeasibility of fitting diameter distributions. This chapter presents our recent study in simulated-based microstructure modelling proposed in (Rafael-Patino, Yu, *et al.*, 2020). In this study, we proposed to eschew current modelling-based approaches favouring a novel, simulation-assisted machine learning approach. In particular, we trained machine learning (ML) algorithms on a large dataset of simulated diffusion MRI signals from white matter regions with different axon diameter distributions and packing densities. We showed, on synthetic data, that the trained models provide an accurate and efficient estimation of microstructural parameters in-silico and from DW-MRI data with moderately high b-values ( $4000s/mm^2$ ). Further, on in-vivo data, we showed that the estimators trained from simulations can provide parameter estimates close to the values expected from histology.

## 5.2 Introduction

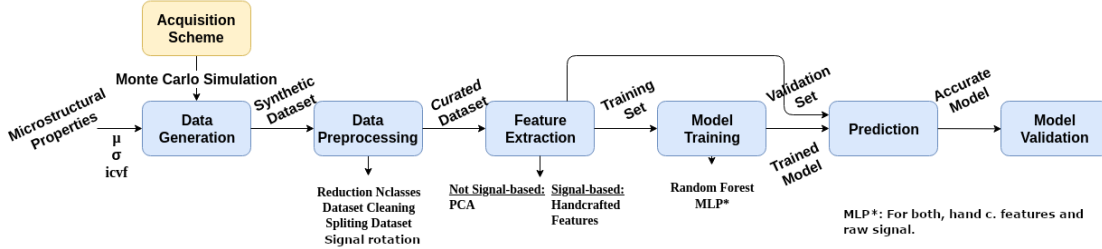


Figure 5-1 Simulation-based framework pipeline.

The proposed framework selects the microstructure properties and the acquisition protocol prior to the dataset generation. The generated data can then be used to train different models, feature-based like Random Forest (RF) and Support Vector Machines (SVM's), or directly from the output signals as the multi-layer perceptron (MLP) model.

In this study, we explored the feasibility of bypassing some of the limitations of the current inverse models by developing an emerging approach that is based on using DW-MRI simulations as a tool for performing forward modelling (Nedjati-Gilani *et al.*, 2017; Rensonnet *et al.*, 2019). In our approach, we first created an extensive and detailed dataset of numerical white matter phantoms with varying geometric properties of interest, such as the mean and standard deviation of axon diameters and axon density. We then generated the DW-MRI signals of these phantoms using the MC/DC simulator (Rafael-Patino, Romascano, *et al.*, 2020). We trained two different machine learning algorithms, i.e., random forest and multi-layer perceptron, to map the simulated signals with and without handcrafted features to the microstructural parameters. The learned models were then applied to both synthetic and in-vivo brain data.

Figure 5-1 shows the structure of our framework from the dataset generation to the accuracy evaluation. In generating the dataset, we express the DW-MRI signal in the brain white matter as the sum of the signals from the intra-axonal  $S_{int}$  and extra-axonal  $S_{ext}$  compartments, weighted by their relaxation-weighted volume fractions (icvf and ecvf, resp.) as follows:

$$S = (icvf)S_{int} + (1 - icvf)S_{ext} ,$$



where  $ecvf = 1 - icvf$ , and  $icvf + ecvf = 1$ . The intra-axonal space represents the axons, which we model as straight and parallel cylinders, and the extra-axonal space corresponds to the space outside the axons, including the extra-axonal matrix, glial cells, and cerebrospinal fluid. We further assume that within a bundle, the axon diameters follow a Gamma distribution (Sepehrband *et al.*, 2016) each bundles having different means and standard deviations.

A large dataset of white matter phantoms with different geometrical properties was generated by parameterizing the intra-axonal space with the volume fraction  $icvf$  as well as the mean  $\mu$  and standard deviation  $\sigma$  derivated from the parameters of a Gamma distribution. A packing algorithm that generates axon geometries matching these predefined parameters was implemented similar to (Hall and Alexander, 2009). Then, simulated DW-MRI signals for each one of these phantoms were generated using the MC/DC simulator with a specific acquisition protocol consisting of 2 shells with b-values equals to  $1000 \text{ s/mm}^2$  and  $4000 \text{ s/mm}^2$ ,  $\delta = 7 \text{ ms}$ , and echo time ( $TE$ ) =  $80 \text{ ms}$ , and an isotropic voxel resolution of  $2 \text{ mm}$ . For each shell, the  $\Delta$  time varied as  $\Delta = 17.3, 30, 42, 55 \text{ ms}$ . A total of 30 uniformly sampled directions in the sphere were used per different  $\Delta$  time for the shell with b-value =  $1000 \text{ s/mm}^2$  and 60 directions for the b-value =  $4000 \text{ s/mm}^2$ . In addition, to include some uncertainty related to the main fibre orientation, four additional signals were generated for each phantom by rotating the original signal by 5 degrees in 4 directions around the mean fibre direction. We chose this dispersion by computing the variance of the main fibre direction in a region of interest in the corpus callosum (CC) from the in-vivo data. The resulting substrates were removed if the packed distribution were not close enough to the desired distribution of diameters or could not reach the desired ICVF. Figure 5-2 shows an example of a generated distribution and the directions used to rotate the phantom's main direction. In total, the final database consisted of 82,400 white matter phantoms and their DW-MRI signals, which were obtained after generating different realizations of each of the 1824 combinations of  $icvf$ ,  $\mu$  and  $\sigma$  (Table 5-1) after pruning.

Parameters	Values
$\mu$	{0.2, 0.3, 0.5, 0.66, 0.81, 0.97, 1.12, 1.28, 1.44, 1.59, 1.75, 1.91, 2.06, 2.22, 2.34, 2.53, 2.69, 2.84, 3}
$\sigma$	{0.1, 0.3, 0.5, 1, 1.5, 2, 2.5, 3}
icvf	{0.35, 0.4, 0.45, 0.5, 0.53, 0.57, 0.6, 0.63, 0.67, 0.7, 0.73, 0.75}

Table 5-1 Table of values used to generate all the substrates for the mean radius ( $\mu$ ) the standard deviation of the distribution ( $\sigma$ ), and the ICVF. A total of 1824 combinations were produced.

The in-vivo data were acquired using a 3T Connectome scanner equipped with 300mT/m diffusion gradients and using the same imaging parameters to generate the synthetic dataset. The same healthy volunteer subject was scanned five times to test the method's robustness to multiple repetitions.

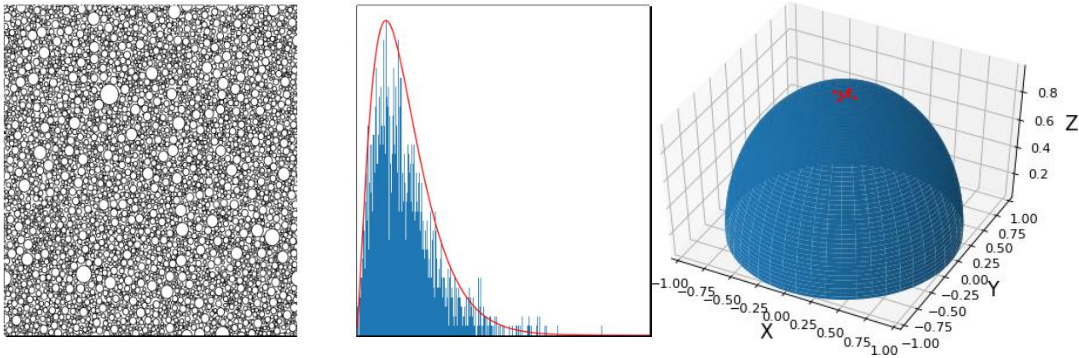


Figure 5-2 Substrate generation characteristics

From left to right, an example of a generated phantom, the resulting distribution of axons after fitting, and the directions used to rotate the main fibre direction to simulate minor angular dispersion.

### 5.3 Simulation-Assisted Machine Learning models

We implemented three approaches to learn the mapping from simulated signals to microstructural parameters, relying on either handcrafted features or the raw diffusion signal. The diffusion signal vector was separated into eight parts to create the handcrafted features. Each part corresponds to a different shell with a specific combination of the

imaging protocol parameters used, i.e.  $\Delta$ ,  $\delta$  and  $G$ . Then, for each of these, a Principal Component Analysis (PCA) was computed, and the first three components were selected, which explained more than 98% of the signal variance. In addition, the fractional anisotropy (FA) and the mean diffusivity (MD) were computed and concatenated to the feature vector. The total feature vector signal consisted of  $8 * 3 + 2 = 26$  normalized features.

The computed models were the following. First, we trained a random forest (RF) regressor using the handcrafted features described above. A total of 100 estimator trees with a maximum depth of 17 were used. The random forest parameters were optimized using the Bootstrap aggregation method. Second, a multi-layer perceptron (MLP) was trained using the same handcrafted features with the following architecture: four dense hidden layers with 129, 32, 16 and 3 units, respectively. We used a rectified linear unit (Relu) as the activation function for all layers, with dropout after the first and second layers with a probability of 0.01. The third layer was regularized using  $L_2$ -based kernel and bias regularization with a coefficient of 0.01. We used the  $L_2$  loss between the predicted and ground truth parameters as the cost function. Finally, an Adam optimizer was employed to train the network for 100 epochs with a batch size of 10. We refer to this method as MLP-feat in the rest of the results below. Third, we trained an MLP using the DW-MRI signal directly, with no feature extraction. The architecture consists of 6 hidden layers with 400, 200, 100, 56, 16 and 3 neurons. The fifth layer is a regularization layer, and all other details are identical to those used in the MLP above. We refer to this method as MLP-raw to differentiate it from the previous one trained with handcrafted features.

We used 80% of the dataset for training and validation, while 20% was held out for testing; 10-fold cross-validation to mitigate overfitting was performed. The three described approaches were tested on both the held-out synthetic data and five in-vivo DW-MRI images masked into the CC. As a baseline for the in-vivo data, we compare these results with those of the AMICO implementation of ActiveAx, using the default regularization parameters and dictionary.

## 5.4 Results and Discussion

Figure 5-3 shows the microstructure parameters estimated by the three ML algorithms from synthetic data. Our main finding is that they can accurately estimate both the mean and standard deviation of the axon diameter distributions even for diameters much smaller than those estimated in previous studies (i.e. approx.  $2\ \mu m$ ), and using an acquisition protocol employing b-values lower than the conventional ones used for diameter estimation (Dyrby *et al.*, 2013; Daducci *et al.*, 2015; Ye, 2017). To explain why the proposed ML techniques can improve the estimation of axons with smaller diameters, it is essential to remember that the model-based approaches determine the axon diameter entirely from an intra-axonal model, as the signal from the extra-axonal space is challenging to relate analytically to the underlying microstructure parameters. The limited diffusion contrast of the DW-MRI signal from the intra-axonal space along the direction perpendicular to the fibres hampers the estimation of axons with small diameters. In contrast, applying ML techniques to the whole signal allows finding hidden non-trivial and nonlinear relationships between the microstructure parameters and the DW-MRI signal from the intra- and the extra-axonal spaces. As the properties of the diffusion process in the extra-axonal space (i.e., mean displacement length, tortuosity, time-dependent diffusion) are highly influenced by the microstructure features of the intra-axonal space, the ML algorithms can exploit this additional information. Another critical factor is that, by defining a specific distribution of axon diameters in our forward model, the ML algorithms could predict the full distribution using only the information from the right-tail of the distribution, which is not affected by the contrast/resolution problem mentioned before.

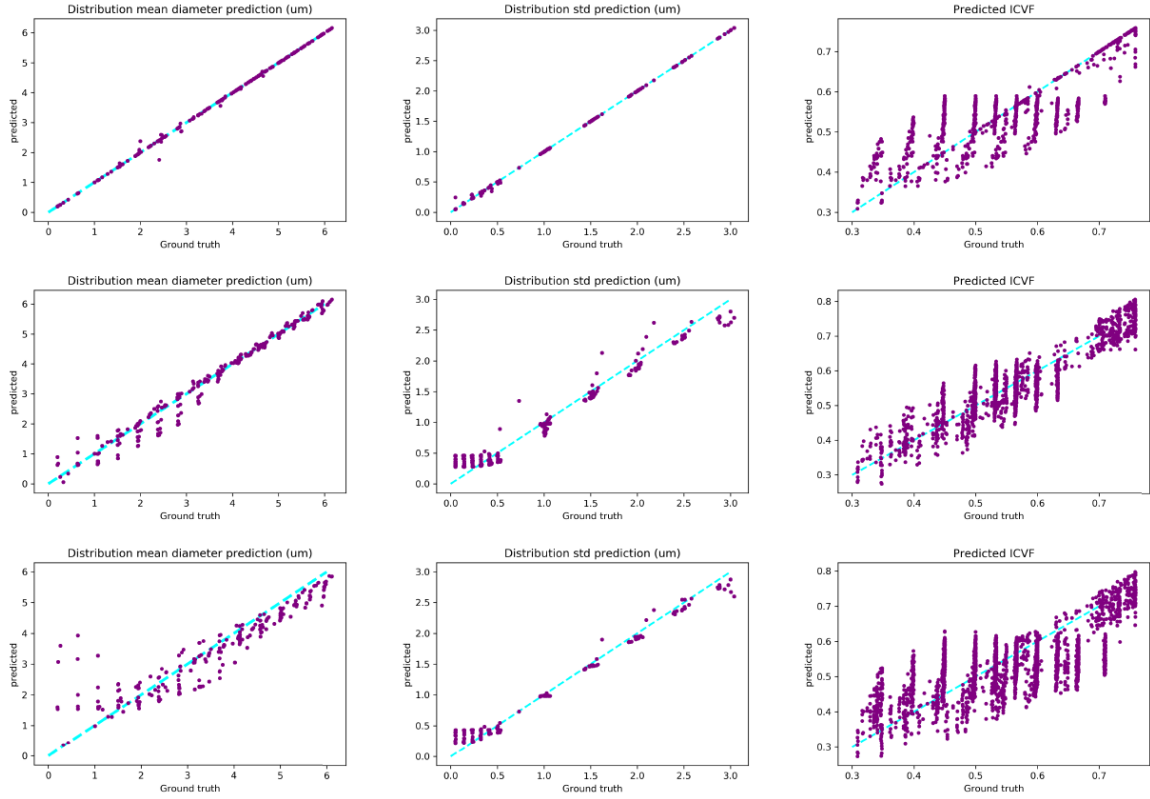


Figure 5-3 Estimates of the trained regressors on the validation dataset.

From top to bottom, results for the Random Forest (top), MLP trained with handcrafted features (middle row), and the MLP trained with the raw signal (bottom). From left to right, ground truth vs the estimated parameters on the validation dataset for the mean diameter, standard deviation, and ICVF.

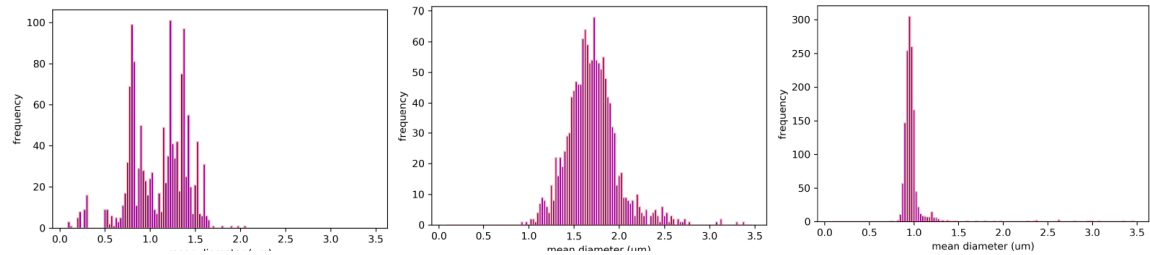
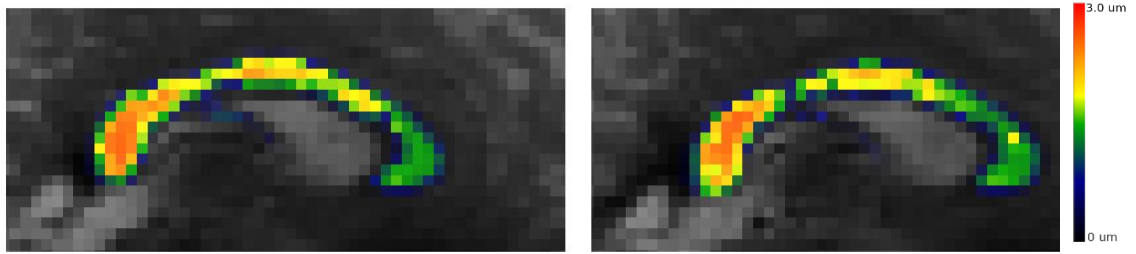


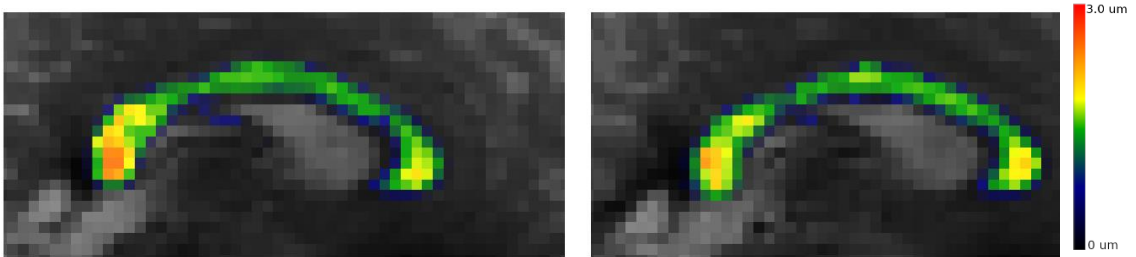
Figure 5-4 Joint histogram of the estimated mean diameters.

Joint histogram of the estimated mean diameters in the segmented mask of the CC across five scans for (from left to right) the RF regressor, MLP-feat and the MLP-raw. Each histogram was computed using the combined estimates of the five in-vivo scans.

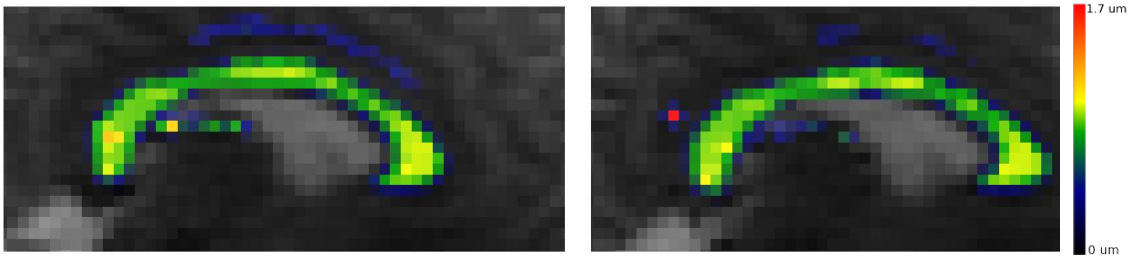
### In-vivo Random Forest $\mu D$ predictions



### In-vivo $MLP_{feat}$ $\mu D$ predictions



### In-vivo $MLP_{raw}$ $\mu D$ predictions



### In-vivo $AMICO_{ActiveAx}$ $\mu D$ predictions

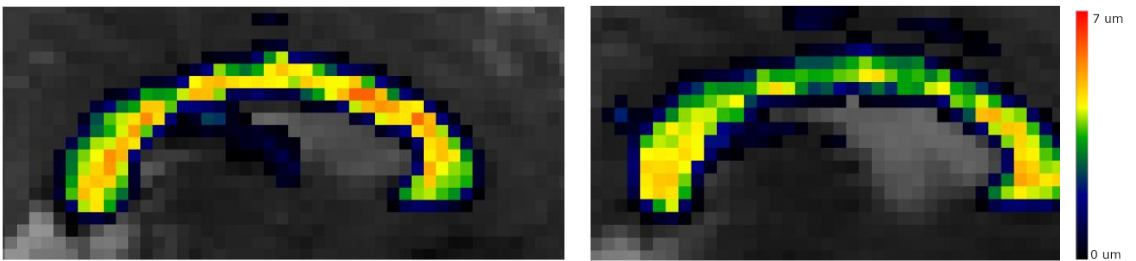


Figure 5-5 Midsagittal plane of the estimation maps for two subjects (showed from posterior to anterior).

The colour bars were adjusted per model to highlight the regions with higher and lower values. One of the MLP-raw predictions contains notorious outlier values in regions voxels outside the CC.

## 5.5 Conclusion and contributions

The main focus of this work is the introduction of an emerging simulation-based technique for microstructural parameter estimation, from the construction of a large dataset of realistic numerical phantoms to training machine learning algorithms on the corresponding simulated signals. A comprehensive dataset accounting for a wide variety of parameters characterizing axon packing, size, and small angular dispersion, mimicking that which occurs in the CC, was generated. We demonstrated that machine learning models with and without handcrafted features could accurately recover the mean and standard deviation of the axon diameter distribution on synthetic data and DW-MRI data with moderately high b-values ( $4000s/mm^2$ ). The proposed approach allowed us to estimate, for the first time, the number-weighted distribution of axon diameters, which cannot be estimated with previous DW-MRI modelling techniques. As this is the distribution conventionally reported in histological studies, this study may help to fill the gap between in-vivo DW-MRI and postmortem histology.

Furthermore, once trained, machine learning models require a few seconds of computation time for estimating the microstructure parameters in the whole-brain white matter. Finally, the in-vivo results show consistent trends and values for all five subject scans with the same ML model. However, there are qualitative differences between the different models that should be explored in future studies. Our findings show that values reported in the CC for all ML models are close to those found in histology, with the RF regressor further replicating the expected spatial trend in mean diameter (Liewald *et al.*, 2014). However, in this work, it is valuable to mention that a simplified model of the CC microstructure is employed by considering a two-compartment model that assumes that axons are completely straight cylinders, without micro-dispersion along the axons. Nevertheless, since it is straightforward to generate more realistic phantoms (e.g. axons with undulations and angular dispersion) and simulate the corresponding DW-MRI signals using state-of-the-art MC simulators, both limitations can be addressed in the future by generating more complex axon configurations without significantly modifying the machine learning models

and related parameters. Future in-silico validations will be conducted to evaluate the method's robustness as a function of the signal-to-noise ratio and acquisition protocol.



## Chapter 6

# Simulation-Assisted Protocol Optimization

---

### 6.1 Overview

In diffusion-weighted MRI, general gradient waveforms became of interest for their sensitivity to microstructure features of the brain white matter. However, the design of such waveforms remains an open problem. This chapter resumes the contribution paper presented in (Truffet *et al.*, 2020). In this article, we propose a framework for designing generalized gradient waveforms with optimized sensitivity to selected microstructure features. We presented a rotation-invariant method based on a genetic algorithm to maximize the signal's sensitivity to the intra-axonal volume fraction. The sensitivity is assessed by calculating a score based on the Fisher information matrix from Monte-Carlo simulations, which provide more flexibility and realism than traditional analytical models. As a proof of concept, we demonstrate that the optimized waveforms outperform the standard pulsed-field gradient experiments.

### 6.2 Fisher information based Optimal waveforms.

By measuring the displacement of molecules at the micrometre scale, diffusion-weighted MRI (DW-MRI) is sensitive to the fine structure of biological tissues. Biophysical models have been proposed to extract useful information about tissue microstructure in-vivo. In particular, in the brain white matter, axons have a coherent organization. Besides estimating the orientation of fibres (Tuch, 2004), one can quantify the apparent intra-axonal volume fraction (iavf), parameters of the distribution of axon radii (Yaniv, 2004; Assaf *et al.*, 2008) or orientation coherence of the fibre orientations (Zhang *et al.*, 2012).

Complementary to analytical modelling of the DW-MRI signal, Monte-Carlo simulation offers increased flexibility for the description of biological substrates and higher accuracy of the DW-MRI signal for selected microstructure configurations (Hall and Alexander, 2009; Yeh *et al.*, 2013; Rafael-Patino, Romascano, *et al.*, 2020). The signals computed using Monte-Carlo simulations were shown to be a good predictor of that measured in-vivo (Rensonnet *et al.*, 2019).

Another critical factor, besides modelling, to improve the accuracy of microstructure features estimation is the experimental design. In (Alexander, 2008), the authors present a general framework for experimental design, applied to the optimization of pulsed gradient spin echo (PGSE) sequence parameters for the estimation of the composite hindered and restricted model of diffusion (CHARMED). The same framework was later extended to oscillating gradient spin-echo (OGSE) (Drobnjak *et al.*, 2016), generalized gradient waveforms (linear-encoding) and gradient trajectories (spherical-encoding) (Drobnjak, Siow and Alexander, 2010; Drobnjak and Alexander, 2011).

In this work, we focus on the choice of gradient waveforms to optimize the sensitivity of the acquisition to the intra-axonal volume fraction (IAVF) in white matter. Using a 3d substrate model of white matter and Monte-Carlo simulation, we optimize the gradient waveforms for an increased rotation-averaged Fisher information. The search for optimized waveforms follows a particle swarm heuristic. Our optimized waveforms are compared with the PGSE sequence.

The Fisher information is a measure of how sensitive a gradient trajectory,  $g$ , is to a microstructure parameter of interest. Indeed, the Cramér-Rao bound, defined as the lower bound on the variance of any unbiased estimator, is computed as the inverse of the Fisher information (Galdos, 1980). In this study, we focus on the IAVF,  $f$ , while the other microstructure parameters are fixed. We focused on the IAVF for two main reasons: i) the IAVF is a biologically relevant index of axonal loss, and therefore a biomarker specific to several neurodegenerative diseases; ii) measuring the IAVF from clinically plausible

datasets is more accessible and less sensitive to noise than other parameters of interest, such as, e.g. axon diameter index, for which a precise estimation remains challenging for diameters below  $5 \mu m$ . We derive in the sequel the Fisher information for  $f$ , and provide implementation details for its computation using Monte-Carlo simulations.

## Signal and noise model

The signal attenuation model  $A(f, g)$  depends on the IAVF,  $f$ , and an effective DW-MRI gradient trajectory,  $\mathbf{g}(t)$ ,  $t \in [0, TE]$  (TE is the echo time). Besides, the magnitude signal in DW-MRI is corrupted by noise. As mentioned in (Alexander, 2008), it is important to consider Rician noise rather than Gaussian noise since the latter leads to an unrealistic choice of higher b-value (Aja-Fernández and Vegas-Sánchez-Ferrero, 2016). In some situations, the Rician model does not adequately describe noise properties. However, in most cases, it can be considered a valid model. The probability density function of the measured signal,  $\tilde{A}$  in noise is, with a spread parameter  $\sigma$ :

$$p(\tilde{A}; f, g, \sigma^2) = \frac{\tilde{A}}{\sigma^2} I_0 \left( \frac{A(f, g) \tilde{A}}{\sigma^2} \right) \exp \left( -\frac{A^2(f, g) + \tilde{A}^2}{2\sigma^2} \right). \quad 6-1$$

The Fisher information for the parameter  $f$  is defined as

$$F_0(\mathbf{g}, f, \sigma^2) = E \left[ \frac{\partial^2 \log p}{\partial f^2} (A; f, \mathbf{g}, \sigma^2) \right] \quad 6-2$$

The full derivation for the Fisher information  $F_0$  (not reported here) can be found in the Appendix of (Alexander, 2008); it can be computed from the estimation of the partial derivatives  $\partial A / \partial f$ . Note that in our case, there is no analytical expression for the signal attenuation; instead,  $A$  is computed using the Monte-Carlo simulator. Because of the intrinsic uncertainty in the signal, we cannot estimate these partial derivatives using classical finite difference. Therefore, we empirically propose to perform linear regression from a set of signals generated for ten values of  $f$  around the value of interest.

We note that the Fisher information depends on the value of the IAVF  $f$ . Without prior knowledge on this parameter, and to avoid introducing any bias in the acquisition design, we compute the average Fisher information over a set  $\Omega = \{0.25, 0.50, 0.75\}$ :

$$F(g, \sigma^2) = \frac{1}{|\Omega|} \sum_{f \in \Omega} F_0(g, f, \sigma^2). \quad 6-3$$

In this work, we focus on gradient trajectories with a fixed orientation,  $u \cdot S = g(t) = g(t) u$ . We want to separate the search for optimal waveforms from the search for optimal sampling directions, the latter having already received prior attention in the community (Jones, Horsfield and Simmons, 1999; Caruyer *et al.*, 2013; Cheng, Shen and Yap, 2014). Besides, to have a rotation-invariant measure, we define the sampling score,  $U$ , as the average over directions on the sphere:

$$U(g, \sigma^2) = \int_{S^2} F(g u, \sigma^2) d^2u. \quad 6-4$$

In practice, the integral in Eq. 6-4 is computed by taking advantage of the cylindrical symmetry of the substrates and considering a set of nine gradient directions, making an angle  $\theta$  with the cylinders uniformly spread in the range  $[0, \pi/2]$ . As a result, we needed to run 270 simulations (3 IAVF values, each with ten values for the linear regression and each with nine angles  $\theta$ ) to compute the score  $U(g, \sigma^2)$  for one waveform. Overall, this corresponds to 30 Monte Carlo particle trajectories files to be generated.

## Numerical substrate design

All substrates were generated assuming a two-compartment model composed of intra- and extra-axonal spaces. The intra-axonal space compartment was represented using a collection of parallel cylinders with radius sampled from a Gamma distribution  $\Gamma(2.0, 0.35) \mu m$  which is in the range of values reported from histology samples (Lamantia and Rakic, 1990; Aboitiz *et al.*, 1992). The extra-axonal space compartment corresponds to space outside the cylindrical axons, which comprise the extra-axonal matrix, glial cells, and cerebrospinal fluid. The substrates were then generated by randomly placing a total of  $10^4$  sampled cylinders into an isotropic voxel, without intersection between them, and ensuring

periodicity at the voxel boundaries. Figure 6-1, panel a), shows a toy example of a numerical substrate.

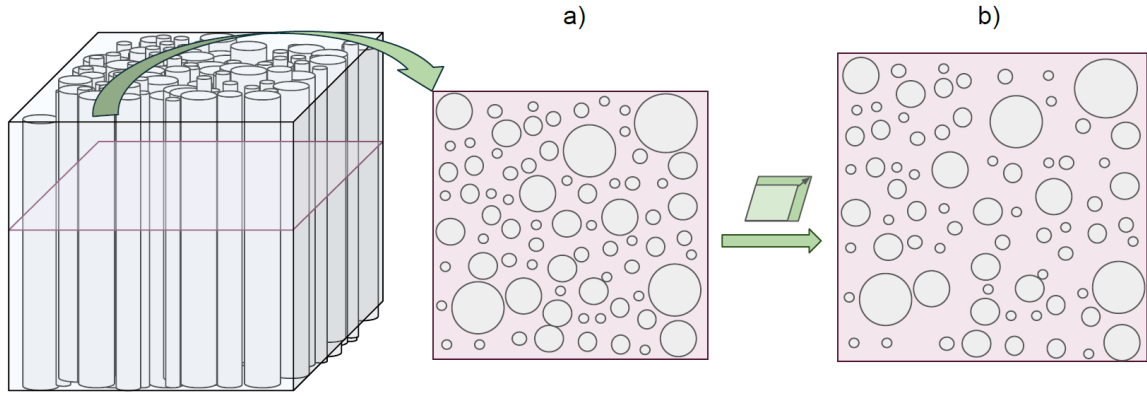


Figure 6-1 Example of substrate design composed of intra- and extra-axonal spaces.

The intra-axonal space compartment is represented using a collection of parallel cylinders with various radii packed inside a containing voxel, which results in the top view displayed in panel a). Panel b) shows how the base configuration is then transformed by scaling the voxel and the position of the cylinders by a constant factor, but without scaling the cylinder's radii; this transformation reduces the volume ratio between the voxel and the total cylinder's volume, thus reducing the represented IAVF.

A total of 40 numerical substrates were generated for four IAVF of 0.25, 0.5, 0.6, and 0.75. For each of the four nominal IAVF, we generated ten samples around the target value to compute the numerical derivative of the Fisher information. To generate samples with the same intra-axonal configuration, but slightly different IAVF, we first generated one randomly packed phantom for each of the four selected IAVF, and then scaled each one of them by a small factor  $1.0 + \epsilon$ , with  $\epsilon = \{0.00, 0.001, 0.002, \dots, 0.010\}$ , without scaling the cylinders radii distribution, as is shown in Figure 6-1, panel b). This way, the same intra-axonal space configuration is kept, but different IAVF can be computed. Doing so, we avoid any bias arising from radii re-sampling and positioning of the cylinders, which would effectively change the considered geometry, hence the signal.

To build waveforms with the highest score defined in Eq. 6-4, we perform a stochastic optimization based on a genetic algorithm. To narrow down the search space, the

admissible range of b-values is pre-determined. Intuitively, if the b-value is too low, there is almost no diffusion-weighting; conversely, a too high b-value leads to a highly attenuated signal which has an amplitude comparable to that of the noise floor. We start with an initial set of 100 random waveforms, and we perform cross-overs to build the next generation. The process to build random gradient waveforms is based on Markov Chains: the value of the waveforms at time  $t + dt$  only depends on the value of the waveform at time  $t$ . This method allows us to build waveforms that respect the properties of maximum gradient strength and slew rate that are well documented. Other limitations, such as the duty cycle, could have been added (Sjölund *et al.*, 2015) but are not documented enough to add numeric constraints. We referred to the limitations of a SIEMENS Prisma 3T for possible future experimentations:

$$|g(t)| \leq 180 \text{ mTm}^{-1} \quad ; \quad \left| \frac{dg}{dt}(t) \right| \leq 200 \text{ Tm}^{-1}\text{s}^{-1}. \quad 6-5$$

We generate the waveform between  $t = 0$  and  $t = TE/2$ , and added a symmetric portion to obtain the full gradient trajectory. Examples of randomly generated gradients are shown in Figure 6-3 (a). We generated several waveforms and selected only those that have a b-value in the targeted range.

## Evolution process

We defined the cross-over as the combination of two waveforms. We keep the beginning of a waveform, and the end of another, as shown in Figure 6-3. The position of the cut is sampled randomly from a Gaussian centred on  $TE/4$ , with a standard deviation of  $TE/12$  to avoid that the new waveform inherits too much from only one of the two previous waveforms.

Generation  $i + 1$  is built on generation  $i$ . First, we randomly select two waveforms. Then, the probability of selecting a waveform is a linear scaling of the score that leads to having a probability of selecting the waveform with the highest score ten times higher than selecting the waveform with the lowest score. If the b-value of the resulting waveform is outside the targeted range, we drop this cross-over and try another one. We repeat this

process until having 95 waveforms that fall within the target range. The last five waveforms needed to complete generation  $i + 1$  are randomly generated, such as for generation 0 to promote novelty.

## Signal simulation

The simulated DW-MRI signals were computed using DW-MRI Monte-Carlo simulations as described in Chapter 1. However, since each iteration of our proposed framework is required to recompute the DW-MRI signal of all the numerical substrates at each generation of waveforms, this requires generating a high number of new signals for the same substrate. Because of this, we proposed first to generate and store all the Monte-Carlo particles dynamics required to compute the DW-MRI signal using the MC/DC open-source simulator (Rafael-Patino, Romascano, *et al.*, 2020) and then use a tailored version of this simulator written in C++ CUDA, which is able to compute the DW-MRI signal in a fraction of the original computation time. Using the latter approach, we were able to produce one generation of waveforms in about 30 minutes, in contrast to 20 hours for the former.

For each numerical substrate, we generated and stored a total of  $2 \times 10^5$  particles, with a maximum diffusion time of 10 ms and in time-step intervals of 20 ms. The diffusion coefficient was set to  $D = 1.7 \times 10^{-9} \text{mm}^2/\text{s}$  as in (Alexander, 2008).

## 6.3 Optimized waveforms

In Figure 6-2, we report the Fisher information for several b-values ranging from 0 to  $5000 \text{s/mm}^2$ , with 100 different waveforms for each b-value. We first notice a high variability within one b-value. This shows that the b-value is not enough to characterize the efficiency of one waveform for the estimation of the IAVF. Then, we also notice that the b-value still represents an important parameter since we observe, as expected, a low score for low b-values and too high b-values. This result leads us to restrict our search for waveforms to those within the target range  $[1500 \text{s/mm}^2; 3100 \text{s/mm}^2]$ .

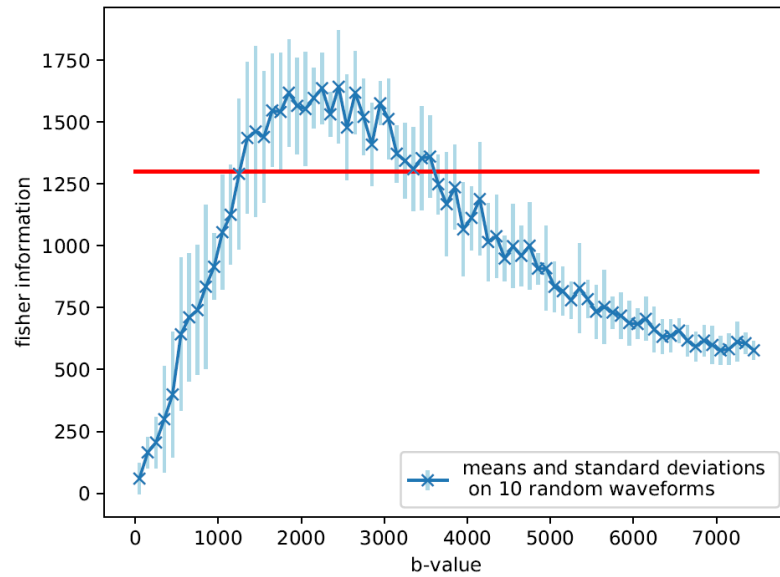


Figure 6-2 Fisher information vs b-value

Fisher information computed for a family of randomly generated gradient waveforms, spanning a range of b-values from 0 to 5,000  $s\ mm^{-2}$ . The Fisher information shows a dependence on the b-values, but within a given b-value, there is a remaining variability which is explained by waveform. We restricted our waveform search in the b-value range of [1500,3100]  $s\ mm^{-2}$  (value above the red line) to further investigate their sensitivity to the IAVF.

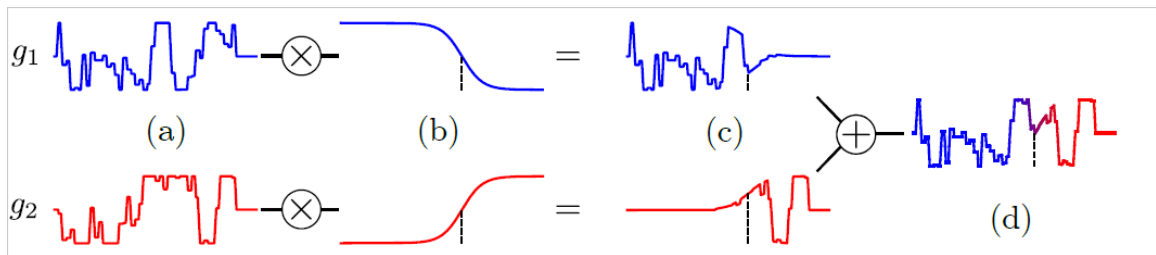


Figure 6-3 Cross-over procedure.

The cross over is performed piece-wise using a common margin point such that the resulting b-value remains almost the same.

Waveforms optimization: As we can see in Figure 6-5, after 30 generations, the score of the waveforms has increased compared to generation 0. Since most of the waveforms of generation 30 have a higher score than the random waveforms of generation 0, one can hope that this increase is due to the optimization process and not only to new random



waveforms incorporated at each generation. The waveforms with the highest score of generation 30 are shown in Figure 6-4.

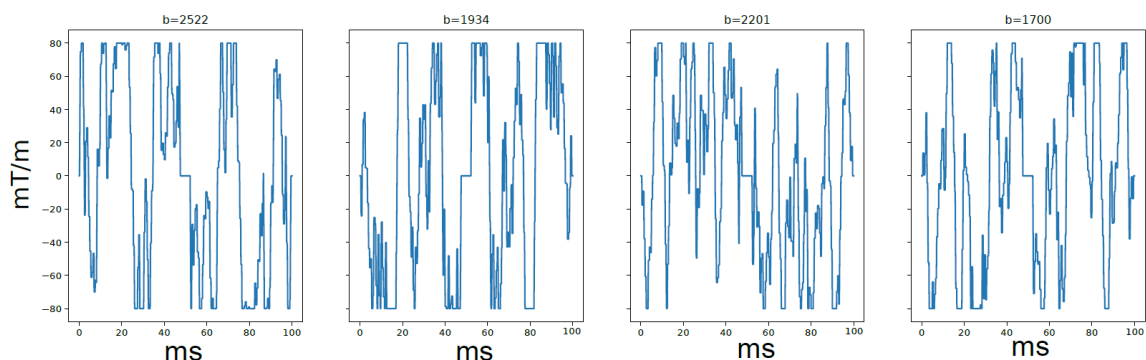


Figure 6-4 Waveforms genetically generated to optimize the Fisher Information.

From left to right, the figure shows the four waveforms of generation 30 with the highest score.

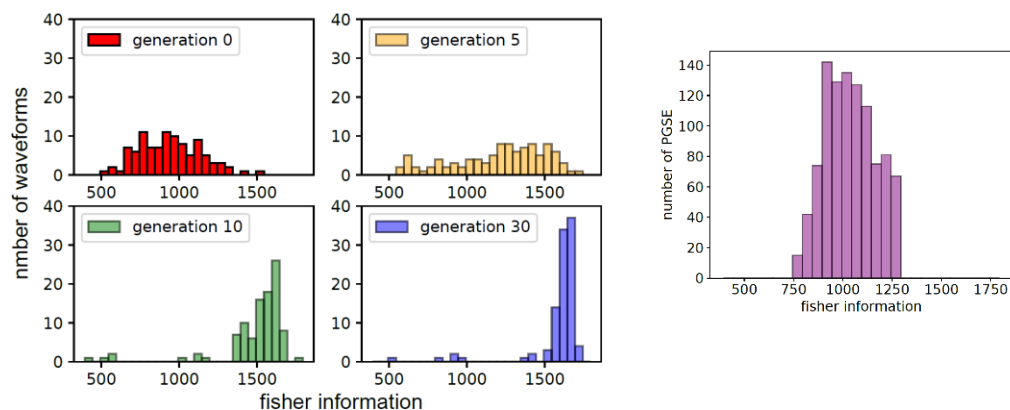


Figure 6-5 Histogram of the Fisher information of DW-MRI sequences.

The left panel shows the histogram associated with gradient waveforms across four generations of the genetic algorithm. Right, histogram computed for the family of 1,000 PGSE sequences.

As a proof-of-concept, we compared our optimized waveforms with PGSE. We computed the score for a family PGSE covering a wide range of timing and gradient amplitude parameters. We generated all the PGSE sequences with  $G_{max} = 80 \text{ mT/md}$   $\delta$  between  $0.5 \text{ ms}$  and  $40 \text{ ms}$  with a step of  $0.5 \text{ ms}$  ; and  $\Delta$  between  $10 \text{ ms}$  and  $80 \text{ ms}$  with a step of  $0.5 \text{ ms}$ . After filtering only feasible sequences and only selecting those with a b-value between 1500 and 3100, we obtained approximately 1,000 PGSE. Figure 6-5 right panel shows the distribution of scores among these PGSE sequences.

The maximum score with these b-values is lower than the score obtained with generalized waveforms in generation 30. We can also notice that, even in generation 0, some randomly generated waveforms had a higher score than PGSE sequences. This shows that generalized waveforms have a greater potential than PGSE sequences at identifying the substrate's IAVF.

## 6.4 Conclusion

The optimization of gradient waveforms is an important step in designing new acquisition sequences in DW-MRI. The generalized waveforms protocol obtained in this work is optimized independently from the sampling directions. We designed a genetic algorithm to make the waveforms evolve. After a few generations, our algorithm created a family of waveforms with a higher sensitivity to the IAVF than PGSE.

We have presented a novel framework with several advantages. First, it is based on Monte-Carlo simulations and can be adapted to various microstructure configurations, such as substrate with various compartment shapes and sizes. Second, generalized waveform optimization can be performed on one or several microstructure parameters of interest. In this work, we optimized for the IAVF parameter in two-compartment substrates composed of parallel cylinders with various radii and packing densities, but other biomarkers can be used instead. The only requirement is our ability to compute partial derivatives of the signal with respect to these parameters. Future work will target angular dispersion and spherical pore size parameter estimation. In vivo experiments will be a necessary step for the validation of the generated waveforms. Designing an experiment that shows the efficiency of the waveforms without having the ground truth microstructure is a challenging issue.

# Chapter 7

## Data-driven Machine Learning: Perspectives for the Simulation of Realistic DW-MRI Signals

---

### 7.1 Overview

In this chapter, we present two contributions on the use of data-driven machine learning models, the detection of anomalous tissue presented in (Fischi-Gomez *et al.*, 2021)<sup>4</sup> and for the use of deep learning-based autoencoders for the axon diameter estimation (Rafael-Patino *et al.*, 2019). In both works, we aimed to train data-driven methods thoroughly using the available data and forms of ground truth. However, the final aim of these studies is to explore which applications, sources of contrast and learned features could be further improved by constructing and designing tailored simulation experiments where to train and validate such approaches. Both works then served to define novel research avenues such as the DisCo simulated phantom presented before and implement additional simulation components such as multi-diffusion and multi-T2 compartment simulations discussed at the end of the chapter.

### 7.2 Anomalous Tissue Detection

The goal of this work is two-fold; first, to evaluate the prediction power of the combination of enhanced DW-MRI microstructural methods and multi-echo T2 data for the

---

<sup>4</sup> Rafael-Patino equalilly contributed author

classification of anomalous tissue. Second, we used a state-of-the-art machine learning method known for improving the prediction quality with low samples — since in our showed application in Multiple Sclerosis (MS) lesions can be very sparse and data challenging to gather — in order to test whether such *swallow* machine learning methods can predict lesions on MRI scans obtained without the use of contrast material in a localized voxel-wise level scheme.

MS is a chronic disease of the central nervous system (CNS) characterized by focal and diffuse inflammation and degeneration within the cerebral tissue (Noseworthy *et al.*, 2000). Brain inflammation leads to myelin/axonal damage and altered axonal organization, which translates to the presence of diffuse demyelination, gliosis, and axonal damage in non-lesional normal-appearing (NA) tissue. The pathological hallmark of MS is multiple focal areas of myelin loss, also known as plaques or lesions (Kerschensteiner *et al.*, 2004).

MS has an intrinsic disseminated nature (Kerschensteiner *et al.*, 2004), with individual patients differing from each other regarding clinical presentation, level of disability and number and anatomical locations of the demyelinating lesions. For MS assessment, MRI is the reference neuroimaging modality. However, the processes linked to MS pathology are difficult to visualize using conventional in-vivo imaging techniques, as they are generally limited by low pathological specificity and low sensitivity to diffused damage (Filippi and Agosta, 2007; Erzinger *et al.*, 2015; Cercignani and Bouyagub, 2018). Myelin water imaging methods appear as an appealing set of techniques for characterizing in-vivo the underlying complex geometry of the tissue, especially in the brain. The valuable compartment-specific information they provide opens the way to identifying competing diseases processes that simultaneously act on several tissue compartments, offering new insights into the pathophysiology of the disease.

Myelin-sensitive techniques exploit the tissue-specific changes in quantitative measures of proton relaxation times ( $T_1, T_2, T_2^*$ ) and semi-quantitative measures such as the magnetization transfer ratio (MTR) (Bakshi *et al.*, 2002; Neema *et al.*, 2009; Bonnier *et*

*al.*, 2015, 2016, 2017). Several mathematical models have been proposed that relate MRI-derived measures of myelin content (obtained using magnetization transfer or multicomponent relaxometry imaging) and fibre volume fraction (obtained from DWI) to the myelin g-ratio (the ratio of the inner axonal diameter to the total outer diameter). Stikov *et al.* (Stikov, 2015) proposed a model that combines the myelin volume fraction (MVF) obtained from magnetization transfer and the relative axon volume fraction (AVF) computed from NODDI. The NODDI model, however, suffers from heavy bias and poor precision due to its non-linear fitting, mainly in regions with CSF. This limitation added to the MTI limitations in inflammatory areas where extracellular water accumulates (oedema), hampers its use for myelin mapping. In (Warntjes *et al.*, 2016), authors combined R1 and R2 relaxation rates ( $R_x = 1/T_x$ ) and proton density (PD) imaging to propose a tissue model that combines the myelin and oedema in the brain. This model relates these imaging parameters to four partial volume compartments simultaneously: myelin, cellular water, free water and excess parenchymal water partial volume. The limitations of this model mainly come from the model simplification performed by the authors to allow the model to converge to a unique solution.

T2-relaxometry extracts the myelin water fraction (MWF) in the brain by resolving differentially-relaxing T2 water pools (Mackay *et al.*, 1994; Alonso-Ortiz, Levesque and Pike, 2015). By separating the short- and medium-time T2 relaxation components in the observed T2 relaxation time, these techniques differentiate between the water trapped between myelin layers (McKenzie *et al.*, 1999) and the one attributed to the intra-axonal and extracellular compartments. These models separate the water signal into three non-exchanging components: a short T2 component (between 10-40 ms) attributed to myelin; an intermediate T2 component (longer than 60 ms) arising from intra- and extra-compartments, and a long T2 component (higher than 100ms T2-relaxation time) due to cerebrospinal fluid (CSF) (MacKay and Laule, 2016). The MWF is then calculated as the short T2 relaxation component ratio relative to the total T2 distribution (Whittall *et al.*, 1997; Laule *et al.*, 2006). T2-derived MWFs have shown strong correlations with gold standard histological measures of myelin concentration. Interestingly, MWFs are also relatively insensitive to inflammation and other non-myelin-related aspects of pathology

in diseased tissues. However, imaging the whole brain at sufficiently high resolution remains challenging. The major drawback are the long scan times required to provide full-brain coverage (Piredda *et al.*, 2020), the computationally intensive (and relatively complex) post-processing, and the inherently low signal-to-noise ratio (SNR) of the MWF maps (E J Canales-Rodríguez *et al.*, 2019).

Recent improvements in MR scanner gradient performance and sequence development allow the whole-brain coverage in clinically acceptable scans times by provided sufficient high resolution and SNR. Multicomponent T2 relaxation analysis has become the gold standard to non-invasively compute the myelin water fraction (MWF) in the brain.

## Data

Twenty early-stage relapsing-remitting MS (RRMS) patients and twenty sex and age-matched healthy controls (HC) were scanned using the same 3T MRI Siemens scanner with a standard 32-channel head/neck coil. High-resolution human brain multi-echo T2 (MET2) data were collected using a prototype 3d multi-echo gradient and spin-echo sequence accelerated with CAIPIRINHA (Piredda *et al.*, 2020) using the following parameters: matrix-size = 144x126; voxel-size =  $1.8 \times 1.8 \times 1.8 \text{ mm}^3$ ; TE/N-echoes/TR =  $10.68 \text{ ms}/32/1 \text{ s}$ ; prescribed  $FA = 180^\circ$ ; number-of-slices=84; acceleration factor=3x2; number of averages = 1; acquisition time = 10:30 mins.

The dMRI acquisition consisted of a four-shell protocol, including six images at  $b = 700 \text{ s/mm}^2$ , 20 images at  $b = 2000 \text{ s/mm}^2$  and 66,  $b = 3000 \text{ s/mm}^2$ , and 11 intersperse  $b = 0$  ( $b_0$ ) images. The voxel size was  $1.8 \times 1.8 \times 1.8 \text{ mm}^3$  and the TE and TR were  $75 \text{ ms}$  and  $4500 \text{ ms}$ , respectively. Additionally, 12 reverse encoding  $b_0$  images were acquired for distortion correction. Standard MP2RAGE and FLAIR structural 3d images with voxel-size =  $1 \times 1 \times 1 \text{ mm}^3$  were also acquired for the initial radiologic evaluation of the subjects and to segment brain lesions as in (La Rosa *et al.*, 2018). Susceptibility-induced distortions were eliminated using the  $b_0$  images acquired with reversed phase-encoding polarities, and the dMRI data were corrected for eddy-currents and subjects motion using FSL tools

(Andersson and Sotiropoulos, 2015). The institutional review board approved the protocol, and all participants gave their written consent.

## Multi-component T2 reconstruction

The Extended-Phase-Graph (EPG) model (Prasloski, Mädler, *et al.*, 2012) was employed to correct for stimulated echoes due to non-ideal experimental conditions. It allowed quantifying the deviation of the flip angle (FA) from the prescribed value due to B1 field inhomogeneities and imperfect excitation pulses (Hennig, Weigel and Scheffler, 2004). In our study, the dictionary matrix was built using the EPG model with  $p = 60$  T2-logarithmically-spaced points ranging from 10 to 2000 ms (Prasloski, Rauscher, *et al.*, 2012).

The noise was partially suppressed by filtering the raw data with a 3d total variation algorithm in the first step. The filtered data were corrected for head motion by linearly registering all image volumes with different echo times to the first volume. Different dictionary matrices were generated in a second step, each corresponding to a fixed FA value from a discrete set between  $90^\circ$  and  $180^\circ$  equally spaced by  $1^\circ$ . The fitting process was carried out independently for each dictionary matrix by using the standard non-negative least squares (NNLS) method, and the actual FA was determined as the one minimizing the mean squared error. Finally, the intra-voxel T2 distribution was calculated using a regularized NNLS method (Mackay *et al.*, 1994; Whittall *et al.*, 1997) based on a second-difference Laplacian matrix that promotes smooth solutions, as described in (E J Canales-Rodríguez *et al.*, 2019). The optimal regularization parameter was determined using the L-curve methods, implemented in (Castellanos, Gómez and Guerra, 2002). The features extracted from the multi-compartment T2 reconstruction were the myelin water fraction ( $MET2_{f_M}$ ), the intra- and extra-cellular water fraction combined in a single scalar ( $MET2_{f_{IE}}$ ) and the free water fraction, corresponding primarily to free fluids such as the cerebrospinal fluid (CSF) ( $MET2_{f_{CSF}}$ ).

The resulting images were registered to the diffusion MRI native space using the acquired  $b_0$  images as reference. The non-linear registration was carried out with the Elastix software (Klein *et al.*, 2010).

## Multi-compartment microscopic diffusion MRI model

The DW-MRI data was processed using an in-house python implementation of the Spherical Mean Technique (SMT) proposed by Kaden *et al.* (Kaden *et al.*, 2016). It models brain tissue per voxel into an intra-neurite domain, containing dendrites and axons and the extra-neurite compartment that includes neurons, glial cells, and extracellular space. This technique provides estimates of neurite density unconfounded by fibre crossings and orientation dispersion. The features extracted from this model are the intra-neurite signal fraction  $SMT_{f_I}$  and the extra-cellular signal fraction  $SMT_{F_E}$ .

## Lesion identification

Lesions were segmented on T1-w and T2-w images and verified and rated by two trained neurologist. Specifically, the lesion masks consisted of a voxel-wise probability distribution map, where "healthy" voxels have a null probability of being a lesion (La Rosa *et al.*, 2018). On the training set, lesional voxels (L) were selected as voxels having a lesion score higher than 0.75 on the segmentation mask. This threshold was set to reduce the uncertainty in the lesion contours. A sharp limit was enforced in order to exclude perilesional voxels that may belong to normal-appearing tissue. The initial set of MS lesions counting for a total number of 18,441 voxels were identified and later refined and randomly sampled to build the training dataset from the patients' data. The voxels considered normal-appearing WM (NAWM) were selected by defining an external surrounding ring to each MS lesion. NAWM voxels were defined as being six voxels away for any lesion and named as (N) (see Figure 7-1). Voxels considered as healthy tissue voxels (C) were selected from the control dataset.



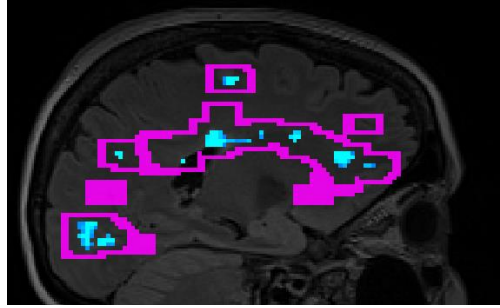


Figure 7-1 Visualization of the extracted training data for the lesions (light blue) and NAWM voxels (purple).

All voxels with a lesion score above 0.75 were chosen as training data; NAWM voxels (N) were extracted from the surrounding WM of a neighbourhood with a minimum distance of six voxels from a lesion voxel ( $\text{lesionscore} > 0$ ).

## Machine learning-based classification scores

Boosting is a successful strategy used for assembling learning since first introduced by (Freund and Schapire, 1997) in the Adaboost classifier; it combines a set of weak classifiers to form a strong classifier via an aggregation-based voting mechanism, which in addition results in a probability of classification estimate. The first weak classifiers are learned by first considering all samples as equally important, then, for the training of the second iteration of the weak classifier, the weighting of all misclassified samples is increased by adjusting the weights of the feature vectors. Hence, the second classifier will focus primarily on the previously misclassified samples and therefore on the features that better separate the remaining data. Such a strategy has proven to work well for handcrafted features from orthogonal and complementary measurements.

In this work, we used the multi-class extension of Adaboost, which performs a forward stagewise additive modelling using a multi-class exponential loss function. We corroborated through a quantitative evaluation strategy (not shown) that this method overperforms other state-of-the-art machine learning models such as SVM's and densely connected multilayer perceptron Neural Networks. The predictions were performed using as a feature set the ensemble of both SMT-dMRI and MET2 derived microstructure

parameters:  $F_{comb} = \{SMT_{f_I}, SMT_{f_E}, MET2_{f_M}, MET2_{f_{IE}}, MET2_{f_{CSF}}\}$ . For the evaluation, we maintain an MS patient dataset that was never used for training the data in any of the repetitions. Three different experiments were performed. In each of these three settings, the classifier was trained, and every repetition is used to predict to which category the voxels in the validation image belong. The classifier implementation was performed using the Scikit-learn 0.22.1 weight-Boosting module. The trained models have the following structure:

- **Experiment-1:** voxel classification in three different classes (L), (N), (C).
- **Experiment-2:** lesions versus normal-appearing WM, i.e., (L) vs (N).
- **Experiment-3:** lesions versus healthy controls, i.e., (L) vs (C).

For each experiment, we performed  $k$ -fold cross-validation with  $k = 5$ . The feature importance was also computed based on the information gain, which correlates to the feature importance to determine the splits over the aggregation procedure. Finally, instead of reporting a discrete label, we report the classification probability between lesions (L) and not lesions (N) or (C) as our "probability estimate map".

## Results

Results from the three experiments are summarized in Figure 7-2 and Table 6.1, which show, respectively, the confusion matrices of the classification and the cross-validation scores and mean accuracy for the three trained models. The first setting (L-N-C classification) shows that the combination of all features leads to a lesion detection of 77% (Figure 7-2 first panel). Most interestingly, the rate of false positives (i.e. when a healthy tissue voxel (C) is classified as a lesion (L)) is less than 1% (Figure 7-2, first column). As expected, the classification between NAWM and control voxels (N) and (C) yielded a modest classification, with almost the same percentage of true and false positives.

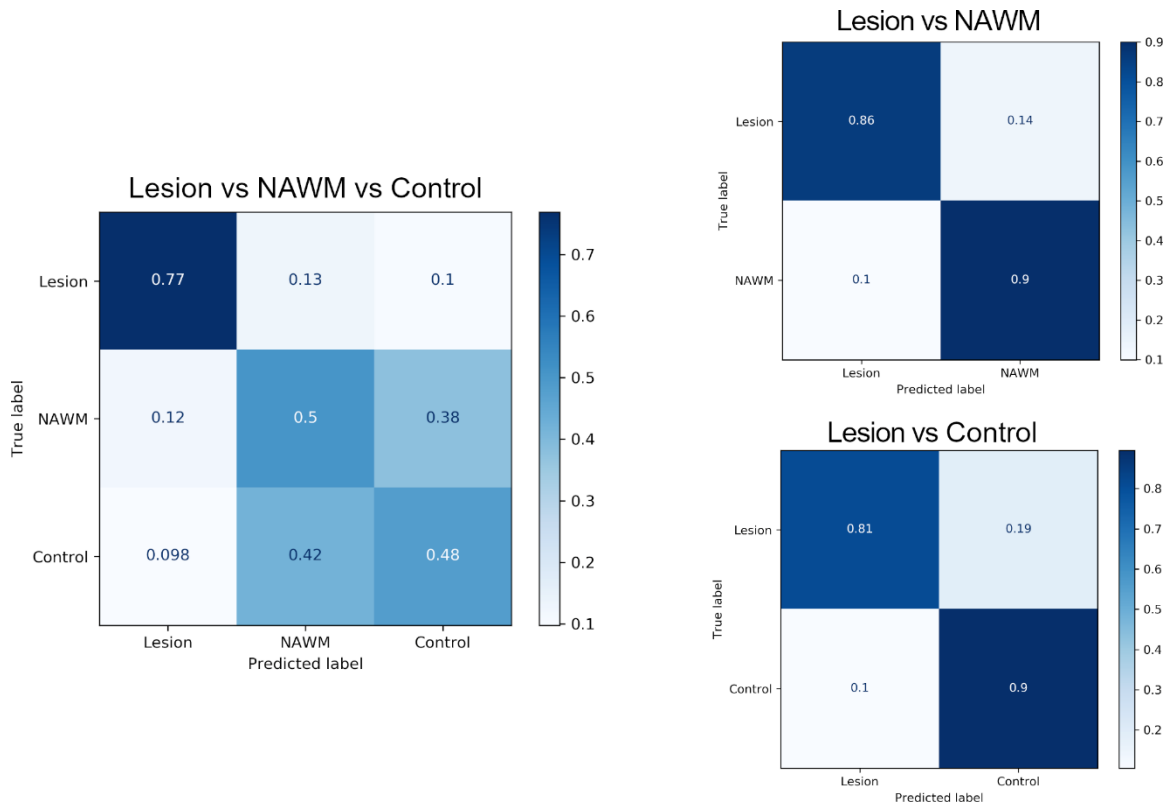


Figure 7-2 Confusion matrix of the three trained models.

The y-axis shows the true ground-truth label.

Test scores	k-1	k-2	k-3	k-4	k-5	mean accuracy
L-N-C	0.598	0.607	0.600	0.597	0.593	0.599
L-N	0.843	0.861	0.851	0.841	0.840	0.847
L-C	0.858	0.853	0.848	0.843	0.854	0.851

Table 7-1 5-folds cross-validation scores and mean accuracy for the three trained models on the test dataset.

Figure 7-2 compares the lesion probability map for two exemplary RRMS subjects extracted from the testing dataset using our proposed method with the lesion segmentation

masks extracted. While the lesions were correctly classified by our method, the resulting map highlighted voxels within the non-lesional tissue showing a diffuse abnormal pattern. These voxels were mainly located in the perilesional voxels. Moreover, voxels within the MS lesions show a gradient pattern, with the centre of the lesion having a higher score than the peripheral voxels.

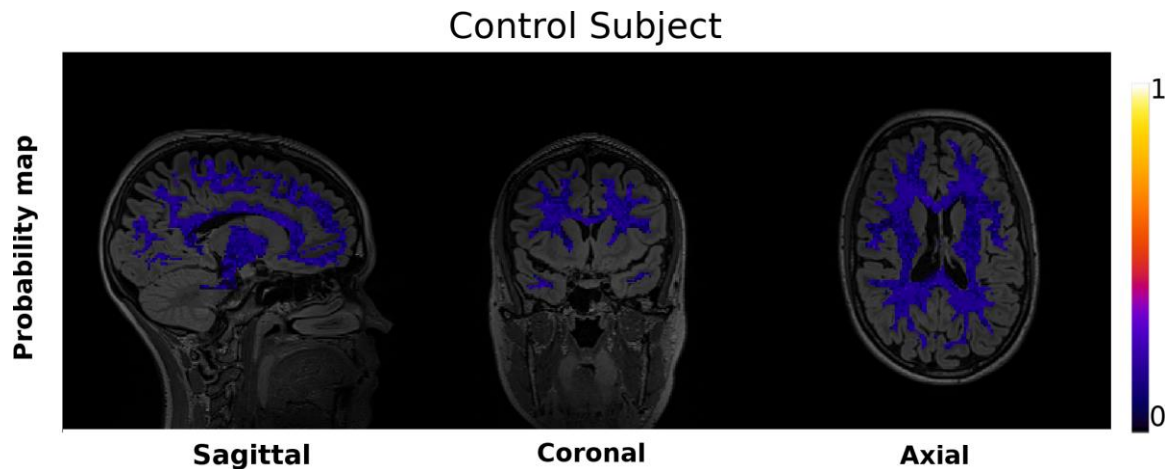


Figure 7-3 Voxel-wise lesion probability maps for one control subjects used in the validation.

Notably, all the WM voxels of the control subject were classified with an overall lower probability than that of the RRMS patients.

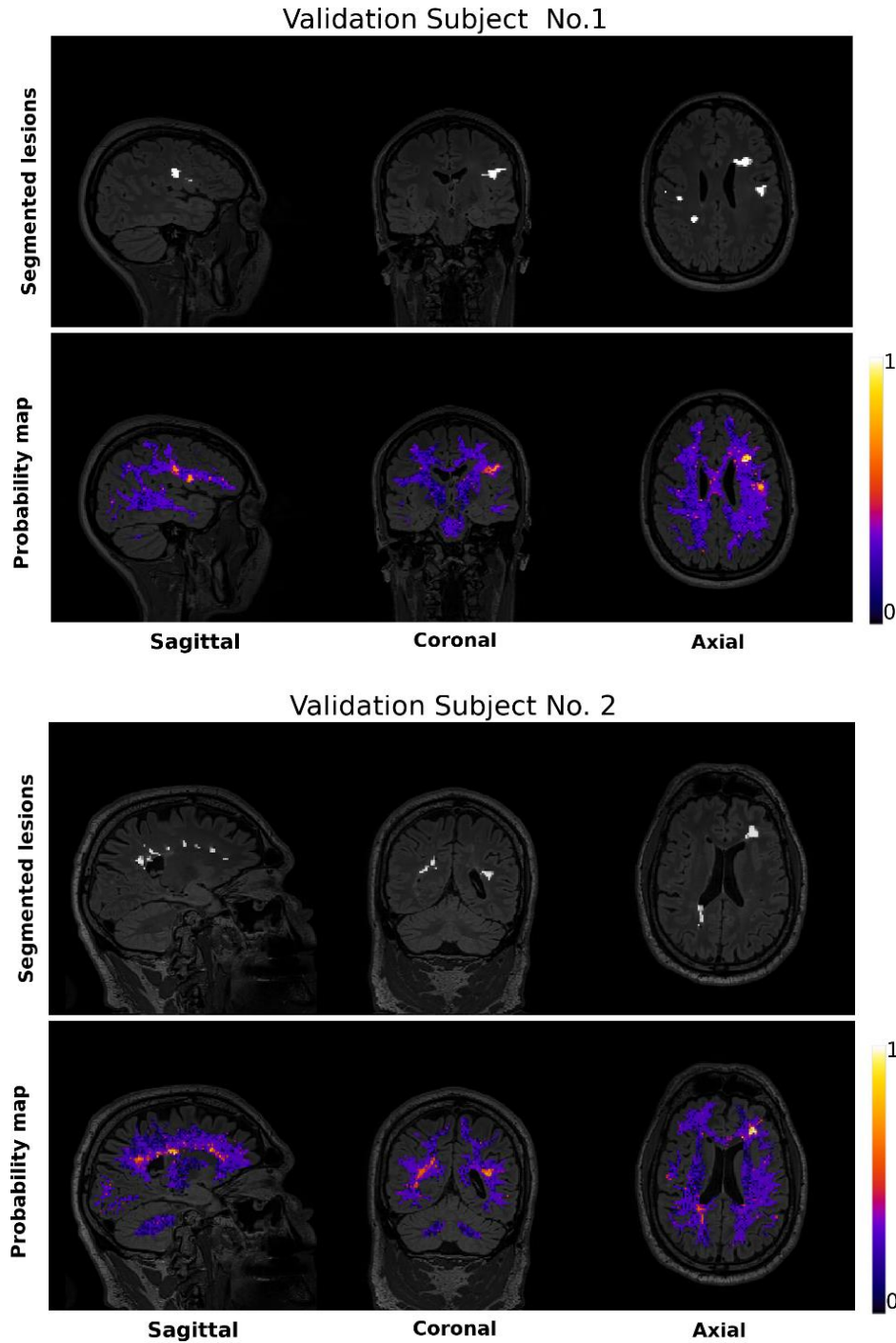


Figure 7-4 Voxel-wise lesion probability maps for two MS subjects used in the validation.

In each panel, the first row corresponds to the sagittal, coronal and axial views over the FLAIR image of the subject's lesions mask. In the second row, the same views of the lesion probability map as computed using our proposed method. The probability maps show a gradient in the lesions, with the core of the lesions having a higher lesion score and a diffuse pattern of abnormal tissue in regions otherwise considered non-lesional.

## Conclusions and perspectives

This study proposes combining multi-component diffusion MRI and T2 relaxometry models to characterize brain lesions in patients with multiple sclerosis. Our results show that combining the dMRI and T2 relaxometry features, together with an Ada-boost classifier, adds valuable complementary information for the classification of abnormal tissue otherwise considered non-lesional. The proposed approach is fully automatic and may help monitor illness progression and assess the efficacy of new treatments.

Our analysis shows that combining tissue microstructure information from multi-compartment dMRI and T2 relaxometry helps yield better delineation of MS lesions than the state-of-the-art method used for the segmentation. More interestingly, the lesion probability map, computed using our Ada-Boost classifier, highlighted a gradient pattern in the lesional voxel, concordant with previous studies showing a progressive tissue loss in the core of MS lesions (Klistorner *et al.*, 2018).

In contrast to recent studies in MS using the fractional anisotropy metric derived from DTI (Chatterjee *et al.*, 2018; Klistorner *et al.*, 2018; Lipp *et al.*, 2019), in our study, we employed a multi-shell acquisition protocol and a more complex biophysical model of the dMRI signal. The parameters estimated for this multi-compartment microscopic diffusion model are unconfounded by fibre crossings and orientation dispersion, thus providing more specific biomarkers of the tissue microstructure.

Our study has certain limitations, mainly arising from the limited dataset available. Further work will include increasing the training and testing dataset and investigating other dMRI and MET2-based features.

## 7.3 Microstructure Maps using Trainable Sparse Encoders

Diffusion-Weighted Magnetic Resonance Imaging is the only non-invasive technique available to infer the underlying brain tissue microstructure. One of the promising methods for microstructure imaging is signal modelling using the convex formulation, e.g. using the COMMIT framework. Despite the benefits of such a framework, a significant limitation is the long convergence time, making the method unappealing for clinical applications. In order to address this limitation, we propose to use a neural network to learn the sparse representation of the data and perform an end-to-end reconstruction of the microstructure estimates directly from the DW-MRI data. Our results show that the neural network can accurately estimate the microstructure maps, four orders of magnitude faster than the convex formulation.

### Introduction

In previous studies, the COMMIT framework (see Chapter 1) was successfully used to recover Axon Diameter Indices (ADI) from whole-brain tractography on ex-vivo monkey data and in-vivo human data. However, even if the convex optimization formulation brings fast estimations for simple biophysical forward models, with the increase in complexity of the forward models, the optimization procedure can reach several hours/days of computation time. In the following sections, we propose using a deep neural network to learn the sparse representation of the data and perform an end-to-end reconstruction of the microstructure estimates directly from the DW-MRI data.

### COMMIT

The COMMIT framework associates whole-brain tractography streamlines — estimating the white matter pathways — and microstructure imaging in a joint formulation. The framework is expressed as a linear equation:

$$y = Ax + \mu,$$

7-1

Where  $y$  contains the acquired DW-MRI voxels of the brain,  $A$  is a matrix generated applying multi-compartmental biophysical modelling, and  $\mu$  is the acquisition noise. The contributions  $x$  of the compartments are estimated by solving a non-negative least-square problem:

$$x = \operatorname{argmin} \|Ax - y\|_2^2.$$

7-2

The estimated coefficients  $x$ , associated with each streamline, are commonly projected back to the voxel space. This procedure generates biophysical maps allowing comparison to state-of-art voxel-based methods (Daducci *et al.*, 2015)

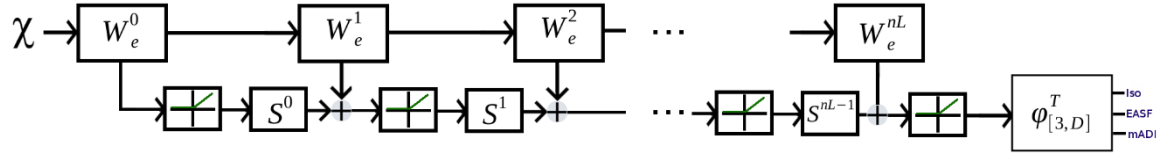


Figure 7-5 The network architecture of LISTA truncated to the number of layers.

Matrices  $W_e$  and  $S$  are learned and correspond to the learned auto-encoder. The matrix  $\phi^T$  is learned as part of the microstructure estimation rendered as a supervised learning classification.

## Learned Sparse Encoding

Sparse encoding aims to reconstruct an input signal using a linear combination of basis functions with a sparse set of coefficients. In the work of (Gregor and Lecun, 2010), a learned method that computes approximations of optimal sparse codes in a fixed amount of times was proposed. The method uses a time-unfolded neural network architecture where back-propagation through time can be applied. This method was coined Learned ISTA (LISTA) since it unfolds the popular ISTA algorithm (Beck and Teboulle, 2009), which solves the most common form of sparse encoding. This is summarized in the equation:

$$E_{W_e}(X, Y) = \frac{1}{2} \|X - W_e Y\|_2^2 + \alpha \|Y\|_1,$$



where  $W_e$  is a  $N_{signals} \times N_{atoms}$  dictionary matrix of which the columns are the basis vectors,  $\alpha$  is a coefficient controlling the sparsity penalty, and the vector  $Y$  is the signal data. ISTA finds the sparse coefficients  $X$  by iterating until convergence the following equation:

$$Y_{k+1} = h_{\theta}(W_e X + S Y_k); Y(0) = 0 ,$$

where  $W_e = W_d^T$  is the filter matrix,  $S = (I - \theta W_d^T W_d)$  is the mutual inhibition matrix  $\theta$ -weighted, and  $h_{\theta}(\cdot)$  is the shrinkage function (Gregor and Lecun, 2010). The idea of LISTA is to unfold the iterative process in Eq. 7-3 and map it into a sequential neural network, as shown in Figure 7-5.

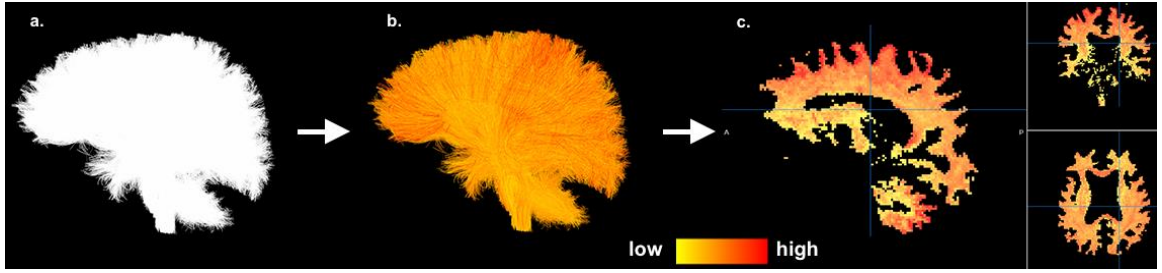


Figure 7-6 Voxel-wise map of the mean Axon Diameter Index

a) Whole-brain tractography of one of the subjects of the HCP dataset; the white colour of the streamlines means that no quantitative information is associated with the tractography; b) Whole-brain tractography with streamlines coloured according to the Axon Diameter Index (ADI) estimated using the COMMIT framework; c) Voxel-wise map of the mean Axon Diameter Index (mADI); left: sagittal view, top right: coronal view; bottom right: axial view.

## Sparse Encoding for Microstructure Estimation.

In a previously proposed framework, (Daducci *et al.*, 2015) used sparse encoding to infer microstructure information using dictionaries of microstructure compartmentalized signals, coined as AMICO. More recently (Ye, 2017) used the LISTA architecture to learn

microstructure properties by mimicking the computation of the Neurite Orientation Dispersion and Density Imaging (NODDI) estimates as proposed in AMICO.

Inspired by (Ye, 2017) we propose to learn the sparse representation of the voxel-wise mean Axon Diameter Index (*mADI*) computed with the COMMIT. Differently from local microstructure frameworks like AMICO, where the estimations are computed voxel-by-voxel independently, COMMIT computes the microstructure properties jointly for the whole-brain, using the geometry of the streamlines to create voxel connections. We use the LISTA Network architecture to map the voxel-wise DW-MRI signal to the estimated *mADI* by adding a complete connected layer that maps directly into the learned coefficients.

## In-Vivo Dataset and Processing

We used 34 subjects of the MGH-USC Human Connectome Project (HCP) Adult Diffusion Dataset. The DW-MRI acquisition scheme consists of 552 q-space samples over four shells with  $b = 1, 3, 5, 10 \text{ ms}/\mu\text{m}^2$  and 40  $b = 0$  images. The DW-MRI images were acquired at  $1.5 \text{ mm}$  isotropic voxel size (Spin-echo EPI sequence,  $TR/TE = 8800/57 \text{ ms}$ ,  $\delta = 12.9 \text{ ms}$ ,  $\Delta = 21.8 \text{ ms}$ ). DW-MRI images were corrected for motion and EDDY currents. The fibre Orientation Distribution Functions (ODFs) were computed using a single averaged fibre response (white matter voxels with fractional anisotropy above 0.7) as input for the spherical deconvolution (Tournier, Calamante and Connelly, 2007; Erick Jorge Canales-Rodríguez *et al.*, 2019) on single-shell DW-MRI images ( $b = 3 \text{ ms}/\mu\text{m}^2$  and a maximum spherical harmonic order 8). Partial Volume Estimates (PVEs) for the white matter, grey matter and cerebrospinal fluid were obtained from the provided T1-weighted using FSL/FAST (Zhang *et al.*, 2005). We used the PVEs as input for the probabilistic Particle Filtering Tractography (PFT) algorithm, and ten streamlines were initiated per voxel of the white matter volume; the resulting streamlines are shown in Figure 7-6 a.

We used the COMMIT framework to estimate the ADI coefficients for each streamline, Figure 7-6, b, and the Extra Axonal Signal Fraction (EASF) for each voxel. The mean Axon Diameter Index (*mADI*) (shown in Figure 7-6) is reported voxel-wise as:

$$mADI = \frac{\sum_s^S w_s \cdot l_s \cdot ADI_s}{\sum_s^S w_s \cdot l_s}, \quad 7-5$$

where  $S$  is the set of all streamlines crossing the voxel,  $ADI_s$  is the ADI of the streamline  $s$ ,  $l_s$  is the length of the segment intersecting the voxel, and  $w_s$  is the intra-axonal contribution of the streamlines.

## Results

Figure 7-7 shows the mADI and the EASF maps obtained for a single volume in the test dataset from both the Neural Network (NN) and COMMIT. The bottom row shows the difference map between both estimations. The overall mean ( $\mu$ ) and standard deviation ( $\sigma$ ) of the mADI and ECSF error, calculated as the difference between the estimations of COMMIT and the NN over 14 training subjects, were  $\mu = 0.627$  and  $\sigma = 0.083$ , and  $\mu = 0.028$  and  $\sigma = 0.003$ , respectively. In addition, a regular trend of high mADI estimations near the Corpus Callosum (CC) can be observed in both COMMIT and NN methods and a decrease of the EASF in both maps in the same CC regions. The average computation time for COMMIT was approximately 15 hours per subject on a machine with 12 cores, while with NN, the computation time went down to a few seconds per subject using an NVIDIA Titan Xp GPU.

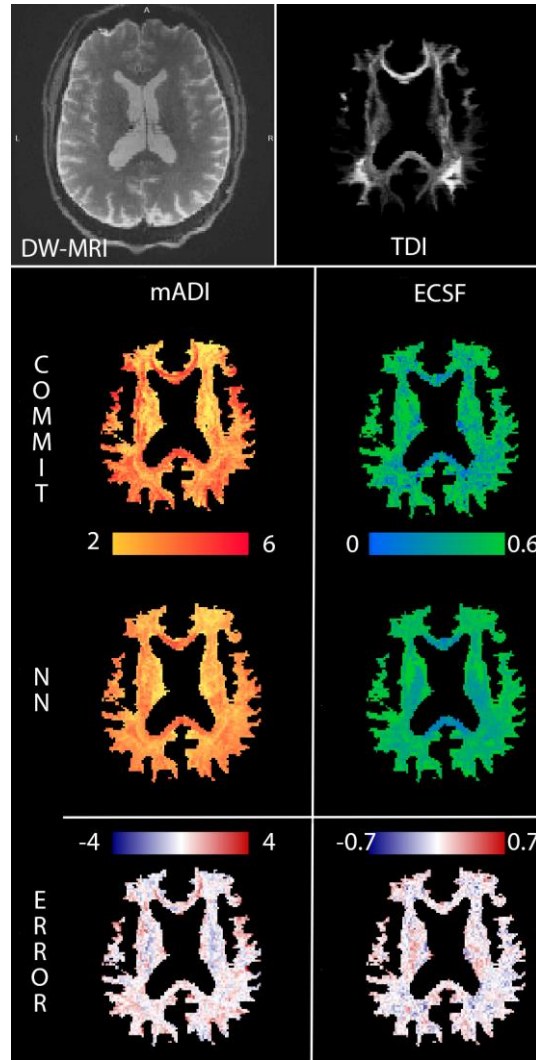


Figure 7-7 DNN vs COMMIT bases mADI results.

a) axial view of the  $b_0$  image. b) Track Density Imaging (TDI), counting the number of tractography streamlines passing through each voxel. c) Top: mADI map estimated with COMMIT; bottom: mADI map estimated with the neural network (NN). d) Top: EASF map estimated with COMMIT; bottom: ECSF estimated with the NN. e) Map of the difference between the mADI estimated with COMMIT and with the NN. f) Map of the difference between EASF estimated with COMMIT and with the NN.

## Conclusions

In this work, we present a preliminary exploration of the use of learned sparse encoders to estimate tissue microstructure properties derived from a whole-brain tractography informed microstructure framework, i.e. COMMIT. The first advantage of the proposed method is the speed up in computation time of the microstructure maps from several hours

for COMMIT to a few seconds. The second advantage is that the learned network can compute the microstructure maps directly from the raw DW-MRI data, and thus it does not require tractography methods. The results presented in this work shows the feasibility of this approach to replicate such maps accurately.

The presented work is exploratory, and further experiments will be carried out to address some limitations, such as the quality of the microstructure maps. This can be done using data with higher diffusion gradients strength to improve the sensitivity to smaller axon diameters' indices. Finally, a thorough comparison of the network's architecture and convergence against more robust architectures will be considered in future work.

## Chapter 8 Conclusions and Perspectives

---

The purpose of this thesis was to investigate the modelling and reconstruction of DW-MRI signals from the brain's WM using Monte-Carlo diffusion simulations, with applications ranging from protocol optimization to microstructure estimation.

Our first notably contribution is the design and development of the MCDC (Section 3.4 ), a robust, fast and open-source Monte-Carlo DW-MRI simulator. Our simulator is capable of performing groundbreaking simulations, which has open the door to new studies on the diffusion properties of realistic WM microstructure (Andersson *et al.*, 2021), the validation of models for the axon diameter distribution estimation in the WM (Romascano *et al.*, 2020), signal peak estimation on novel DW-MRI sequences (Rensonnet *et al.*, 2020). The simulator is in constant development and available for the scientific community. Hence our future work will focus on extending the simulator capabilities.

An interdependent part of the generation of realistic Monte-Carlo simulations is the creation of accurate virtual tissue models. In our work, we extended an existing method for the creation of composite white matter bundles configurations and extended it into a framework for creating complex substrates for Monte-Carlo simulations (Chapter 4). We created a Diffusion Simulated Connectivity Phantom with this framework (Section 4.3 ), a one-of-a-kind numerical phantom with unheard dimensions and complexity. The phantoms dimensions and complexity make it an exceptional environment for validating joint tractography and microstructure models. Furthermore, we have presented two new constructed phantoms as a collaborative tractography and connectivity estimation challenge in MICCAI's 2021 conference. However, this framework can still be further improved, for example, by adding more accurate refine structures found in the natural axonal tissue, such as axons diameter variations, the presence of non-myelinated (and thus

permeable) structures, and densely high packed regions. Thus, future studies on the segmentation and reconstruction of hyper-realistic axonal 3d models, like the one presented in (Andersson *et al.*, 2021), will ultimately guide the development of new frameworks for the generation of hyper-realistic virtual tissue models.

In the second part of our contribution work, we have focused on applications of our novel simulator as a forward modelling tool for the generation of simulation-assisted frameworks. Here, we have shown two key applications of this. The first contribution paper uses simulations to generate a massive number of simulated data for training Machine Learning-based microstructure models (Chapter 5). We were able to show that the trained models with and without handcrafted features could accurately recover the mean and standard deviation of the axon diameter distribution on synthetic data and DW-MRI data with moderately high b-values ( $4000\text{s/mm}^2$ ). However, the simulated data in this work can still be further improved by considering more than a two-compartment model and axonal trajectories with micro-dispersion along the axons. As before, this limitation can be addressed in the future by generating more complex and realistic axonal configurations, remarkably, without significantly modifying the machine learning models and related parameters from this study.

Our second simulated-assisted model tackles the problem of creating DW-MRI sequences optimized for the reconstruction of a microstructure feature of interest (Chapter 6). The key element in this study relies upon the performance and flexibility of our simulator, which makes it feasible to compute the DWI signal fast and robustly enough to approximate first-order derivatives of the waveform optimization procedure on the go. Our framework — which relies on maximizing the Fisher information derived for a microstructure feature of interest (the IAVF in our case scenario) — can create a family of waveforms with a higher sensitivity to the IAVF than those from optimized PGSE sequences. Our future work will target more challenging microstructure properties, such as angular dispersion and spherical pore size parameter estimation. More importantly, however, accounting for in-vivo experiments will be an essential step for validating the generated waveforms.

Finally, the third part of the thesis presents a data-driven exploration of two challenging scenarios of our simulation-based approach (Chapter 7). The first application tackles the characterization of anomalous tissue, which by its nature, is more challenging to characterize and study than healthy segmented tissue. Our results on such cases showed that combining tissue microstructure information from multi-compartment DW-MRI and T2 relaxometry can accurately delineate MS lesions at the individual voxel level. As future work, and in order to apply our simulated-based strategy to this study, we have further developed our simulation framework to account for multiple diffusion compartments and T2 relaxometry effects (Rafael-Patino, Girard, *et al.*, 2020). These extensions are a first step forward towards the characterization of the structural changes in pathology. However, work regarding other possible effects on MS, such as demyelination — and thus changes in the tissue's permeability conditions — are open challenges that we will address in future work.

The final data-driven application explores the use of deep learning-based methods to learn microstructure features from COMMIT-mADI, which uses the global information of a tractogram to model the local axonal microstructure. Such an approach presents several remarkable challenges. The first arises from the learned model need to use the outputs maps from another computed model as COMMIT, which, as discussed before, suffers from previous models' limitations based on simplified geometries. The second challenge is constructing and computing suitable substrates and their corresponding simulation, requiring a complete tractogram spawning several voxels. Both constraints have been successfully addressed with our constructed DisCo phantom, from which we can use the ground-truth information of the phantom's optimized trajectories and virtually generated microstructure to train from scratch a simulated-assisted version of the deep-learning based work presented.

All the contributions presented here summarise our particular effort towards novel, robust, and accurate DW-MRI microstructure models; from the first step on the signal modelling to the final inverse modelling for microstructure estimation. It is our hope that our



simulated-based approach, along with the simulator developed in this thesis, will help to produce novel and reproducible research in microstructure imaging.

# References

- Abdollahzadeh, A. *et al.* (2019) ‘Automated 3D Axonal Morphometry of White Matter’, *Scientific Reports*. Nature Publishing Group, 9(1), pp. 1–16. doi: 10.1038/s41598-019-42648-2.
- Abdollahzadeh, A. *et al.* (2021) ‘DeepACSON automated segmentation of white matter in 3D electron microscopy’, *Communications Biology*. Nature Research, 4(1), pp. 1–14. doi: 10.1038/s42003-021-01699-w.
- Aboitiz, F. *et al.* (1992) ‘Fiber composition of the human corpus callosum’, *Brain Research*, 598(1–2), pp. 143–153. doi: 10.1016/0006-8993(92)90178-C.
- Agarwal, P. K. *et al.* (2001) ‘Box-trees and R-trees with Near-optimal Query Time’, in *Proceedings of the Seventeenth Annual Symposium on Computational Geometry*. New York, NY, USA: ACM (SCG ’01), pp. 124–133. doi: 10.1145/378583.378645.
- Aja-Fernández, S. and Vegas-Sánchez-Ferrero, G. (2016) ‘The Problem of Noise in MRI’, in *Statistical Analysis of Noise in MRI*. Springer International Publishing, pp. 1–6. doi: 10.1007/978-3-319-39934-8\_1.
- Albert Einstein (1956) ‘Investigations on the theory of the Brownian movement’.
- Alexander, D. C. (2008) ‘A general framework for experiment design in diffusion MRI and its application in measuring direct tissue-microstructure features.’, *Magnetic Resonance in Medicine*. John Wiley and Sons Inc., 60(2), pp. 439–448. doi: 10.1002/mrm.21646.
- Alexander, D. C. *et al.* (2010) ‘Orientationally invariant indices of axon diameter and density from diffusion MRI’, *NeuroImage*. Elsevier Inc., 52(4), pp. 1374–1389. doi: 10.1016/j.neuroimage.2010.05.043.
- Alexander, D. C. *et al.* (2017) ‘Imaging brain microstructure with diffusion MRI: Practicality and applications’, *NMR in Biomedicine*, (September), pp. 1–26. doi: 10.1002/nbm.3841.
- Allison C. Bain David I. Shreiber, D. F. M. (2004) ‘Modeling of Microstructural Kinematics During Simple Elongation of Central Nervous System Tissue’, *J. Biomech Eng*, (6). doi: 10.1115/1.1632627.
- Alonso-Ortiz, E., Levesque, I. R. and Pike, G. B. (2015) ‘MRI-based myelin water imaging: A technical review’, *Magn Reson Med*, 24(4), pp. 515–525.
- Andersson, J. L. R. and Sotiropoulos, S. N. (2015) ‘An integrated approach to correction for off-resonance effects and subject movement in diffusion MR imaging’, *Neuroimage*, 125, pp. 1063–1078.
- Andersson, M. *et al.* (2021) ‘Axon morphology is modulated by the local environment and impacts the noninvasive investigation of its structure–function relationship’, *Proceedings of the National Academy of Sciences of the United States of America*. National Academy of Sciences,

117(52), pp. 33649–33659. doi: 10.1073/PNAS.2012533117.

Assaf, Y. *et al.* (2008) ‘AxCaliber: A method for measuring axon diameter distribution from diffusion MRI’, *Magnetic Resonance in Medicine*. John Wiley and Sons Inc., 59(6), pp. 1347–1354. doi: 10.1002/mrm.21577.

Assaf, Y. and Basser, P. J. (2005) ‘Composite hindered and restricted model of diffusion (CHARMED) MR imaging of the human brain’, *NeuroImage*. Neuroimage, 27(1), pp. 48–58. doi: 10.1016/j.neuroimage.2005.03.042.

Bakshi, R. *et al.* (2002) ‘T2 hypointensity in the deep gray matter of patients with multiple sclerosis: a quantitative magnetic resonance imaging study’, *Arch Neurol*, 59(1), pp. 62–68.

Balls, G. T. and Frank, L. R. (2009) ‘A simulation environment for diffusion weighted MR experiments in complex media’, *Magnetic Resonance in Medicine*, 62(3), p. 771. doi: 10.1002/mrm.22033.

Barazany, D., Basser, P. J. and Assaf, Y. (2009) ‘In vivo measurement of axon diameter distribution in the corpus callosum of rat brain’, *Brain*. Oxford University Press, 132(5), pp. 1210–1220. doi: 10.1093/brain/awp042.

Beck, A. and Teboulle, M. (2009) ‘A Fast Iterative Shrinkage-Thresholding Algorithm’, *Society for Industrial and Applied Mathematics Journal on Imaging Sciences*, 2(1), pp. 183–202. doi: 10.1137/080716542.

Benjamini, D. *et al.* (2016) ‘White matter microstructure from nonparametric axon diameter distribution mapping’, *Neuroimage*, 135, pp. 333–344. doi: 10.1016/j.neuroimage.2016.04.052.

Le Bihan, D. *et al.* (1986) ‘MR imaging of intravoxel incoherent motions: Application to diffusion and perfusion in neurologic disorders’, *Radiology*. Radiology, 161(2), pp. 401–407. doi: 10.1148/radiology.161.2.3763909.

Bihan, D. Le (2013) ‘Apparent diffusion coefficient and beyond : What diffusion mr imaging can tell us about tissue structure’, *Radiology*. Radiology, pp. 318–322. doi: 10.1148/radiol.13130420.

Le Bihan, D. and Iima, M. (2015) ‘Diffusion magnetic resonance imaging: What water tells us about biological tissues’, *PLoS Biology*. Public Library of Science, 13(7), p. e1002203. doi: 10.1371/journal.pbio.1002203.

Bonnier, G. *et al.* (2015) ‘Multicontrast MRI Quantification of Focal Inflammation and Degeneration in Multiple Sclerosis’, *BioMed Res Internat*, 569123. doi: 10.1155/2015/569123.

Bonnier, G. *et al.* (2016) ‘A new approach for deep gray matter analysis using partial volume estimation’, *PLoS One*, 11(2), p. e0148631.

Bonnier, G. *et al.* (2017) ‘The combined quantification and interpretation of multiple quantitative magnetic resonance imaging metrics enlightens longitudinal changes compatible with brain repair in Relapsing-Remitting Multiple Sclerosis patients’, *Front Neurol*, 8, p. 506. doi: 10.3389/fneur.2017.00506.

Brusini, L., Menegaz, G. and Nilsson, M. (2019) ‘Monte Carlo simulations of water exchange

through myelin wraps: Implications for diffusion MRI', *IEEE Transactions on Medical Imaging*. Institute of Electrical and Electronics Engineers Inc., 38(6), pp. 1438–1445. doi: 10.1109/TMI.2019.2894398.

Burcaw, L. M., Fieremans, E. and Novikov, D. S. (2015) 'Mesoscopic structure of neuronal tracts from time-dependent diffusion', *NeuroImage*. Elsevier Inc., 114, pp. 18–37. doi: 10.1016/j.neuroimage.2015.03.061.

Buxton, R. B. (2009) *Introduction to functional magnetic resonance imaging: Principles and techniques*, *Introduction to Functional Magnetic Resonance Imaging: Principles and Techniques*. Cambridge University Press. doi: 10.1017/CBO9780511605505.

Canales-Rodríguez, E J *et al.* (2019) 'Robust Myelin Water Imaging from multi-echo T2 data using second-order Tikhonov regularization with control point', *In: Proceedings of the International Society of Magnetic Resonance in Medicine, Montreal, Canada*, p. 4901.

Canales-Rodríguez, Erick Jorge *et al.* (2019) 'Sparse wars: A survey and comparative study of spherical deconvolution algorithms for diffusion MRI', *NeuroImage*. Academic Press Inc., 184, pp. 140–160. doi: 10.1016/j.neuroimage.2018.08.071.

Caruyer, E. *et al.* (2013) 'Design of multishell sampling schemes with uniform coverage in diffusion MRI', *Magnetic resonance in medicine*. Wiley Online Library, 69(6), pp. 1534–1540. doi: 10.1002/mrm.24736.

Castellanos, J. L., Gómez, S. and Guerra, V. (2002) 'The triangle method for finding the corner of the L-curve', *Appl. Numer. Math.*, 43, pp. 359–373. doi: 10.1016/S0168-9274(01)00179-9.

Cercignani, M. and Bouyagub, S. (2018) 'Brain microstructure by multi-modal MRI: Is the whole greater than the sum of its parts?', *Neuroimage*, 182, pp. 117–127.

Chatterjee, S. *et al.* (2018) 'Identification of Gadolinium contrast enhanced regions in MS lesions using brain tissue microstructure information obtained from diffusion and T2 relaxometry MRI', *In: Frangi AF et al (Eds.): MICCAI 2018, LNCS*, 11072, pp. 63–71.

Cheng, J., Shen, D. and Yap, P.-T. (2014) 'Designing single-and multiple-shell sampling schemes for diffusion MRI using spherical code', in *International Conference on Medical Image Computing and Computer-Assisted Intervention*, pp. 281–288.

Close, T. G. *et al.* (2009) 'A software tool to generate simulated white matter structures for the assessment of fibre-tracking algorithms', *NeuroImage*. Elsevier Inc., 47(4), pp. 1288–1300. doi: 10.1016/j.neuroimage.2009.03.077.

Daducci, A. *et al.* (2015) 'Accelerated Microstructure Imaging via Convex Optimization (AMICO) from diffusion MRI data', *NeuroImage*. The Authors, 105, pp. 32–44. doi: 10.1016/j.neuroimage.2014.10.026.

Dortch, R. D. *et al.* (2013) 'Characterizing inter-compartmental water exchange in myelinated tissue using relaxation exchange spectroscopy', *Magnetic Resonance in Medicine*. John Wiley and Sons Inc, 70(5), pp. 1450–1459. doi: 10.1002/mrm.24571.

Drobnjak, I. *et al.* (2016) 'PGSE, OGSE, and sensitivity to axon diameter in diffusion MRI:

Insight from a simulation study', *Magnetic Resonance in Medicine*. John Wiley and Sons Inc, 75(2), pp. 688–700. doi: 10.1002/mrm.25631.

Drobnjak, I. and Alexander, D. C. (2011) 'Optimising time-varying gradient orientation for microstructure sensitivity in diffusion-weighted MR', *Journal of Magnetic Resonance*. J Magn Reson, 212(2), pp. 344–354. doi: 10.1016/j.jmr.2011.07.017.

Drobnjak, I., Siow, B. and Alexander, D. C. (2010) 'Optimizing gradient waveforms for microstructure sensitivity in diffusion-weighted MR', *Journal of Magnetic Resonance*. Academic Press, 206(1), pp. 41–51. doi: 10.1016/j.jmr.2010.05.017.

Dyrby, T. B. *et al.* (2013) 'Contrast and stability of the axon diameter index from microstructure imaging with diffusion MRI', *Magnetic Resonance in Medicine*, 70(3), pp. 711–721. doi: 10.1002/mrm.24501.

Erzinger, C. *et al.* (2015) 'Nonconventional MRI and microstructural cerebral changes in multiple sclerosis', *Nature Reviews Neurology*, 11, pp. 676–686.

Ferizi, U. *et al.* (2015) 'White matter compartment models for in vivo diffusion {MRI} at 300 mT/m', *NeuroImage*, 118, pp. 468–483.

Ferizi, U. *et al.* (2017) 'Diffusion MRI microstructure models with in vivo human brain Connectome data: results from a multi-group comparison', *NMR in Biomedicine*. doi: 10.1002/nbm.3734.

Fick, A. (1855) 'Ueber Diffusion', *Annalen der Physik*. John Wiley & Sons, Ltd, 170(1), pp. 59–86. doi: 10.1002/andp.18551700105.

Fieremans, E. *et al.* (2008) 'Simulation and experimental verification of the diffusion in an anisotropic fiber phantom', *Journal of Magnetic Resonance*, 190(2), p. 189. doi: 10.1016/j.jmr.2007.10.014.

Filippi, M. and Agosta, F. (2007) 'Magnetization transfer MRI in multiple sclerosis', *J Neuroimaging*, Suppl 1, pp. 22S–26S.

Fischi-Gomez, E. *et al.* (2021) 'Multi-compartment diffusion MRI, T2 relaxometry and myelin water imaging as neuroimaging descriptors for anomalous tissue detection'. Available at: <http://arxiv.org/abs/2104.07502> (Accessed: 13 May 2021).

Freund, Y. and Schapire, R. E. (1997) 'A Decision-Theoretic Generalization of On-Line Learning and an Application to Boosting', *Journal of Computer and System Sciences*, 55(1), pp. 119–139.

Galdos, J. I. (1980) 'A Cramer-Rao Bound for Multidimensional Discrete-Time Dynamical Systems', *IEEE Transactions on Automatic Control*, 25(1), pp. 117–119. doi: 10.1109/TAC.1980.1102211.

Garyfallidis, E. *et al.* (2014) 'Dipy, a library for the analysis of diffusion MRI data', *Frontiers in Neuroinformatics*, 8. doi: 10.3389/fninf.2014.00008.

Van Gelderen, P. *et al.* (1994) 'Evaluation of Restricted Diffusion in Cylinders. Phosphocreatine in Rabbit Leg Muscle', *Journal of Magnetic Resonance, Series B*, 103(3), pp. 255–260. doi:

10.1006/jmrb.1994.1038.

Ginsburger, K. *et al.* (2019) ‘MEDUSA: A GPU-based tool to create realistic phantoms of the brain microstructure using tiny spheres’, *NeuroImage*. Elsevier, 193, pp. 10–24. doi: 10.1016/j.neuroimage.2019.02.055.

Girard, G. *et al.* (2021) ‘Diffusion-Simulated Connectivity Challenge’. doi: 10.5281/ZENODO.4733450.

Gregor, K. and Lecun, Y. (2010) ‘Learning Fast Approximations of Sparse Coding’. doi: 10.1049/ip-vis:20045082.

Grussu, F. *et al.* (2016) ‘A framework for optimal whole-sample histological quantification of neurite orientation dispersion in the human spinal cord’, *Journal of Neuroscience Methods*. Elsevier B.V., 273, pp. 20–32. doi: 10.1016/j.jneumeth.2016.08.002.

Hall, M. G. (2009) ‘Convergence and parameter choice for monte carlo simulations of diffusion MRI data’, 28(9), pp. 1354–1364.

Hall, M. G. and Alexander, D. C. (2009) ‘Convergence and Parameter Choice for Monte-Carlo Simulations of Diffusion MRI’, *IEEE Transactions on Medical Imaging*, 28(9), pp. 1354–1364. doi: 10.1109/TMI.2009.2015756.

Haninec, P. (1986) ‘Undulating course of nerve fibres and bands of Fontana in peripheral nerves of the rat’, *Anatomy and Embryology*, 174(3), pp. 407–411. doi: 10.1007/BF00698791.

Hennig, J., Weigel, M. and Scheffler, K. (2004) ‘Calculation of Flip Angles for Echo Trains with Predefined Amplitudes with the Extended Phase Graph (EPG)-Algorithm: Principles and Applications to Hyperecho and 21TRAPS Sequences’, *Magn. Reson. Med*, 51(1), pp. 68–80. doi: 10.1002/mrm.10658.

Horsfield, M. A., Jones, D. K. and Horsfield, ; M A Jones ; D K (2002) ‘Applications of diffusion-weighted and diffusion tensor MRI to white matter diseases- a review’, *NMR in Biomedicine*. NMR Biomed, 15(7–8), pp. 570–577. doi: 10.1002/nbm.787.

Hrabe, J. *et al.* (2004) ‘A model of effective diffusion and tortuosity in the extracellular space of the brain’, *Biophysical Journal*, 87(3), pp. 1606–1617. doi: 10.1529/biophysj.103.039495.

Hui, Z. P. L. H. G. J. M. P. D. C. A. *et al.* (2011) ‘Axon diameter mapping in the presence of orientation dispersion with diffusion MRI.’, *NeuroImage*, 56(3), pp. 1301–1315. doi: 10.1016/j.neuroimage.2011.01.084.

Innocenti, G. M., Caminiti, R. and Hof, P. R. (2010) ‘Fiber composition in the planum temporale sector of the corpus callosum in chimpanzee and human’, *Brain Structure and Function*. Brain Struct Funct, 215(2), pp. 123–128. doi: 10.1007/s00429-010-0274-9.

Jelescu, I. O. *et al.* (2016) ‘Degeneracy in model parameter estimation for multi-compartmental diffusion in neuronal tissue’, *NMR in Biomedicine*, 29(1), pp. 33–47. doi: 10.1002/nbm.3450.

Jensen, J. H. *et al.* (2005) ‘Diffusional kurtosis imaging: The quantification of non-Gaussian water diffusion by means of magnetic resonance imaging’, *Magnetic Resonance in Medicine*.

John Wiley and Sons Inc., 53(6), pp. 1432–1440. doi: 10.1002/mrm.20508.

John, C. and Crank, J. (1979) ‘The Mathematics of Diffusion.’, in Press, C. and Press, C. (eds). Clarendon Press.

Jones, D. K., Horsfield, M. A. and Simmons, A. (1999) ‘Optimal strategies for measuring diffusion in anisotropic systems by magnetic resonance imaging’, *Magnetic Resonance in Medicine: An Official Journal of the International Society for Magnetic Resonance in Medicine*. Wiley Online Library, 42(3), pp. 515–525.

Kaden, E. *et al.* (2016) ‘Multi-compartment microscopic diffusion imaging’, *NeuroImage*, 139, pp. 346–359.

Kerschensteiner, M. *et al.* (2004) ‘Remodeling of axonal connections contributes to recovery in an animal model of multiple sclerosis’, *J Exp Med*, 200(8), pp. 1027–1038.

Khasawneh, A. *et al.* (2020) ‘Development of a novel phantom using polyethylene glycol for the visualization of restricted diffusion in diffusion kurtosis imaging and apparent diffusion coefficient subtraction method’, *Biomedical Reports*. Spandidos Publications, 13(6), pp. 1–7. doi: 10.3892/br.2020.1359.

Klein, S. *et al.* (2010) ‘elastix: a toolbox for intensity based medical image registration’, *IEEE Transactions on Medical Imaging*, 29(1), pp. 196–205.

Klistorner, A. *et al.* (2018) ‘Evidence of progressive tissue loss in the core of chronic MS lesions: A longitudinal DTI study’, *Neuroimage Clin*, 17, pp. 1028–1035.

Lamantia, A.-S. and Rakic, P. (1990) ‘Cytological and quantitative characteristics of four cerebral commissures in the rhesus monkey’, *Journal of Comparative Neurology*, 291(4), pp. 520–537. doi: 10.1002/cne.902910404.

Latour, L. L. *et al.* (1994) ‘Time-dependent diffusion of water in a biological model system’, *Proceedings of the National Academy of Sciences of the United States of America*. National Academy of Sciences, 91(4), pp. 1229–1233. doi: 10.1073/pnas.91.4.1229.

Laule, C. *et al.* (2006) ‘Myelin water imaging in multiple sclerosis: quantitative correlations with histopathology’, *Mult Scler*, 12, pp. 747–753.

Lavdas, I. *et al.* (2013) ‘A phantom for diffusion-weighted MRI (DW-MRI)’, *Journal of Magnetic Resonance Imaging*. J Magn Reson Imaging, 38(1), pp. 173–179. doi: 10.1002/jmri.23950.

Liewald, D. *et al.* (2014) ‘Distribution of axon diameters in cortical white matter: an electron-microscopic study on three human brains and a macaque’, *Biological Cybernetics*. Springer Verlag, 108(5), pp. 541–557. doi: 10.1007/s00422-014-0626-2.

Lin, M. *et al.* (2016) ‘Simulation of changes in diffusion related to different pathologies at cellular level after traumatic brain injury’, *Magnetic Resonance in Medicine*, 76(1), pp. 290–300. doi: 10.1002/mrm.25816.

Lipinski, H. G. (1990) ‘Monte Carlo simulation of extracellular diffusion in brain tissues’,



*Physics in Medicine and Biology*, 35(3), p. 441. doi: 10.1088/0031-9155/35/3/012.

Lipp, I. *et al.* (2019) ‘Comparing MRI metrics to quantify white matter microstructural damage in multiple sclerosis’, *Hum Brain Mapp*, 40, pp. 2917–2932.

Mackay, A. *et al.* (1994) ‘In vivo visualization of myelin water in brain by magnetic resonance’, *Magn. Reson. Med*, 31, pp. 673–677. doi: 10.1002/mrm.1910310614.

MacKay, A. L. and Laule, C. (2016) ‘Magnetic resonance of myelin water: an in vivo marker for myelin’, *Brain Plast*, 2(1), pp. 71–91.

McKenzie, C. A. *et al.* (1999) ‘Fast acquisition of quantitative T2 maps’, *Magn Reson Med*, 41(1), pp. 208–212.

McKinnon, E. T. and Jensen, J. H. (2019) ‘Measuring intra-axonal T2 in white matter with direction-averaged diffusion MRI’, *Magnetic Resonance in Medicine*. John Wiley and Sons Inc, 81(5), pp. 2985–2994. doi: 10.1002/mrm.27617.

Mitra, P. P. and Halperin, B. I. (1995) ‘Effects of Finite Gradient-Pulse Widths in Pulsed-Field-Gradient Diffusion Measurements’, *Journal of Magnetic Resonance, Series A*, p. 94. doi: 10.1006/jmra.1995.1060.

Mitra, P. P., Sen, P. N. and Schwartz, L. M. (1993) ‘Short-time behavior of the diffusion coefficient as a geometrical probe of porous media’, *Physical Review B. Phys Rev B Condens Matter*, 47(14), pp. 8565–8574. doi: 10.1103/PhysRevB.47.8565.

Mollink, J. *et al.* (2017) ‘Evaluating fibre orientation dispersion in white matter: Comparison of diffusion MRI, histology and polarized light imaging’, *NeuroImage*, 157(June), pp. 561–574. doi: 10.1016/j.neuroimage.2017.06.001.

Mori, S. and Barker, P. B. (1999) ‘Diffusion magnetic resonance imaging: its principle and applications.’, *The Anatomical Record*, 257(3), pp. 102–9. doi: 10.1002/(SICI)1097-0185(19990615)257:3<102::AID-AR7>3.0.CO;2-6 [pii].

Murday, J. S. and Cotts, R. M. (1968) ‘Self-diffusion coefficient of liquid lithium’, *The Journal of Chemical Physics*. American Institute of PhysicsAIP, 48(11), pp. 4938–4945. doi: 10.1063/1.1668160.

Nath, V. *et al.* ‘Tractography reproducibility challenge with empirical data (TraCED): The 2017 ISMRM diffusion study group challenge’, *Journal of Magnetic Resonance Imaging*. John Wiley and Sons Inc., 51(1), pp. 234–249. doi: 10.1002/jmri.26794.

Nedjati-Gilani, G. L. *et al.* (2017) ‘Machine learning based compartment models with permeability for white matter microstructure imaging’, *NeuroImage*. Elsevier, 150(July 2016), pp. 119–135. doi: 10.1016/j.neuroimage.2017.02.013.

Neema, M. *et al.* (2009) ‘3 T MRI relaxometry detects T2 prolongation in the cerebral normal-appearing white matter in multiple sclerosis’, *Neuroimage*, 46(3), pp. 633–641.

Neuman, C. H. (1974) ‘Spin echo of spins diffusing in a bounded medium’, *The Journal of Chemical Physics*, 60(11), pp. 4508–4511. doi: 10.1063/1.1680931.



- Nicholson, C. (2001) 'Diffusion and related transport mechanisms in brain tissue', *Reports on Progress in Physics*. IOP Publishing, 64(7), pp. 815–884. doi: 10.1088/0034-4885/64/7/202.
- Nilsson, M. *et al.* (2012) 'The importance of axonal undulation in diffusion MR measurements: A Monte Carlo simulation study', *NMR in Biomedicine*. John Wiley & Sons, Ltd, 25(5), pp. 795–805. doi: 10.1002/nbm.1795.
- Nilsson, M. *et al.* (2013) 'The role of tissue microstructure and water exchange in biophysical modelling of diffusion in white matter', *Magnetic Resonance Materials in Physics, Biology and Medicine*, 26(4), pp. 345–370. doi: 10.1007/s10334-013-0371-x.
- Nilsson, M. *et al.* (2017) 'Resolution limit of cylinder diameter estimation by diffusion MRI: The impact of gradient waveform and orientation dispersion', *NMR in Biomedicine*. John Wiley and Sons Ltd, 30(7). doi: 10.1002/nbm.3711.
- Noseworthy, J. J. *et al.* (2000) 'Multiple Sclerosis', *N Engl J Med*, 343, pp. 938–952.
- Palombo, M., Alexander, D. C. and Zhang, H. (2019) 'A generative model of realistic brain cells with application to numerical simulation of the diffusion-weighted MR signal', *NeuroImage*. Academic Press Inc., 188, pp. 391–402. doi: 10.1016/j.neuroimage.2018.12.025.
- Panagiotaki, E. *et al.* (2010) 'High-Fidelity Meshes from Tissue Samples for Diffusion MRI simulations', *Medical Image Computing and Computer-Assisted Intervention – MICCAI 2010*, pp. 404–411.
- Panagiotaki, E. *et al.* (2012) 'Compartment models of the diffusion MR signal in brain white matter: A taxonomy and comparison', *NeuroImage*, 59(3), pp. 2241–2254. doi: 10.1016/j.neuroimage.2011.09.081.
- Piredda, G. F. *et al.* (2020) 'Fast and high-resolution myelin water imaging: Accelerating multi-echo GRASE with CAIPIRINHA', *Mag Reson Med*, pp. 1–14. doi: 10.1002/mrm.28427.
- Powles, J. G. *et al.* (1992) 'Exact Analytic Solutions for Diffusion Impeded by an Infinite Array of Partially Permeable Barriers', *Proceedings: Mathematical and Physical Sciences*. The Royal Society, 436(1897), pp. 391–403. Available at: <http://www.jstor.org/stable/52042>.
- Prasloski, T., Mädler, B., *et al.* (2012) 'Applications of stimulated echo correction to multicomponent T2 analysis', *Magn. Reson. Med*, 67, pp. 1803–1814. doi: 10.1002/mrm.23157.
- Prasloski, T., Rauscher, A., *et al.* (2012) 'Rapid whole cerebrum myelin water imaging using a 3D GRASE sequence', *Neuroimage*, 63(1), pp. 533–539. doi: 10.1016/j.neuroimage.2012.06.064.
- Price, W. S. (1997) 'Pulsed-Field Gradient Nuclear Magnetic Resonance as a Tool for Studying Translational Diffusion: Part 1. Basic Theory', *Concepts Magn. Reson.*, 9(5), pp. 299–336. doi: 10.1002/chin.199750339.
- Rafael-Patino, J. *et al.* (2017) 'Validating Particle Dynamics in Monte Carlo Diffusion Simulation Using the Finite Element Method', *Proc. 25th Scientific Meeting of the International Society for Magnetic Resonance in Medicine*. Honolulu, HI, USA: Proc. Intl. Soc. Mag. Reson. Med. 25, p. 1849.

Rafael-Patino, J. *et al.* (2019) ‘Learning global brain microstructure maps using trainable sparse encoders’. Available at: <http://infoscience.epfl.ch/record/265398>.

Rafael-Patino, J., Yu, T., *et al.* (2020) ‘DWI Simulation-Assisted Machine Learning Models for Microstructure Estimation’, in *Mathematics and Visualization*. Springer Science and Business Media Deutschland GmbH, pp. 125–134. doi: 10.1007/978-3-030-52893-5\_11.

Rafael-Patino, J., Girard, G., *et al.* (2020) ‘Multi-diffusion and Multi-T2 weighted Monte-Carlo Simulations’, *2020 OHBM ANNUAL MEETING*. doi: 10.13140/RG.2.2.19239.78241.

Rafael-Patino, J., Romascano, D., *et al.* (2020) ‘Robust Monte-Carlo Simulations in Diffusion-MRI: Effect of the Substrate Complexity and Parameter Choice on the Reproducibility of Results’, *Frontiers in Neuroinformatics*. Frontiers Media S.A., 14, p. 8. doi: 10.3389/fninf.2020.00008.

Rafael-Patino, J. *et al.* (2021) ‘The Diffusion-Simulated Connectivity Dataset’. Mendeley, 1. doi: 10.17632/FGF86JDFG6.1.

Rafael-Patiño, J., Ramírez-Manzanares, A. and Rivera, M. (2011) ‘Estimation of anisotropic water diffusion indexes on axon bundle crossings’, in *Proceedings - 2011 10th Mexican International Conference on Artificial Intelligence: Advances in Artificial Intelligence and Applications, MICAI 2011 - Proceedings of Special Session*. doi: 10.1109/MICAI.2011.33.

Rafael-Patino, J. *et al.* (2019) *Phantoms for Diffusion Simulations: Multi-Objective Differential Evolution for Realistic Numerical (MODERN) Phantoms*. Available at: <https://archive.ismrm.org/2019/3635.html> (Accessed: 1 April 2021).

Ramírez-Manzanares, A. *et al.* (2010) ‘Single and multi diffusion-tensor based kernels for anisotropic filtering of brain DW-MR images’, *Proceedings - 2010 IEEE Electronics, Robotics and Automotive Mechanics Conference, CERMA 2010*, (1), pp. 399–404. doi: 10.1109/CERMA.2010.113.

Reisert, M. *et al.* (2017) ‘Disentangling micro from mesostructure by diffusion MRI: A Bayesian approach’, *NeuroImage*, 147(June), pp. 964–975. doi: 10.1016/j.neuroimage.2016.09.058.

Rensonnet, G. *et al.* (2018) ‘Assessing the validity of the approximation of diffusion-weighted-MRI signals from crossing fascicles by sums of signals from single fascicles’, *Magnetic Resonance in Medicine*, 79(4), pp. 2332–2345. doi: 10.1002/mrm.26832.

Rensonnet, G. *et al.* (2019) ‘Towards microstructure fingerprinting: Estimation of tissue properties from a dictionary of Monte Carlo diffusion MRI simulations’, *NeuroImage*. Academic Press Inc., 184, pp. 964–980. doi: <https://doi.org/10.1016/j.neuroimage.2018.09.076>.

Rensonnet, G. *et al.* (2020) ‘A Signal Peak Separation Index for axisymmetric B-tensor encoding’. Available at: <http://arxiv.org/abs/2010.08389> (Accessed: 1 April 2021).

Roebroek, A. *et al.* (2008) ‘High-resolution diffusion tensor imaging and tractography of the human optic chiasm at 9.4 T’, *NeuroImage*, 39(1), pp. 157–168. doi: 10.1016/j.neuroimage.2007.08.015.

Romascano, D. *et al.* (2020) ‘ActiveAx<sub>ADD</sub>: Toward non-parametric and orientationally invariant

axon diameter distribution mapping using PGSE', *Magnetic Resonance in Medicine*. John Wiley and Sons Inc, 83(6), pp. 2322–2330. doi: 10.1002/mrm.28053.

Romascano, D. P. R. (2019) 'Towards non-parametric reconstruction of axon diameter distributions using diffusion MRI and regularized discrete linear modeling'. Lausanne: EPFL, p. 112. doi: 10.5075/epfl-thesis-9091.

La Rosa, F. *et al.* (2018) 'Shallow vs deep learning architectures for white matter lesion segmentation in the early stages of multiple sclerosis', In: Crimi A *et al.* (Eds) *Brainlesion: Glioma, Multiple Sclerosis, Stroke and Traumatic Brain Injuries. BrainLes 2018. LNCS*, 11383.

Schilling, K. G. *et al.* (2018) 'Histological validation of diffusion MRI fiber orientation distributions and dispersion', *NeuroImage*. Elsevier Inc., 165, p. 200. doi: 10.1016/j.neuroimage.2017.10.046.

Sepehrband, F. *et al.* (2016) 'Towards higher sensitivity and stability of axon diameter estimation with diffusion-weighted MRI', *NMR in Biomedicine*, 29(3), pp. 293–308. doi: 10.1002/nbm.3462.

Sjölund, J. *et al.* (2015) 'Constrained optimization of gradient waveforms for generalized diffusion encoding', *Journal of Magnetic Resonance*, 261, pp. 157–168. doi: 10.1016/j.jmr.2015.10.012.

Sorensen, A. G. *et al.* (1996) 'Hyperacute stroke: Evaluation with combined multisection diffusion-weighted and hemodynamically weighted echo-planar MR imaging', *Radiology*. Radiological Society of North America Inc., pp. 391–401. doi: 10.1148/radiology.199.2.8668784.

Sotak, C. H. (2002) 'The role of diffusion tensor imaging in the evaluation of ischemic brain - A review', *NMR in Biomedicine*. NMR Biomed, pp. 561–569. doi: 10.1002/nbm.786.

Stikov, N. (2015) 'In vivo histology of the myelin g-ratio with magnetic resonance imaging', *Neuroimage*, 118, pp. 397–405.

Syková, E. and Nicholson, C. (2008) 'Diffusion in brain extracellular space', *Physiological Reviews*. NIH Public Access, pp. 1277–1340. doi: 10.1152/physrev.00027.2007.

Tanner, J. E. and Stejskal, E. O. (1968) 'Restricted self-diffusion of protons in colloidal systems by the pulsed-gradient, spin-echo method', *The Journal of Chemical Physics*, 49(4), pp. 1768–1777. doi: 10.1063/1.1670306.

Tao, L. and Nicholson, C. (2004) 'Maximum geometrical hindrance to diffusion in brain extracellular space surrounding uniformly spaced convex cells', *Journal of Theoretical Biology. J Theor Biol*, 229(1), pp. 59–68. doi: 10.1016/j.jtbi.2004.03.003.

Tariq, M. *et al.* (2016) 'Bingham-NODDI: Mapping anisotropic orientation dispersion of neurites using diffusion MRI', *NeuroImage*. Academic Press Inc., 133, pp. 207–223. doi: 10.1016/j.neuroimage.2016.01.046.

Tax, C. M. W. *et al.* (2020) 'The dot-compartment revealed? Diffusion MRI with ultra-strong gradients and spherical tensor encoding in the living human brain', *NeuroImage*. Academic Press Inc., 210, p. 116534. doi: 10.1016/j.neuroimage.2020.116534.

- Tournier, J. D., Calamante, F. and Connelly, A. (2007) 'Robust determination of the fibre orientation distribution in diffusion MRI: Non-negativity constrained super-resolved spherical deconvolution', *NeuroImage*, 35(4), pp. 1459–1472. doi: 10.1016/j.neuroimage.2007.02.016.
- Truffet, R. *et al.* (2020) *An Evolutionary Framework for Microstructure-Sensitive Generalized Diffusion Gradient Waveforms, Lecture Notes in Computer Science (including subseries Lecture Notes in Artificial Intelligence and Lecture Notes in Bioinformatics)*. doi: 10.1007/978-3-030-59713-9\_10.
- Tuch, D. S. (2004) 'Q-ball imaging', *Magnetic Resonance in Medicine*. John Wiley and Sons Inc., 52(6), pp. 1358–1372. doi: 10.1002/mrm.20279.
- Verth, J. M. Van and Bishop, L. M. (2008) 'Chapter 12 - Intersection Testing', in Verth, J. M. Van and Bishop, L. M. (eds) *Essential Mathematics for Games and Interactive Applications (Second Edition)*. Second Edi. Boston: Morgan Kaufmann, pp. 541–599. doi: <https://doi.org/10.1016/B978-0-12-374297-1.50017-9>.
- Warntjes, M. *et al.* (2016) 'Modeling the Presence of Myelin and Edema in the Brain Based on Multi-Parametric Quantitative MRI', *Frontiers in Neurology*, 17.
- Whittall, K. P. *et al.* (1997) 'In vivo measurement of T2 distributions and water contents in normal human brain', *Magnetic Resonance in Medicine*. John Wiley and Sons Inc, 37(1), pp. 34–43. doi: 10.1002/mrm.1910370107.
- Yaniv, A. D. C. A. D. K. J. A. B. T. E. J. B. C. A. C. Y. C. T. B. D. P. S. H. T. R. K. D. L. G. J. M. P. C. P. (2013) 'The CONNCT project: Combining macro- and micro-structure', *NeuroImage*.
- Yaniv, A. R. Z. F. G. K. R. P. J. B. (2004) 'New Modeling and Experimental Framework to Characterize Hindered and Restricted Water Diffusion in Brain White Matter', *Magnetic Resonance in Medicine*.
- Ye, C. (2017) 'Tissue microstructure estimation using a deep network inspired by a dictionary-based framework', *Medical Image Analysis*. Elsevier B.V., 42(Supplement C), pp. 288–299. doi: 10.1016/j.media.2017.09.001.
- Yeh, C.-H. *et al.* (2013) 'Diffusion Microscopist Simulator: A General Monte Carlo Simulation System for Diffusion Magnetic Resonance Imaging', *PLoS ONE*, 8(10), p. e76626. doi: 10.1371/journal.pone.0076626.
- Zhang, H. . S. T. W.-K. C. A. D. C. H. H. . S. T. W.-K. C. A. D. C. *et al.* (2012) 'NODDI: practical in vivo neurite orientation dispersion and density imaging of the human brain.', *NeuroImage*. Elsevier Inc., 61(4), pp. 1000–1016. doi: 10.1016/j.neuroimage.2012.03.072.
- Zhang, J. *et al.* (2005) 'Fiber Tractography in Diffusion Tensor Magnetic Resonance Imaging: A Survey and Beyond', (437), pp. 1–26.
- Zhou, Y. *et al.* (2012) 'Diffusion tensor imaging of forearm nerves in humans', *Journal of Magnetic Resonance Imaging*, 36(4), p. 920. doi: 10.1002/jmri.23709.